ELSEVIER

Current Opinion in Colloid & Interface Science 11 (2006) 81 – 117

Current Opinion in COLLOID and INTERFACE SCIENCE

www.elsevier.com/locate/cocis

Nucleation and growth of zeolites and inorganic mesoporous solids: Molecular insights from magnetic resonance spectroscopy

Jan D. Epping, Bradley F. Chmelka *

Department of Chemical Engineering, University of California, Santa Barbara, CA 93106, USA

Available online 9 May 2006

Abstract

Inorganic nano- and mesoporous materials can be prepared with a variety of compositions, structures, and macroscopic morphologies. Due to their wide range of properties and applications, a detailed understanding of the mechanisms governing their formation under different synthesis conditions is of particular interest. Magnetic resonance spectroscopy offers a variety of powerful and complementary techniques for acquiring insights on the molecular processes and structures that underly crystallization or self-assembly of these complex heterogeneous systems. This review examines contributions from NMR and EPR spectroscopy to the recent developments and current understanding in the nucleation and growth of nanoporous molecular sieves and mesoporous inorganic solids.

Keywords: NMR; EPR; In situ spectroscopy; MQ-MAS; Double-quantum ^{29}Si NMR; Zeolites; Molecular sieves; Mesoporous materials; Nanoporous solids; Silica; Titania; Aluminosilicas; Aluminosilicates; $AlPO_4$

1. Introduction

The design and synthesis of inorganic porous solids with diverse compositions, structures, and macroscopic morphologies are important for controlling their properties and interesting from both fundamental and technological perspectives. Across a wide range of compositions and pore sizes from sub-nanometer to micrometer length scales, porous inorganic solids can be prepared for extremely wide ranges of applications in adsorption, separations, catalysis, optics, etc. A similar diversity exists in the synthesis and processing conditions used, particularly with respect to the selection of different structure-directing agents, according to the compositions and physical dimensions of the pore sizes sought. This often leads to different physicochemical mechanisms among correlated and often competing kinetic processes that govern the nucleation and growth of ordered domains for different materials and different size regimes.

The most striking differences between nanoporous molecular sieves, such as zeolites and mesoporous (and larger) inorganic solids, such as those synthesized in the presence of surfactants or block-copolymers, are the differences in their short- and long-range structures. Fig. 1 displays and compares several key structural features for representative examples of two types of porous inorganic solids, specifically the siliceous zeolite ITQ-3 [2,3] and siliceous MCM-41 [1]. In particular, these materials have very different extents of molecular order in their frameworks, different characteristic ordering length scales (including pore dimensions), and different ordering periodicities. Zeolites possess crystalline inorganic frameworks with three-dimensional molecular order that allows well-defined faceted single crystals to be prepared, such as those shown in the scanning electron micrograph (SEM) in Fig. 1(a) for ITQ-3 [2]. Powder X-ray diffraction (XRD) patterns [Fig. 1(b)] yield a multitude of well-defined reflections with differing intensities at high scattering angles ($2\theta > 5°$) that can be indexed to complicated crystalline morphologies with pore dimensions that are typically ≤ 1 nm. The extent of molecular framework order can be established by solid-state ^{29}Si cross-polarization (CP) magic-angle-spinning (MAS) nuclear magnetic resonance (NMR) spectroscopy measurements. For example, the ^{29}Si CP/MAS NMR spectrum of siliceous ITQ-3 yields [Fig. 1(c)] three narrow (0.7 ppm, full-width-at-half-maximum, fwhm) well-resolved signals from each of the three crystallographically distinct and tetrahedrally coordinated ^{29}Si sites in a bulk powder sample.

* Corresponding author. Tel.: +1 805 893 3673; fax: +1 805 893 4731.
E-mail address: bradc@engineering.ucsb.edu (B.F. Chmelka).

1359-0294/$ - see front matter © 2006 Published by Elsevier Ltd.
doi:10.1016/j.cocis.2005.12.002

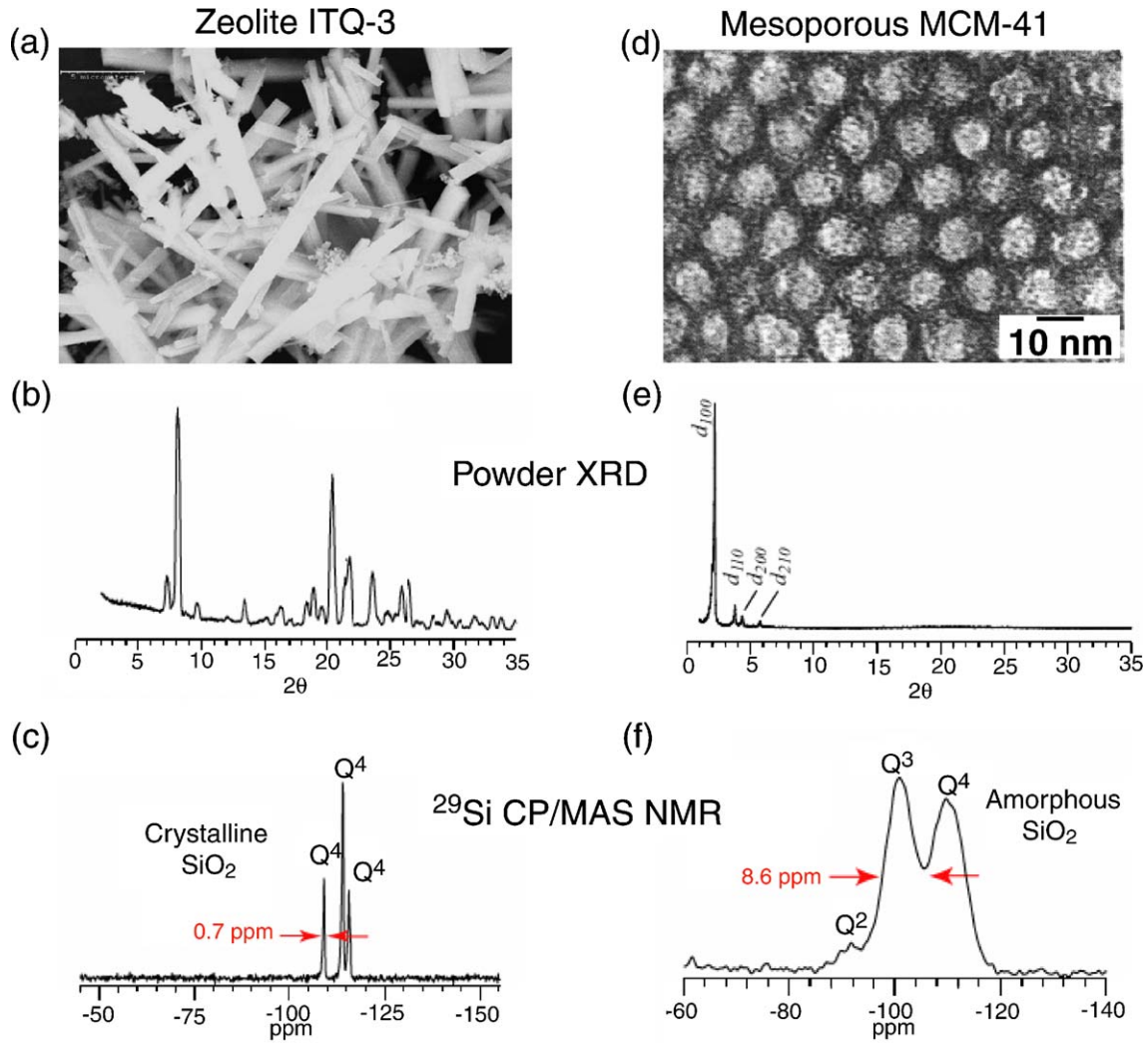

Fig. 1. Differences characteristic of crystalline siliceous zeolites and ordered mesoporous silicas: electron microscopy images, ^{29}Si CP/MAS NMR spectra, and X-ray powder diffraction patterns, respectively of (a)–(c) siliceous zeolite ITQ-3 and (d)–(f) mesoporous MCM-41 silica. [Adapted with permission from Ref. [1], copyright 1992 American Chemical Society. Adapted with permission from Ref. [2]. Copyright 1997 Wiley-VCH. Adapted from Ref. [3]. Copyright 2004, with permission from Elsevier.]

Mesoporous inorganic solids can similarly be prepared with highly uniform and periodic arrays of pores, although the structures are otherwise significantly different from zeolites. Mesoporous oxides, such as MCM-41 [1], have much larger pore dimensions (ca. 4–15 nm), which are uniform and adjustable, and generally do not possess three-dimensional (3D) crystallinity at a molecular level. As shown in the transmission electron microscopy (TEM) image in Fig. 1(d), MCM-41 is characterized by a hexagonally periodic arrangement of pores, which is consistent with the (*100*), (*110*), (*200*), and (*210*) reflections observed at small scattering angles ($2\theta < 5°$) in the powder XRD pattern in Fig. 1(e). However, unlike zeolites, little or no scattering intensity is observed at high scattering angles, indicating the absence of periodicity at nanometer length scales. Such molecular-level disorder is confirmed by the ^{29}Si CP/MAS NMR spectrum of siliceous MCM-41 in Fig. 1(f), which shows three broad peaks with linewidths that are an order-of-magnitude larger (~9 ppm, fwhm) than for zeolites [e.g., Fig. 1(c)]. In contrast to the highly locally ordered silicon sites in zeolites, the broad ^{29}Si peaks typical of mesoporous silicas reflect a broad distribution of four-coordinated Si sites, with different extents of cross-linking and non-uniform Si–O–Si bond angles and/or bond distances.

Zeolites and mesoporous inorganic solids may, thus, possess similar overall inorganic compositions (e.g., silica), but their structures tend to be entirely different. These differences crucially affect their macroscopic properties and additionally reflect the very different physicochemical processes that account for their early stage formation. The molecular origins of these structural differences will be the focus of this review of recent published work and current understanding of nucleation and growth of ordered domains in zeolite and mesoporous inorganic solids. Magnetic resonance spectroscopy methods are among the most powerful analytical methods available for studying molecular interactions and processes in complicated solution- and solid-state systems. The information provided by state-of-the-art NMR and Electron Paramagnetic Resonance (EPR) techniques, in conjunction with state-of-the-art syntheses

of porous materials, is providing new and detailed insights on the formation mechanisms of these important families of porous inorganic solids.

2. Formation mechanisms of crystalline nanoporous molecular sieves

Due to their immense importance as catalysts, sorbents, and ion-exchange materials, there is great interest in the processes by which different zeolites and related molecular sieves form, for the purpose of controlling their compositions, structures, and macroscopic properties [4–7]. Since the 1960s, numerous studies have been and still are undertaken to deepen understanding of the formation mechanisms of crystalline zeolites from alkaline precursor solutions. Such understanding has been driven increasingly by advances in characterization methodologies, which have allowed more detailed insights at early stages of zeolite crystal nucleation and growth and in subsequent resultant structures. Refs. [8–10] provide extensive overviews of different characterization approaches, including in situ methods, and discuss their contributions to the understanding of how zeolites form. Nuclear magnetic resonance (NMR) and electron paramagnetic resonance (EPR) spectroscopies, in particular, have witnessed tremendous innovation and progress in the development of methods that have led to enhanced signal sensitivity and spectral resolution from which new understanding has come. Diverse and complementary multinuclear applications of solution- and solid-state NMR methods and EPR techniques have elucidated a variety of profound insights on zeolite chemistry, structure, and properties, for which a rich literature exists. We refer the reader with specific interests in these areas to other reviews that discuss NMR measurements of zeolite structures [11], heterogeneous catalyst properties [11–15], the structure of Brønsted acid sites [11,16,17], pore size distributions [18], and guest–host interactions [19], which are beyond the scope of the present compilation. Here, we review recent literature with respect to new molecular-level insights provided by NMR and EPR spectroscopies on the nucleation and growth of crystalline zeolites, focusing principally on work that has appeared since a thorough review by Bell [20] in 1999.

2.1. Zeolite crystallization from alkaline solutions and amorphous gels

Zeolites are synthesized under highly alkaline hydrothermal conditions from silicate, aluminosilicate, or mixed oxide solutions containing different cationic or other organic structure-directing species. Under such conditions, a variety of silicate and/or other anions have been observed to be present in solution and have been studied with respect to their roles in zeolite crystallization. It was early-on proposed by Barrer et al. that zeolites are formed by the sequential addition of small "secondary building blocks" (SBUs) from solution [21]. Fig. 2 shows schematic structures of 23 silicate anions found in alkaline solutions determined from series of in situ solution ^{29}Si NMR measurements [22–25]. The structures range from monomeric silicate anions to larger oligomeric anions formed of SiO_4-tetrahedra that are linked through shared bridging oxygen atoms to form three-, four-, or five-membered rings. However, despite much searching, the open and flexible five-,

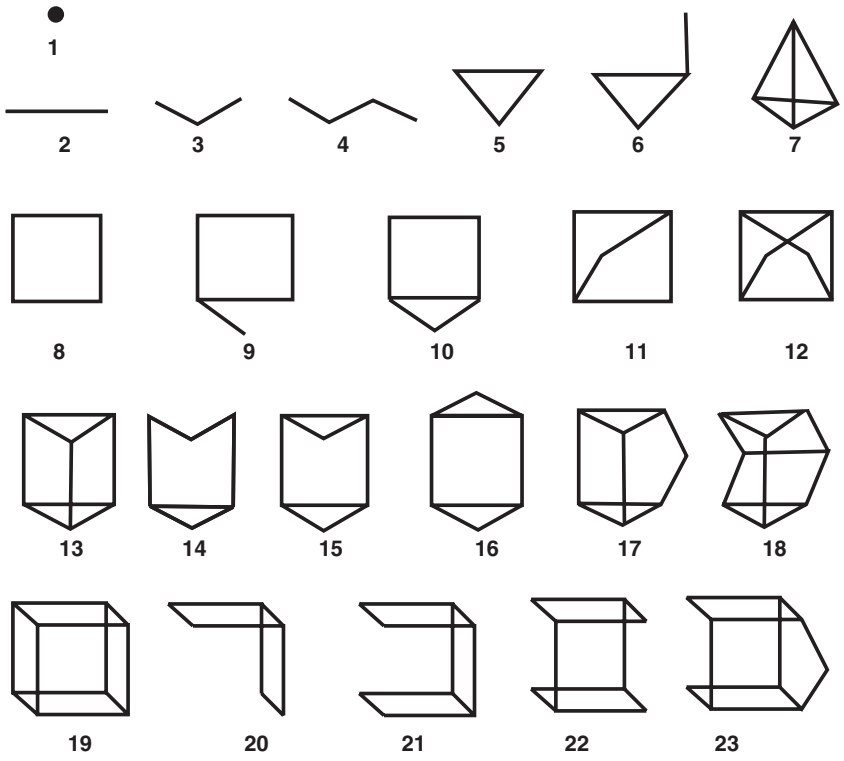

Fig. 2. Silicate structures in basic aqueous solution identified by analysis of solution-state ^{29}Si NMR [22–25]. Each line in the stick figure represents a Si–O–Si siloxane linkage. [Reprinted with permission from Ref. [32]. Copyright 2002 American Chemical Society.]

six-, and eight-membered ring systems proposed as SBUs have till now not yet been found [26]. The anions that have been identified generally consisted of Q^1, Q^2, and Q^3 silica species, where each silicon atom is covalently bound to one, two, or three neighboring silicon atoms via bridging oxygen atoms, respectively, while the fully condensed Q^4 species that primarily constitute the resulting zeolite structures were absent. Recently, three novel silicate anions with Q^4 silicon units were reported in alkaline aqueous solutions containing diquaternary ammonium species [27,28]. Additionally, the presence of novel cations containing five-ring structures was concluded from ^{29}Si solution NMR data recorded in precursor solutions for MFI-type zeolites [29–31], but this interpretation is still under debate [32].

The influence of tetraalkylammonium cations, which are widely used as structure-directing agents in the synthesis of zeolites with high Si/Al ratios, on the equilibria of silicate anions in solution has been studied in detail by solution-state ^{29}Si NMR [33,34]. The addition of tetraalkylammonium cations shifts the equilibria towards symmetric cage-like oligosilicate anions, in contrast to alkali–metal silicate solutions, where smaller asymmetric silicate anions tend to be found. Kinrade et al. [33] attribute this shift to a direct association of the organocations with cage-like oligomeric silicate anions to form a protective shell that impedes hydrolysis of the central anion. Generally, the structure-directing tendency of alkylammonium cations decreases systematically with the number and size of the alkyl substituents [35], the larger of which increase the hydrophobic character of the cations and thereby weaken interactions with the network-forming inorganic species. The addition of organic co-solvents, such as alcohols and amines has been shown to offset partially these effects [36,37].

The complex chemistry of silicate anions in alkaline zeolite precursor solutions and their interactions with SDA molecules leads to soluble precursor silicate species with diverse structures. However, there is little evidence for direct zeolite crystal growth by the aggregation of secondary building units in the syntheses of most zeolites. Knight et al. suggest that the different silicate species in solution often are little more than spectator species [32], while zeolite formation occurs by the relatively rapid formation of amorphous intermediate gels from solution and subsequent slow crystallization of the amorphous material. Exchange of soluble silicate species between the solution phase and the intermediate amorphous gel may contribute to the evolution of order and subsequent conversion of the amorphous gel into highly crystalline products [9]. Additionally, in some cases, soluble species may contribute to the growth of initial crystallization seeds by direct deposition on the surface of these growing zeolite crystals [9].

In the synthesis of some zeolites, the gels that are initially formed in a mixture of soluble silicon and aluminum precursor species under alkaline conditions must generally be aged for certain periods of time prior to heating in order to form highly crystalline zeolite products [6,38]. NMR spectroscopy has provided valuable molecular-level insights concerning the influence of gel aging on the nucleation and growth of zeolites. One example is the crystallization of zeolites with technologically important faujasite-type (FAU) structures, for which the crystallization rates and composition of the zeolite products depend strongly on the aging of the initial hydrogels formed by mixing sodium aluminate and colloidal silica in aqueous sodium hydroxide solutions [39,40]. Recent ex situ ^{29}Si MAS NMR experiments [41] on hydrogel samples extracted after different aging periods indicate that, during aging of the gel, colloidal silica is dissolved, and with increasing aging time, aluminosilicate species are formed consisting exclusively of Q^4(4Al) silicon units that are connected to four aluminum atoms via bridging oxygen atoms. The dissolution of the colloidal silica appears to be the rate-determining step of this process. TEM measurements of samples extracted after different extents of aging also show that longer aging times prior to crystallization lead to smaller particle sizes in the final zeolite FAU product [41]. Quantitative analysis of the different silicon species in the ^{29}Si NMR data indicates that the intermediate amorphous aluminosilica formed during aging has a significantly lower Si/Al ratio (i.e., higher Al content) than the final zeolite product and that Si/Al ratios increase continuously during crystallization [41]. This finding suggests that zeolite crystallization may not occur solely by conversion of amorphous aluminosilica gel intermediates, but may involve the incorporation of other siliceous solution-phase species from the reaction mixture along with possible depletion of Al species from the gel back into solution.

The evolution of order during the conversion of amorphous intermediate gels to crystalline zeolites may be followed on a molecular level by solid-state ^{27}Al and ^{29}Si MAS NMR [42]. Ex situ NMR studies [43,44] and dynamic light scattering [45] of zeolite precursors have shown that the initial sources of aluminum and silicon significantly affect the specific intermediates present, although apparently not the final structure of the zeolite product. Shi and co-workers reported the first in situ MAS study of zeolite A, which has a Si/Al ratio of one, acquiring ^{29}Si and ^{27}Al MAS spectra at intervals of 14 and 10 min, respectively, for a gel of composition $1Al_2O_3$:$2SiO_2$:2.4NaOH:$42H_2O$ [42]. The ^{29}Si MAS spectrum of the initial gel [Fig. 3(a), bottom spectrum] shows a weak resonance at −72 ppm, which corresponds to Q^0 silicate species, and a broad resonance between −75 and −95 ppm attributed to a complex mixture of Si(0Al), Si(1Al), Si(2Al), Si(3Al), and Si(4Al) species. For the first 56 min after the heating, there are few apparent changes in the ^{29}Si spectra, after which peaks at −85 and −89 ppm appear, which are attributed to Si(3Al) and Si(4Al) species, respectively, the latter of these corresponding to crystalline zeolite A [43]. The peak at −85 ppm was attributed to zeolite X impurities based on XRD measurements, its weak intensity, and previous ^{29}Si NMR measurements [46]. Between 84 and 140 min, the peak at −89 ppm becomes significantly more intense and narrow (ca. 150 Hz fwhm), reflecting increased local ordering of ^{29}Si environments and suggesting that zeolite A crystallization occurs on this time scale. After 140 min, this peak narrows further, but the relative integrated intensity remains approximately constant. ^{27}Al MAS spectra independently complement and corroborate the ^{29}Si MAS

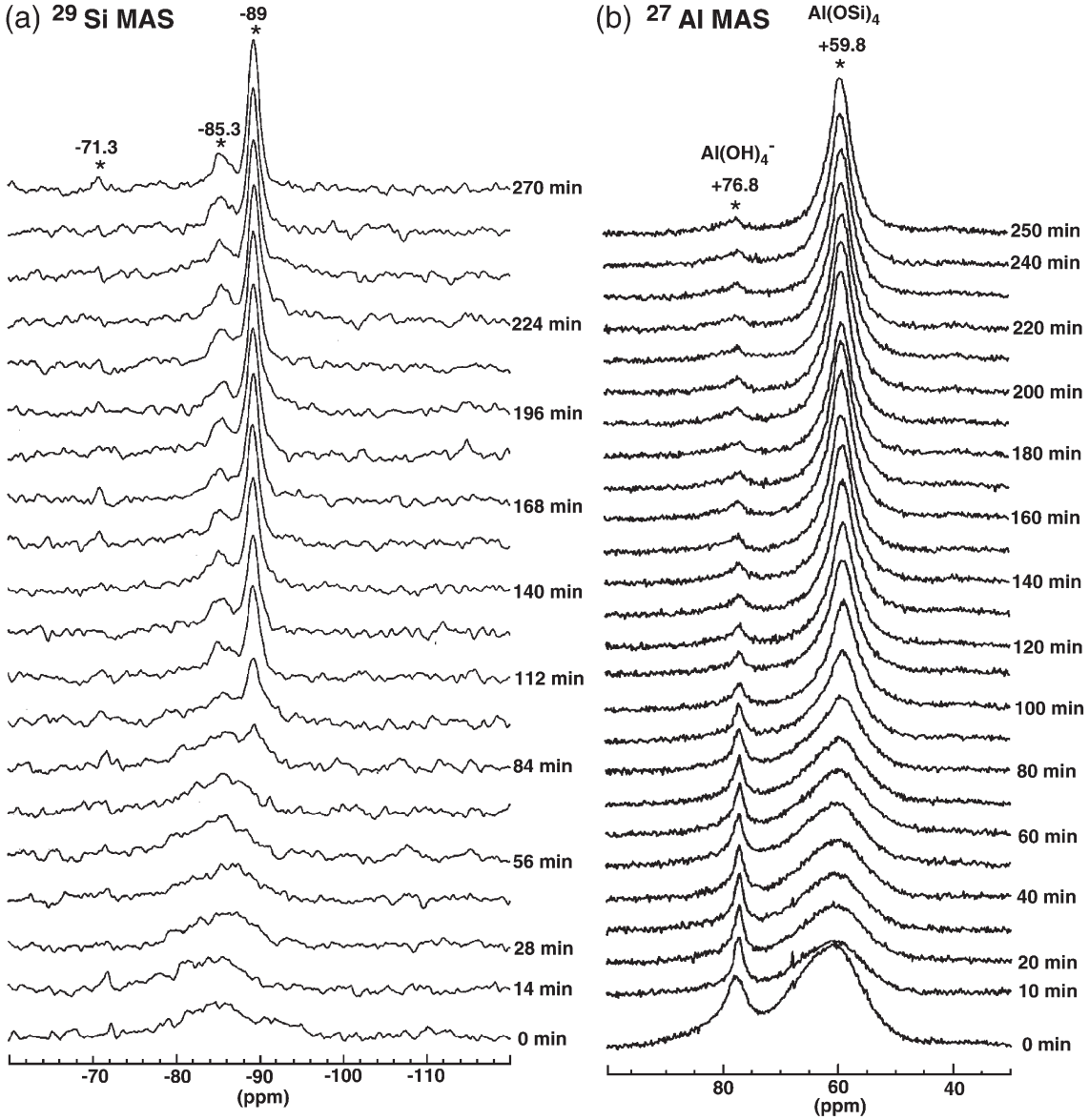

Fig. 3. In situ ^{29}Si and ^{27}Al MAS NMR spectra of zeolite A synthesized from an intermediate gel of composition $1Al_2O_3{:}2SiO_2{:}2.4Na_2O{:}42H_2O$ at 65 °C. (a) ^{29}Si MAS NMR spectra are shown from bottom to top measured in intervals of 14 min. (b) ^{27}Al MAS NMR spectra are shown from bottom to top measured in intervals of 10 min. [Adapted with permission from Ref. [42]. Copyright 1996 American Chemical Society.]

results. The ^{27}Al MAS spectrum of the initial gel [Fig. 3(b), bottom spectrum] shows a broad peak at 60 ppm that is attributed to a large distribution of four-coordinated aluminum species linked to silicon atoms via bridging oxygen atoms and a peak at 77 ppm attributed to soluble oligomeric alumina anions. Changes take place slowly also in the ^{27}Al MAS spectra during the first 60 min of the reaction, after which the intensity of the resonance at 77 ppm begins to decrease, a process that occurs more rapidly between 70 and 120 min after the start of the reaction, consistent with the incorporation of soluble alumina species into the solid framework. Concurrently, the intensity of the 60-ppm resonance increases and narrows, corresponding to increased local order of the aluminum environments.

Therefore, as the zeolite synthesis mixture is heated, ^{29}Si and ^{27}Al NMR results suggest that for a finite time, referred to as the 'induction period,' reaction intermediates remain mostly amorphous as a gel, prior to crystallization. With the onset of crystallization, most of the intermediate gel transforms relatively rapidly (on the order of tens of minutes for zeolite A) to crystalline zeolite product(s). This process appears to occur more rapidly in more concentrated gels, in which a greater number of small crystalline nuclei are expected to form during the induction period [42]. There is no indication from the ^{29}Si MAS measurements that larger solution-state silicate species, such as secondary building units, may be present, although this does not preclude the existence of a broad distribution of such species that are not resolved. A recent study [47] of the stages of zeolite A crystallization by ^{29}Si and ^{27}Al MAS NMR, in combination with small-angle X-ray diffraction, concluded that, during the induction period, reorganization of the amorphous aluminosilica gel takes place, leading to the formation of 'crystalline' zeolite nanoparticles throughout the amorphous

gel. These conclusions were based on changes in particle morphology observed in SAXS and TEM measurements that occurred significantly after the onset of local crystallinity, as seen by NMR and wide-angle XRD results. During subsequent growth of these crystallization seeds into well-ordered zeolite A crystals, transfer of soluble molecular species to the growing zeolite surface seems to be an important process, as suggested by the fact that crystal growth continues after a substantial part of the amorphous gel is already crystallized. The absence of significant changes in the ^{29}Si and ^{27}Al MAS spectra during the induction period prior to crystallization indicates that the gels retain appreciable local disorder during initial stages of network formation, apparently prior to crystallization, even for zeolite A with its rigorously alternating ordered Si–O–Al frameworks (Si/Al = 1).

In general, high-resolution NMR spectra may be obtained for rapidly and isotropically mobile species in solution or highly and locally ordered solid-state species under conditions of magic angle spinning. In contrast, the relatively low-resolution solid-state NMR spectra obtained for amorphous gels reflect the broad distributions of molecular species and local disorder that are characteristic of poorly ordered or heterogeneous systems. Such diminished spectral resolution presents challenges for analyzing the molecular reorganization processes that occur in the amorphous phase during the initial stages of zeolite formation and also for heterogeneous, even crystalline, solid products. Such resolution challenges are exacerbated further in the case of quadrupolar nuclei ($I > 1/2$), such as ^{27}Al ($I = 5/2$), ^{23}Na ($I = 3/2$), ^{17}O ($I = 5/2$), ^{51}V ($I = 7/2$), etc., due to interactions of their nuclear quadrupole moments with local electric field gradients. Compared to spin $I = 1/2$ nuclei, such as ^{1}H, ^{13}C, ^{29}Si, etc., under similar conditions of conventional MAS, quadrupolar interactions are only partially averaged, leading often to significant centerband broadening from anisotropic second-order quadrupolar effects [48,49,59]. Such second-order quadrupolar interactions scale inversely with the strength of the externally applied magnetic field and so are mitigated by the use of high fields. Practical limitations, however, exist on the availability of very high homogeneous magnetic fields, so that quadrupolar effects are often present and must be confronted. Furthermore, since the electric field gradient around a given nucleus increases with decreasing symmetry of the nearby electronic environment [48], measurements of NMR spectra of quadrupolar nuclei in distorted environments, such as found in amorphous solids or at solid surfaces, are particularly challenging. In studies of crystalline zeolites, for example, deviations from tetrahedral or octahedral symmetry of distorted extra-framework or surface sites can lead to substantial broadening of ^{27}Al signals with high percentages of the total aluminum unobservable by ^{27}Al MAS NMR (so-called "NMR-invisible" aluminum species) [50–53].

Nevertheless, newly developed solid-state NMR techniques and approaches overcome a number of the challenges presented by quadrupolar nuclei with important implications for inorganic materials research. In particular, multiple-quantum MAS (MQ-MAS) [54–57] is now widely used to enhance the resolution of solid-state NMR spectra of half-integer quadrupolar nuclei by averaging anisotropic second-order quadrupolar interactions. MQ-MAS is an echo technique that correlates multiple-quantum (e.g., often triple-quantum) and single-quantum coherences under MAS conditions. In doing so, anisotropic interactions that frequently broaden the MAS spectra of non-integer spin $I > 1/2$ nuclei are averaged, while isotropic chemical shifts and isotropic second-order quadrupolar shifts are retained. Applying a conventional two-dimensional Fourier transformation of the MQ-MAS time-domain data yields frequency-domain spectra with ridge lineshapes that lie along an axis tilted by the MQ-MAS ratio (e.g., $-7/9$ for spin $I = 3/2$ or $+19/12$ for spin $I = 5/2$) for triple-quantum MAS. In this case, an isotropic spectrum can be obtained from a projection of the signal intensity orthogonal to the tilted axis, as opposed to a direct projection onto either of the frequency axes of the 2D spectrum. The isotropic chemical shift and isotropic second-order quadrupolar shift components associated with a given MQ-MAS signal can be extracted from the centers-of-gravity of the ridge lineshapes [57]. Often 2D MQ-MAS spectra are presented after a scaling transformation [58] that yields a 'sheared' spectrum, whose projection onto one of the axes (usually the indirectly detected dimension F_1) corresponds to the isotropic lineshape [e.g., as shown in Fig. 4]. In this case, the isotropic chemical shift and isotropic second-order quadrupolar shift can be calculated from the positions of each resolved isotropic signal and the center-of-gravity of their respective anisotropic lineshapes along the corresponding frequency axes [56]. The MQ-MAS technique has advantages over other line-narrowing methods for quadrupolar nuclei, such as Double Rotation (DOR) and Dynamic-Angle Spinning (DAS) [59], which include its use of conventional MAS probeheads that allow

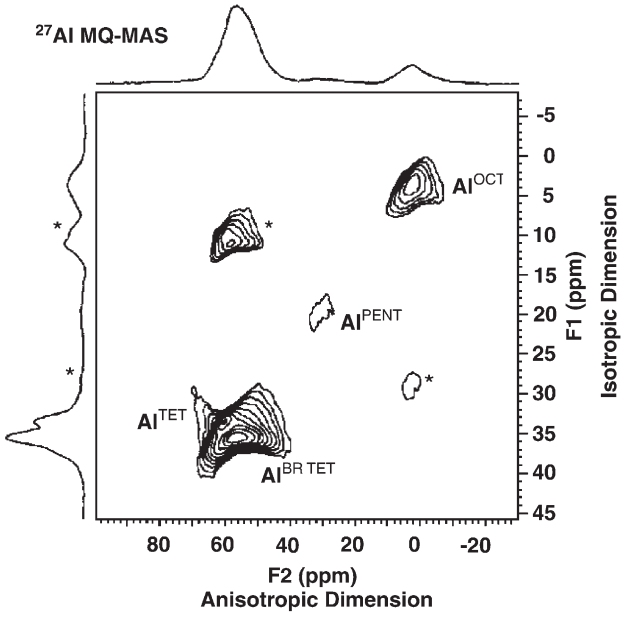

Fig. 4. ^{27}Al MQ-MAS of ultrastable-Y zeolite at a magnetic field strength of 18.8 T and MAS speed of 10.2 kHz. Peak assignments are given in the spectrum; asterisks denote spinning sidebands. The 1D spectra shown on the top and left side are projections along the corresponding axes. [Reprinted with permission from Ref. [62]. Copyright 2001 American Chemical Society.]

for high sample rotation speeds, variable temperature operation, and extraction of quadrupolar parameters without the need to acquire spectra at multiple magnetic field strengths.

MQ-MAS NMR methods are being applied to complicated inorganic solids, including minerals and zeolitic materials, shedding new insights on their molecular structures. For example, Alemany and co-workers [60] conducted a study of the limits of Al detectability for different NMR techniques using the mineral zoisite [orthorhombic $Ca_2Al_3Si_3O_{12}(OH)$] as a model compound. Zoisite contains two six-coordinated aluminum sites, one of which is significantly distorted. The authors demonstrated, that the distorted octahedral sites in zoisite could be observed in ^{27}Al MAS and ^{27}Al MQ-MAS experiments at magnetic field strengths of 11.7 T and higher using MAS speeds exceeding 30 kHz. Similarly, Fyfe et al. [61,62] have shown that ^{27}Al MQ-MAS NMR at very high magnetic field strengths (e.g., 18.8 T) allows ^{27}Al species to be measured in ultrastable-Y zeolite (USY), an important catalyst, formed by steam treatment and partial dealumination of zeolite HY. A 'sheared' 2D ^{27}Al MQ-MAS spectrum of USY in Fig. 4 clearly shows the presence of four distinct aluminum signals assigned to aluminum in tedrahedral (Al^{TET}), distorted tetrahedral ($Al^{BR.TET}$), penta-coordinated (Al^{PENT}), and octahedrally coordinated (Al^{OCT}) environments, as indicated. The two resonances marked with asterisks are spinning sidebands arising from the fast MAS conditions used. The isotropic ^{27}Al chemical shifts calculated for the resonances are 3.2 (Al^{OCT}), 32.2 (Al^{PENT}), 60.4 ($Al^{BR.TET}$), and 60.7 (Al^{TET}) ppm. The validity of the MQ-MAS analysis is supported by the fact that the parameters extracted from the MQ-MAS spectrum at 18.8 T could be used to simulate accurately the anisotropic ^{27}Al lineshapes in conventional MAS spectra measured at the same and lower magnetic field strengths. ^{27}Al MQ-MAS measurements, especially at high magnetic field strengths, show promise for elucidating the nature of distorted aluminum environments in zeolites, including previously "NMR invisible" quadrupolar species and structures of amorphous solids.

With respect to nucleation and growth mechanisms in zeolite syntheses, MQ-MAS NMR techniques provide insights into the evolution of local order in amorphous intermediate species prior to and during crystallization. For example, Yang et al. [63] studied by ^{27}Al and ^{23}Na MQ-MAS NMR the structures of amorphous aluminosilica phases that developed during the formation of zeolite A from an intermediate gel with the composition $1Al_2O_3{:}2SiO_2{:}3.06NaOH{:}128H_2O$. Fig. 5 shows a series of 2D ^{27}Al MQ-MAS NMR spectra presented without the shearing transformation applied, that were acquired under ex situ conditions for different solid samples recovered from identical reaction mixtures after heating for different lengths of time. The spectrum in Fig. 5(a) corresponds to the unreacted amorphous alumina starting material immediately after mixing with the other precursor components at room temperature. The spectrum contains two broad signals, one with an isotropic shift of 16.5 ppm attributed to six-coordinated aluminum species, and a second comprised of two unresolved components with isotropic shifts of ca. 60 and 63 ppm arising from four-coordinated Al sites [64]. After 0.5 h of reaction time, the ^{27}Al MQ-MAS spectrum in Fig. 5(b) shows only traces of six-coordinated aluminum, consistent with its conversion into a network with principally four-coordinated Al species. Spectra of otherwise identical samples acquired after longer reaction times [Fig. 5 (c)–(f)] contain exclusively signals arising from four-coordinated aluminum sites. With longer reaction times, the signal corresponding to four-coordinated Al species, furthermore, becomes sharper, consistent with increased local framework ordering as crystallization to zeolite A progresses.

The 2D ^{27}Al MQ-MAS spectrum of the sample extracted after 7 h treatment time [Fig. 5(d)] contains overlapping contributions from two signals in the region of four-coordinated aluminum: one resonance that corresponds to the amorphous material present at the beginning of the reaction and a significantly sharper signal attributed to crystalline zeolite A. The broad ^{27}Al signal arising from the amorphous material suggests that a range of Al–O bond distances and Si–O–Al bond angles are present, rather than the well-defined units containing rigorously alternating Si–O–Al moieties in zeolite A. With increasing reaction time, the broad signal becomes less and less intense, indicating the depletion of the disordered moieties in favor of a sharp signal at 61 ppm, which is exclusively present after 12 h of reaction time and attributed to highly crystalline zeolite A, consistent with separate XRD and neutron scattering experiments. These results are in good agreement with ^{29}Si{^{1}H} Cross-Polarization MAS (CP/MAS) NMR measurements on the same samples, which showed that the ^{29}Si signals also become significantly narrower after 7–8 h, consistent with the formation of crystalline zeolite A.

^{29}Si, ^{27}Al, and ^{23}Na MAS measurements (not shown here) collectively indicated that, in the early stages, silicon-rich regions were present during the synthesis of zeolite A, together with six-coordinated aluminum species that are associated with the amorphous alumina starting material. However, after short periods of heating and prior to the detectable onset of crystallization, aluminum is incorporated in the aluminosilica gel. Based on the broad ^{27}Al and ^{29}Si MAS signals observed, the amorphous aluminosilicas formed appear to possess a range of Al–O bond distances and Al–O–Si bond angles, as opposed to well-defined structural units present in the final crystalline zeolite A product. The incorporation of aluminum into the silicate framework is also accompanied by association with charge-compensating Na^+ cations, as indicated by an increase in the Na–O peak in radial distribution functions from neutron scattering data. These results are similar to those reported by Antonijevic et al. [65] for the formation of gallosilicate zeolites [66], for which similar ordering processes were observed by ^{71}Ga MAS NMR. The conversion of six-coordinated gallium species of the starting material into four-coordinated gallium atoms was monitored prior to crystallization. The combination of multinuclear solid-state NMR and correlated scattering studies provide valuable insights into the development and evolution of local order, even for poorly ordered intermediate species during crystallization of zeolites.

Similar transformation processes can occur from amorphous gels in the absence of solution phase species in so-called 'dry-gel' zeolite syntheses. In this method first introduced for the

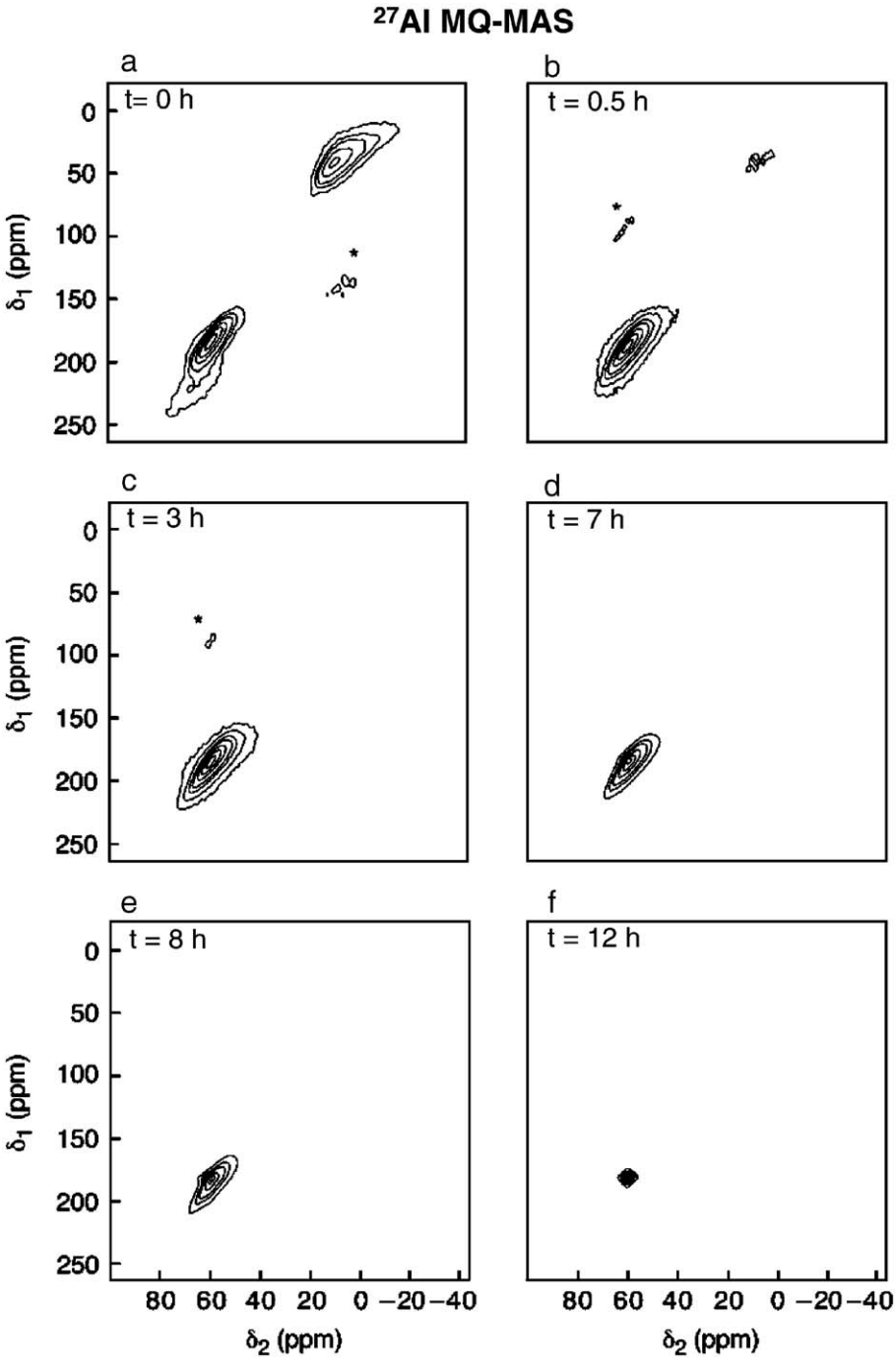

Fig. 5. Ex situ ^{27}Al MQ-MAS NMR spectra of zeolite A synthesis from an intermediate gel of composition $1Al_2O_3$:$2SiO_2$:3.06NaOH:$128H_2O$. Samples were heated to 100 °C for (a) 0 h, (b) 0.5 h, (c) 3 h, (d) 7 h, (e) 8 h and (f) 12 h. Contour levels are drawn at 4, 10, 20, 30, 50, 70 and 90% of the maximum intensities. [Adapted with permission from Ref. [63]. Copyright 2004 American Chemical Society.]

synthesis of ZSM-5 [67], a relatively dry gel was shown to develop into a highly crystalline zeolite product in the presence of water and vapors of volatile amines at temperatures of 180–200 °C. If non-volatile quaternary ammonium salts are required as structure-directing agents, they can be incorporated into the gel and only water supplied from the gas phase. Arnold et al. [68,69] studied the conversion of a dry-gel into zeolite Ga-Beta by means of ex situ ^{1}H MAS, ^{29}Si MAS, ^{71}Ga MAS, and ^{71}Ga MQ-MAS NMR. XRD powder patterns suggested that the formation of long-range tetrahedral-site order occurs relatively rapidly within the first 16 h of heating. Isotropic shift NMR measurements are also sensitive to the local electronic environments and thus to the distribution of isomorphously substituted Ga atoms. Decreases in the ^{29}Si and ^{71}Ga MAS line widths were observed to continue for ca. 65 h, implying that ordering of the local tetrahedral-site environment is completed

over a substantially longer time scale. Evolution of local structural order appeared to occur in two stages that could be differentiated by solid-state NMR. Initially, the conversion of the intermediate amorphous gel to the zeolite was dominated by the breaking of Si–O–Si bonds and subsequent formation of defect silanol groups, which allowed local structural adjustments into an increasingly ordered overall configuration. This was followed by condensation of terminal bonds, accompanied by the incorporation of gallium atoms into the silicate framework. This dry-gel process points to the possibility of formation mechanisms that are not necessarily influenced by soluble silicate anion species.

Nevertheless, evidence has been reported, that under certain conditions, zeolites may also grow by aggregation from pre-organized silicate anion species in solution. Burkett and Davis studied the formation of purely siliceous ZSM-5 by $^{29}Si\{^{1}H\}$ CP/MAS NMR [71] and proposed the existence of soluble pre-organized inorganic–organic composite structures in which the conformation of the tetrapropylammonium (TPA) cations is similar to that in the final zeolite product. During initial synthesis stages, hydrogen bonds between the organic cations and water-clathrated molecules are suggested to be progressively replaced by hydrophobic interactions between organic moieties and silica species [71,72]. These interactions may form in the liquid phase of the gel, leading to reduced mobility of the TPA cations, as evidenced by solution- and solid-state ^{1}H, ^{14}N, and ^{29}Si NMR measurements [73]. The pre-organized inorganic–organic composite precursors may then aggregate and the crystalline product can grow by diffusion of additional such composite precursors to the aggregate surfaces.

NMR measurements allow orientations and conformations of structure-directing organic molecules within zeolite pores to be established, shedding light on interactions that are central to the inorganic–organic co-crystallization process. In the final as-synthesized solid products, dipole–dipole interactions between distinct proton-containing moieties associated with organic structure-directing molecules and ^{29}Si and ^{27}Al sites in zeolite frameworks allow detailed molecular interactions and geometric relationships to be established [74]. For example, by using cross-polarization (CP/MAS) [70] or Rotational Echo Double Resonance (REDOR) [75,76], charge ordering between the structure-directing species and the zeolite framework can be observed, namely that the negative-charge centers of the zeolite frameworks appear to be directly associated with positive-charge centers of the structure-directing species [19,74,77]. $^{13}C\{^{1}H\}$ and $^{29}Si\{^{1}H\}$ CP/MAS measurements are also being widely used to characterize different isomers of organic structure-directing molecules and their orientations in zeolite cages [78–80]. These methods have also been used to follow the decomposition of new ketal-containing agents that are stable at the high pH values used in zeolite syntheses, but can be cleaved into ketones and diols at lower pH, thereby removing them from amorphous and crystalline zeolite products at moderate temperatures of 150 °C [81].

Formation mechanisms under similar reaction conditions might be significantly different for zeolites incorporating heteroatoms [82]. While no great differences have been encountered by the substitution of aluminum by gallium [65,66], Zones and Hwang studied the formation of borosilicate SSZ-42 and aluminosilicate zeolite BEA, which have different structures, from intermediate gels that were identical except for containing B_2O_3 or Al_2O_3, respectively [83]. By using ^{1}H, ^{11}B, and ^{27}Al MAS NMR in conjunction with X-ray scattering and elemental analysis, they found that the borosilicate system crystallized more rapidly then the aluminosilicate system, when both reactions were carried out in the presence of *N*-benzyl-diaza-bicyclo[2.2.2.]octane as a structure-directing agent. Based on a monotonic increase in the solid-state ^{11}B MAS NMR signal with time, the borosilicate zeolite crystals were concluded to grow by incorporation of both boron and silica from solution. By comparison, during the formation of the aluminosilicate zeolite, product elemental analysis and ^{27}Al NMR established that 95% of the available aluminum was in the solid-state independent of reaction time, either in the amorphous or the crystalline phase. ^{11}B and ^{27}Al NMR experiments, along with elemental analysis, of intermediate gels containing aluminum and boron also showed a constant aluminum content in the solid phase, while the boron content steadily increased. These observations and the different product structures suggest that the mechanisms of formation differ for the borosilicate and aluminosilicate molecular sieves in question, involving different extents of growth directly from solution species. Whether this is general for the formation of borosilicates remains unclear; in the presence of other structure-directing agents (i.e., *N*-benzyl-quinuclidine), boro- and aluminosilicates of the same structure type are known to be formed [84].

In the hydrothermal reaction of macroporous glass precursors [85–87], for instance, crystalline nanoporous borosilicates follow similar steps as observed for the formation of crystalline nanoporous aluminosilicates. Solid-state ^{11}B MAS experiments were conducted to follow the formation of MFI-type [86] and ZSM-5-type [87] boron-containing zeolites from porous glass spheres containing 93.7 wt.% SiO_2, 0.2 wt.% Na_2O, 0.1 wt.% Al_2O_3 and 6.0 wt.% B_2O_3. In a first reaction step, the porous glass granules were partially dissolved in alkaline solutions of sodium aluminate or aluminum sulfate. In situ ^{11}B MAS measurements allow solution- and solid-state boron species to be clearly distinguished, indicating that $B_5O_6(OH)_4^-$ ions form in solution prior to heating. A strong decrease in the intensities of ^{11}B MAS signals from trigonal boron species associated with the precursor glass was used to conclude that preferential leaching of trigonal boron from the glass granules occurs. After heating, two additional signals arise in the ^{11}B MAS spectrum from rapidly exchanging tetrahedral and trigonal boron hydroxyl species. ^{27}Al MAS measurements suggest that, in a second synthesis stage, four-coordinated aluminum species in solution are rapidly complexed or adsorbed on the surface of the glass granules, followed by transformation of the amorphous framework into crystalline zeolite structures, as evidenced by ^{11}B MAS NMR and XRD. In the case of the formation of ZSM-5-type zeolites, the ^{11}B NMR data suggest that transformation of four-coordinated boron atoms remaining in the glass occurs after the dissolution of trigonal boron species. In contrast, for the

case of MFI-type zeolites, the decrease of four-coordinated boron species in solution implies that they are involved in the formation of the MFI-type framework. Scanning Electron Microscopy (SEM) measurements of the zeolitic products show that the macroscopic physical shapes of the macroporous glass granules are preserved during the transformation, suggesting crystallization from the amorphous precursor materials.

2.2. Structures and roles of intermediate nanoparticles in zeolite growth

The growth mechanism and structures of intermediate silicate species in clear alkaline solutions have been most extensively studied and controversially debated in the case of syntheses of the zeolite silicalite-1 (siliceous ZSM-5) in the presence of tetrapropylammonium (TPA) cations. Schoeman et al. [88,89] reported intermediate silicate species that were identified and studied by light-scattering and cryo-transmission electron microscopy (cryo-TEM). Since then, this system has been the subject of detailed study by a variety of techniques, including TEM, small-angle X-ray scattering (SAXS), atomic force microscopy (AFM), in situ X-ray scattering, gel permeation chromatography, and ^{29}Si MAS NMR [90–102]. Based on their measurements, Kirschhock et al. [90–92] concluded that extracted block-like intermediate species of 1–4 nm in length possessed the MFI topology of the eventual silicalite-1 product and accordingly termed the species silicalite-1 nanoblocks or nanoslabs. It was suggested that after the formation of nanoslabs at room temperature, aggregation of these species into larger structural intermediates and their fusion to form the final zeolite product then proceeds at elevated temperatures. The intermediate nanoparticles were formed in a sol that was prepared according to the procedure of Ref. [88] by the addition of tetraethylorthosilicate (TEOS) to a 40% aqueous solution of TPA hydroxide. The nanoparticles were extracted by subsequent acidification to pH = 3 with HCl and the addition of *tert*-butyl alcohol and NaCl as hydrogen-bonding and 'salting-out' agents, respectively [92]. Spectrum 3 in Fig. 6(a) shows the one-pulse ^{29}Si MAS spectrum of the extracted nanoparticles, which can be deconvoluted into three peaks at −92 ppm, −101 ppm, and −110 ppm, representing Q^2, Q^3, and Q^4 silicon species with relative intensities of 8%, 41%, and 51%, respectively [spectrum 4, Fig. 6(a)]. The peaks are somewhat narrower than those of amorphous silica aerosil (spectrum 1) and comparable to those of mesoporous MCM-41 (spectrum 2), as shown in Fig. 6(a). The same peaks are present in the ^{29}Si{^{1}H} CP/MAS (spectrum 5), but with the relative intensities of the Q^2 and Q^3 signals enhanced by cross-polarization from nearby proton species. The relative concentrations of Q^2, Q^3, and Q^4 silicon species were compared to Q^n distributions modeled for cubic, spherical, and slab-shaped particles with the MFI-topology for various particle sizes. The best fit was found for slab-shaped particles of 4-nm length along both the *b* and *c* crystallographic directions and 1.3 nm along the *a*-direction. Fig. 6(b) shows a proposed structure for the nanoslabs, which contains nine channel intersections that could host TPA molecules, a number that is consistent with the TPA content measured from thermogravimetric analyses.

The proposed zeolite synthesis mechanism based on nanoslab nucleation and growth has led to a vibrant debate in the literature that is still underway at the time of this review. New experimental results and analyses are appearing in the literature from independent groups, which scrutinize the case for the nanoslabs and which in some cases are leading to

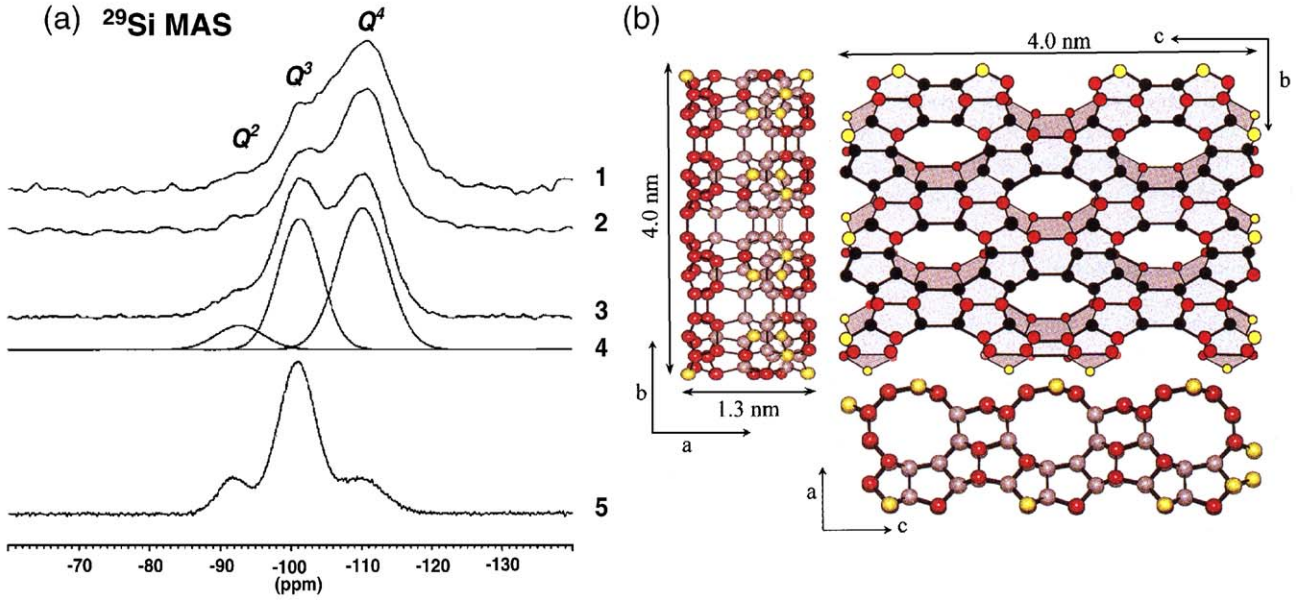

Fig. 6. (a) (1)–(3) ^{29}Si MAS NMR spectra of (1) Aerosil, (2) MCM-41, (3) nanoparticles extracted during clear solution synthesis of silicalite-1 with MAS at 4 kHz and (4) deconvolution of spectrum (3). (5) ^{29}Si{^{1}H} CP/MAS NMR of the same particles as measured in (3). (b) Schematic structure of a silicalite-1 nanoslab obtained by modeling the NMR data. [Adapted with permission from Ref. [92]. Copyright 1999 American Chemical Society.]

countervailing hypotheses. For example, AFM and TEM measurements [95] have recently been reported that find no evidence for block-shaped nanoparticles after drying the as-synthesized clear suspension. Ramanan et al. suggested that NaCl crystals dispersed in the organic-rich phase may have been misinterpreted as nanoslabs in the TEM data of Ref. [90]. In response, Kirschhock et al. [91] countered that NaCl does not form the observed entities, although the nanoslabs may be "stabilized on the NaCl crystals," which may serve as epitaxially compatible growth substrates. A "protective TPA layer" surrounding the external periphery of the anionic nanoslabs is suggested to passivate the nanoslabs against condensation and degradation reactions. In another study, Kragten et al. [96] extracted nanoparticles according to the procedure of Ref. [88] and studied the isolated material by XRD, FTIR spectroscopy, thermogravimetric analysis, N_2 adsorption isotherms, and ^{29}Si MAS NMR. The FTIR, TGA and ^{29}Si MAS results from the extracted intermediate material are in good agreement with the results from preceding literature reports [90,92,93], appearing to establish consensus concerning these measurements. The TGA data suggest that the extracted nanoparticles most likely include TPA^+, though they are separated by a "bulklike TPA-condensate." Comparison of experimental and simulated XRD patterns of the extracted material and amorphous silica, however, indicated that the extracted nanoparticles were amorphous, in contrast to the proposed well-defined nanoslabs. In good agreement with Ref. [92], the ^{29}Si MAS spectrum showed three peaks at -94, -103, and -112 ppm, representing Q^2, Q^3, and Q^4 silicon species with relative intensities of the peaks 6%, 44%, and 50%, respectively [96]. The authors remarked that internal silanol defects that compensate for the charge of the TPA^+ cation can amount to as much as 17% of the peak area [97] not accounted for by the modeling of the NMR data in Ref. [92]. Kragten et al. used a simulated annealing method to fit the ^{29}Si MAS data using calculations starting from building units of 12 $SiO_{4/2}$ units in one approach and from single $SiO_{4/2}$ building units in the other case [96]. The modeling led to a range of nanoparticle structures with open shapes and a considerable amount of internal defects fitting the ^{29}Si MAS data. Fig. 7 shows the final structures obtained by the two fitting approaches. The structures generated from 12-$SiO_{4/2}$ building units exhibit shape variations, but are primarily rods, while the single $SiO_{4/2}$ building units yield open structures with no well-defined shapes and 15% internal Q^3 and Q^2 species. An additional small-angle neutron scattering (SANS) and ^{29}Si NMR study of the nanoparticles in solution led to the determination of an ellipsoidal mean shape of the nanoparticle with minor and major radii of 1.0 and 2.2 nm, respectively [98]. Further SANS and SAXS measurements showed that these particles have a core-shell structure with a TPA shell and a silica core [99]. ^{29}Si MAS NMR measurements suggest that this core is predominantly composed of Q^3 silica species [100], in contrast to crystalline silicalite-1 that mainly consists of Q^4 species. If subjected to hydrothermal treatment, these particles appear to grow via an Ostwald-ripening mechanism, with growth rates dependent on pH and temperature [101].

The differing interpretations of essentially identical ^{29}Si MAS NMR spectra in Refs. [92,96] demonstrate that it is often difficult to determine unambiguously particle structures from 1D NMR data, with the result that the structure of nanoparticles extracted during the synthesis of silicalite-1 remains controversial. The interpretation of the data might additionally be complicated by the possibility of distributions in the structures and/or sizes of the nanoparticles [102]. An unambiguous structure determination of the nanoparticles is clearly needed to resolve this controversy, but remains elusive so far, since powder XRD measurements are also not conclusive and no large single-crystals are of course available. Further structural information of these particles may come from recent 2D NMR approaches that exploit ^{29}Si–^{29}Si homonuclear dipole–dipole or scalar (J) couplings to analyze the molecular structures of siliceous zeolites [103] and mesostructured silicates [104]. In particular, the application of 2D ^{29}Si{^{29}Si} NMR methods may yield ^{29}Si site connectivities and detailed information on local nanoparticle structure(s).

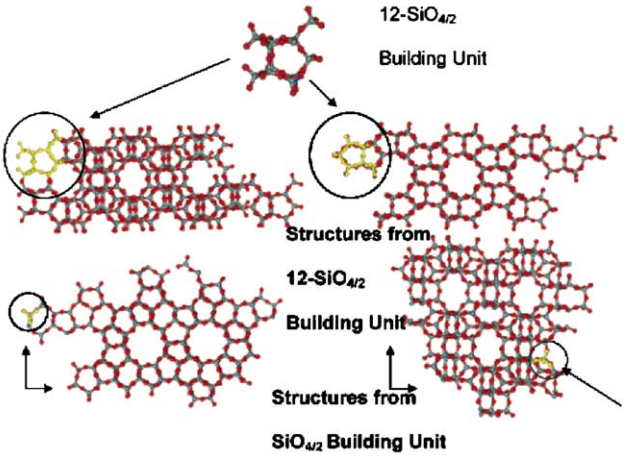

Fig. 7. (a) Structures obtained by fitting ^{29}Si NMR MAS spectra of nanoparticles extracted in the same fashion as those in Fig. 6(a)(3). The top two structures are generated from 12-$SiO_{4/2}$ building units, the lower two from $SiO_{4/2}$ building units [Adapted with permission from Ref. [96]. Copyright 2003 American Chemical Society.]

One approach demonstrated by Brouwer et al. [103] combines powder XRD with solid-state NMR spectroscopy to determine the structures of two siliceous zeolites containing ^{29}Si in natural abundance (4.7%). Fig. 8 shows a schematic overview of their procedure in which unit cell parameters and the space group are determined in the conventional way by powder XRD and the "structure solution" refined by using solid-state homonuclear Double-Quantum (DQ) correlation ^{29}Si{^{29}Si} NMR [105]. The double-quantum method uses a series of pulses that are applied for a specified amount of time to reintroduce homonuclear dipole–dipole interactions that are otherwise averaged to zero under fast MAS conditions. The cross-peaks in a 2D DQ correlation spectrum [e.g., Fig. 8, upper middle spectrum] are associated with dipole–dipole-coupled spin pairs, the intensities of which increase with the strength of the coupling between the two sites and the length of the recoupling time. Since the strength of the dipole–dipole interaction between two nuclei is inversely proportional to the cube of their separation distance, the intensities of the cross-peaks are high for closely spaced, strongly coupled sites. Brouwer et al. used sufficiently short recoupling times (~6 ms), so that cross-peaks in 2D DQ ^{29}Si{^{29}Si} correlation spectra arose primarily for ^{29}Si–^{29}Si spin pairs coupled via bridging oxygen atoms, revealing ^{29}Si–O–^{29}Si site interconnectivities. Additional information on longer range ^{29}Si–^{29}Si distances was obtained by measuring a series of 2D DQ ^{29}Si{^{29}Si} correlation spectra with increasing recoupling times. By plotting the cross-peak intensities as functions of the recoupling time [e.g., Fig. 8, upper, right], double-quantum buildup curves can be produced for each resolved cross-peak pair. Such curves are highly sensitive to ^{29}Si–^{29}Si spin-pair distances and can be simulated for different ^{29}Si–O–^{29}Si distances up to ~0.8 nm [106]. The authors developed an algorithm for determining zeolite crystal structures from the number and occupancies of tetrahedrally coordinated Si sites, and their interconnectivities from DQ ^{29}Si{^{29}Si} NMR, ^{29}Si–O–^{29}Si distance information from the DQ ^{29}Si{^{29}Si} intensity buildup curves for each of the different pairs of coupled spins, and the unit cell parameters and space group from XRD. The structure solution can then be refined against the XRD powder pattern by using the Rietveld method. The feasibility of this approach was demonstrated by the correct blind structure determination and identification of two siliceous zeolites ITQ-4 and ferrierite. A limiting factor of the method is that different crystallographic Si sites must give rise to distinct resolved ^{29}Si NMR signals, which is not the case for most aluminosilicate zeolites or other heteroatom-containing molecular sieves, in which appreciable local composition disorder is generally present. In addition to the detailed structural analyses of siliceous molecular sieves that this approach permits, it might also provide helpful insights on the structures of siliceous nanoparticles extracted during the formation of silicalite-1, provided sufficient ^{29}Si signal sensitivity is obtained.

2.3. Formation mechanisms of aluminophosphate molecular sieves

In contrast to aluminosilicate molecular sieves, which are generally prepared from alkaline solutions, aluminophosphate-based molecular sieves ($AlPO_4$s) can be synthesized under acidic, neutral, or in some cases slightly basic conditions. The vast majority of these materials are prepared by hydrothermal syntheses in acidic solutions with pH-values between 4 and 6.5, at temperatures between 130 °C and 200 °C, and in the presence of organic amines or alkylammonium cations [4,5,107,108]. A wide variety of $AlPO_4$ molecular sieve materials have been prepared and the influence of the synthesis conditions on the final products has been extensively studied. Due to the favorable NMR properties of the ^{27}Al (spin I=5/2, 100% nat. abund.) and ^{31}P (spin I=1/2, 100% nat. abund.) nuclei, solid-state NMR has been widely used to characterize the framework

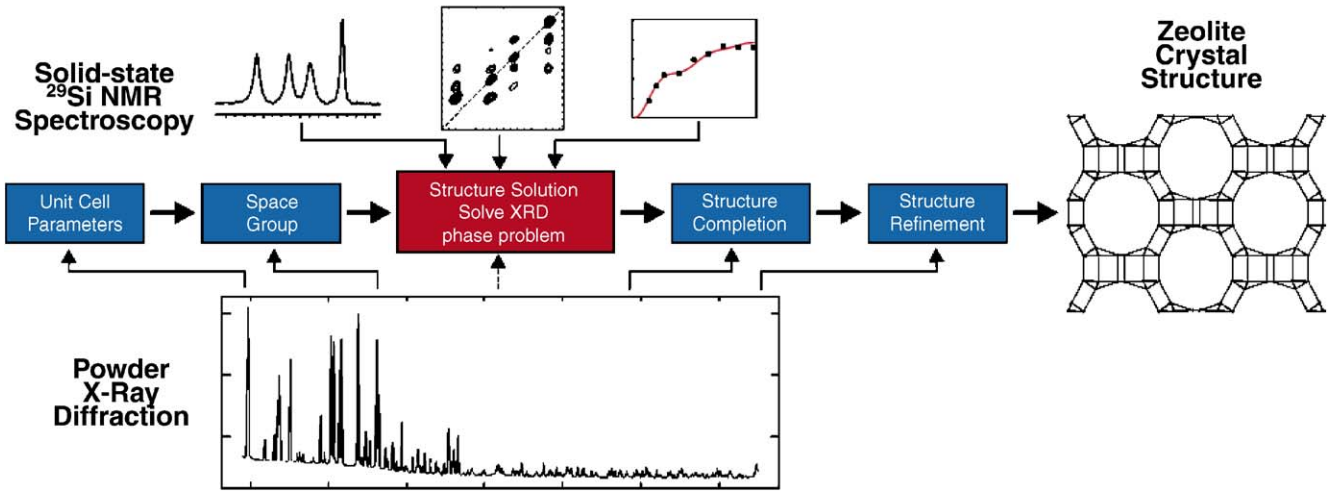

Fig. 8. Schematic overview of the structure determination proposed for zeolite crystals combining powder X-ray diffraction experiments and solid-state ^{29}Si double quantum NMR experiments. [Reprinted with permission from Ref. [103]. Copyright 2005 American Chemical Society.]

structures of $AlPO_4$-based materials (e.g., [11,109]) and more recently, the molecular mechanisms of their formation under hydrothermal conditions [110].

As in the case of zeolites, the preparation of crystalline aluminophosphate molecular sieves involves the early-stage formation of intermediate amorphous gels, which upon heating transform to crystalline $AlPO_4$ materials. Taulelle et al. [111] reported an in situ ^{19}F, ^{27}Al, and ^{31}P NMR study of the formation of nanoporous aluminophosphate $AlPO_4$–CJ2 with the composition $(NH_4)_{0.88}(H_3O)_{0.12}$–$AlPO_4(OH)_{0.33}F_{0.67}$, applying a quantitative in situ NMR approach developed by their group [112]. The authors carried out in situ NMR measurements, as well as ex-situ MAS NMR analyses of the solid phases extracted from a hydrothermal reaction mixture after different reaction times. In addition, they used the pH-sensitive ^{14}N NMR chemical shifts of imidazole and DABCO (1,4-DiAzaBiCyclo-2,2,2-Octane) to monitor in situ the acidity of the hydrothermal reaction solution [113]. The combined NMR results suggest that at the initial stage of the reaction an amorphous $Al(OH)_3$ phase is formed, which disappears rapidly, as another amorphous phase containing fluoride and phosphate moieties $Al(OH,F)_x(H_nPO_4)_y$ is formed. The subsequent dissolution of this second intermediate phase is accompanied by a sharp increase in the pH from 3 to 6, after which the acidity of the solution remains approximately constant for the next 4–5 h of reaction. During dissolution of this amorphous phase, crystalline $AlPO_4$–CJ2 and small amounts of $AlPO_4$–A form slowly. The formation of these materials is substantially slower than the dissolution of the amorphous phase, leading to a decrease of the overall solid fraction present in the hydrothermal reaction mixture.

The formation of crystalline $AlPO_4$–A competes with the formation of $AlPO_4$–CJ2 in the first hours of reaction, but the former eventually disappears. During the latter stages of the reaction, dissolution of the amorphous phase slows, while the formation of crystalline $AlPO_4$–CJ2 product continues. In situ ^{27}Al NMR measurements exhibit two peaks at −40 ppm and at −48 ppm that are attributed to five-coordinated aluminum species in the hydrothermal solution [111,112]. In the presence of fluoride, penta-coordinated aluminum is stable in aqueous solution at neutral pH. Temperature-dependent in situ ^{27}Al NMR measurements of the reaction mixture show that the signal at −40 ppm moves to 0 ppm at lower temperatures, indicating a coordination change to six-coordinated aluminum species, while the signal at −48 ppm is not affected by temperature changes. The authors suggest that the penta-coordinated Al species associated with the signal at −40 ppm are most likely fluoro-aluminophosphate units, in which aluminum atoms are linked to a phosphate atom via a bridging oxygen atom, plus being coordinated by three OH-groups and a fluorine atom. These five-coordinated aluminum moieties are formed in solution from six-coordinated aluminum species by the loss of water in the coordination sphere upon heating. The signal at −48 ppm is assigned to cyclic tetrameric units formed by the monomer fluoro-aluminophosphate species, which could then condense to form the crystalline aluminophosphate product. Compared to the tetramer, the $AlPO_4$–CJ2 structure contains an additional link between two of the aluminum atoms in a tetrameric ring by an F atom or OH group, leading to the formation of six-coordinated aluminum sites in the final product, which were not observed in solution.

The roles of soluble aluminophosphate species in the syntheses of silicon aluminophosphate (SAPO) molecular sieves were studied by similar NMR techniques as those used to follow the formation of the nanoporous $AlPO_4$s. Vistad et al. presented a detailed study of the formation of SAPO-34 from intermediate gels with a composition $1SiO_2$:$1Al_2O_3$:$1P_2O_5$: 2.1morpholine:1HF:$60H_2O$ by in situ ^{13}C, ^{19}F, ^{27}Al, and ^{31}P NMR [114], pH-sensitive ^{13}C NMR [115] and XRD measurements [116]. The mechanism the authors proposed, based on their combined NMR and XRD results, is depicted in Fig. 9(a). The initial hydrothermal solution at pH = 5.5 contained free phosphates and fluoroaluminophosphate and aluminophosphate complexes, as indicated by solution-state ^{19}F, ^{27}Al, and ^{31}P NMR. The broad peak centered at ca. 0 ppm in the bottom ^{27}Al spectrum of Fig. 9(b) indicates that the aluminum species present were six-coordinated in these complexes. The relatively large width of the solution-state ^{27}Al NMR peaks further suggests that these complexes do not exist as monomers in solution but rather as a distribution of species. The high charge density of the morpholinium cation present in solution apparently disfavors the presence of counter-anions larger than four-ring (4R) silicate species. Four-ring species were also observed in in situ XRD data, leading the authors to suggest that the 4R type-1 unit of Fig. 9(a) is a likely species to be present in solution upon dissolution of the intermediate gel. Upon the first stage of heating (<95 °C), the gel is dissolved further, as indicated by an increase in the overall intensity of the solution-state ^{27}Al NMR spectra. Over the temperature range 95–120 °C, a solid layered $AlPO_4F$ intermediate ("prephase") appears to form, the structure of which was determined by XRD to consist of $AlPO_4F$ sheets separated by an ordered double layer of protonated morpholine molecules, as depicted in Fig. 9(a), top.

In a separate experiment it was shown that, under hydrothermal conditions, the layered $AlPO_4F$ prephase could transform into SAPO-34, from which it was concluded that no additional soluble species were necessary for the formation of SAPO-34 from the prephase [114]. The formation of the solid prephase was accompanied by an increase in pH from 5.5 to 7.3 and an overall decrease in the intensity of the solution-state ^{27}Al NMR spectra. When the temperature was further raised above 120 °C, the prephase dissolved, again forming fluorine-rich four-ring type-II units in solution. These species transformed by defluorination into type-III four-ring units containing penta-coordinated aluminum, as indicated by the shift in the ^{27}Al chemical shift from 0 ppm to 45.5 ppm. The stabilization of penta-coordinated aluminum species at neutral pH and at elevated temperatures in the presence of fluoride was shown during the formation of $AlPO_4$–CJ2 discussed above. Further loss of fluoride led to type-V four-ring units, with the crystallization of SAPO-34 proposed to occur by the condensation of the type-III and type-V four-ring species. The

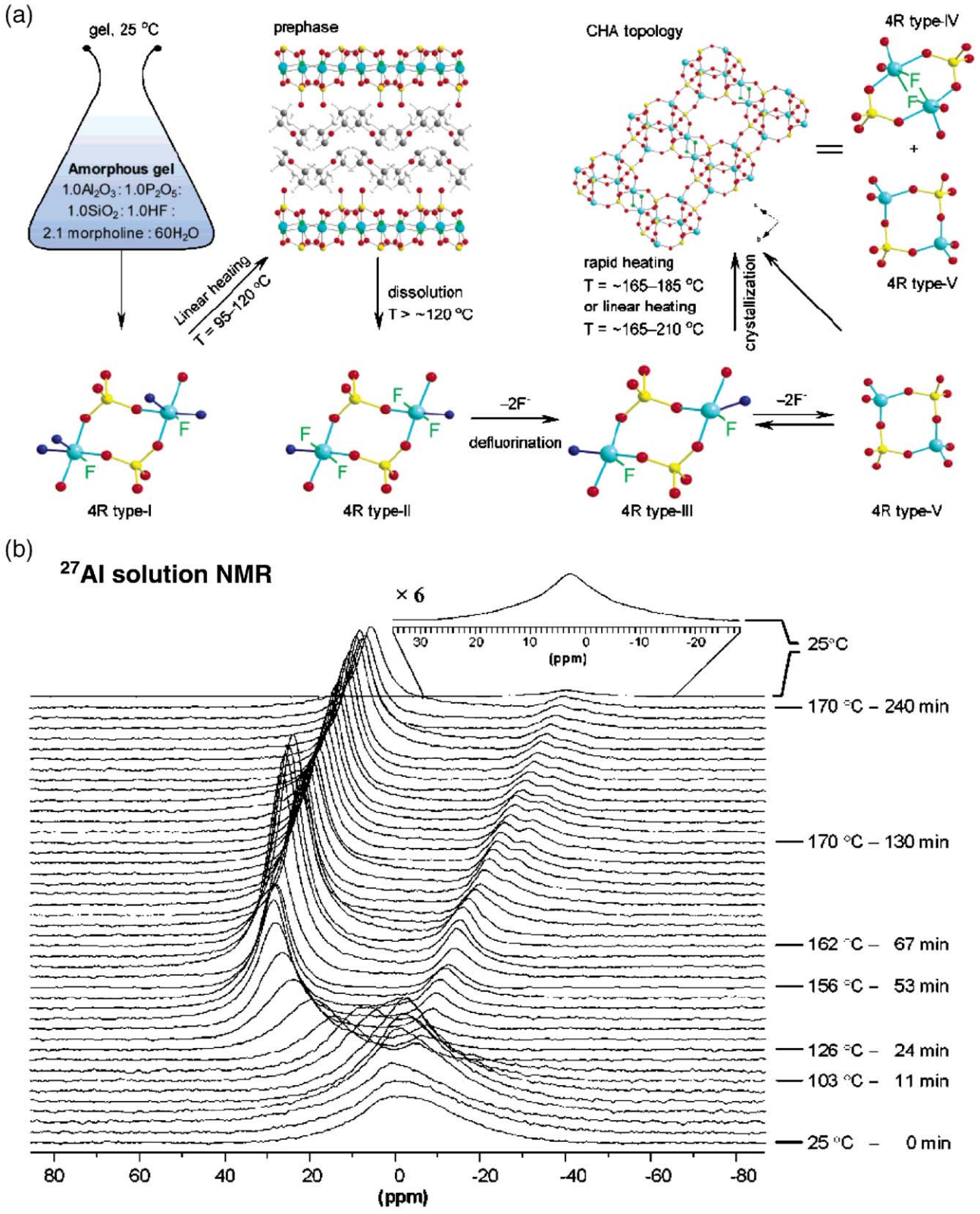

Fig. 9. (a) Schematic overview of the proposed mechanism of SAPO-34 formation from in situ NMR and XRD measurements. (b) Stacked plot of in situ ^{27}Al NMR spectra during the formation of triclinic SAPO-34. The *x*-axis scales of the spectra increase by 1 ppm/spectrum from bottom to top. [Reprinted with permission from Ref. [114]. Copyright 2003 American Chemical Society.]

defluorination is reflected by an increase in the pH to 8.6 and accompanying increase in the overall intensity of the solution-state ^{19}F NMR signal [114]. Although the intermediate gel contained a substantial amount of silicon, in situ ^{29}Si NMR spectra could not be recorded due to the low ^{29}Si signal sensitivity, so no direct evidence for the mechanism of silicon incorporation in SAPO-34 was provided. When, the synthesis was carried out in the absence of silicon, very little change in the in situ ^{19}F, ^{27}Al, and ^{31}P NMR spectra were observed. These results suggest, that the incorporation of silicon may proceed by the substitution of phosphorous or aluminum in the type-I four-ring units. Ex situ solid-state NMR, XRD, and Raman experiments on the intermediate phases of SAPO-44 formation by Huang et al. are consistent with such late incorporation of silicon into the framework [117]. It remains however not generally established, whether the aluminophosphate species

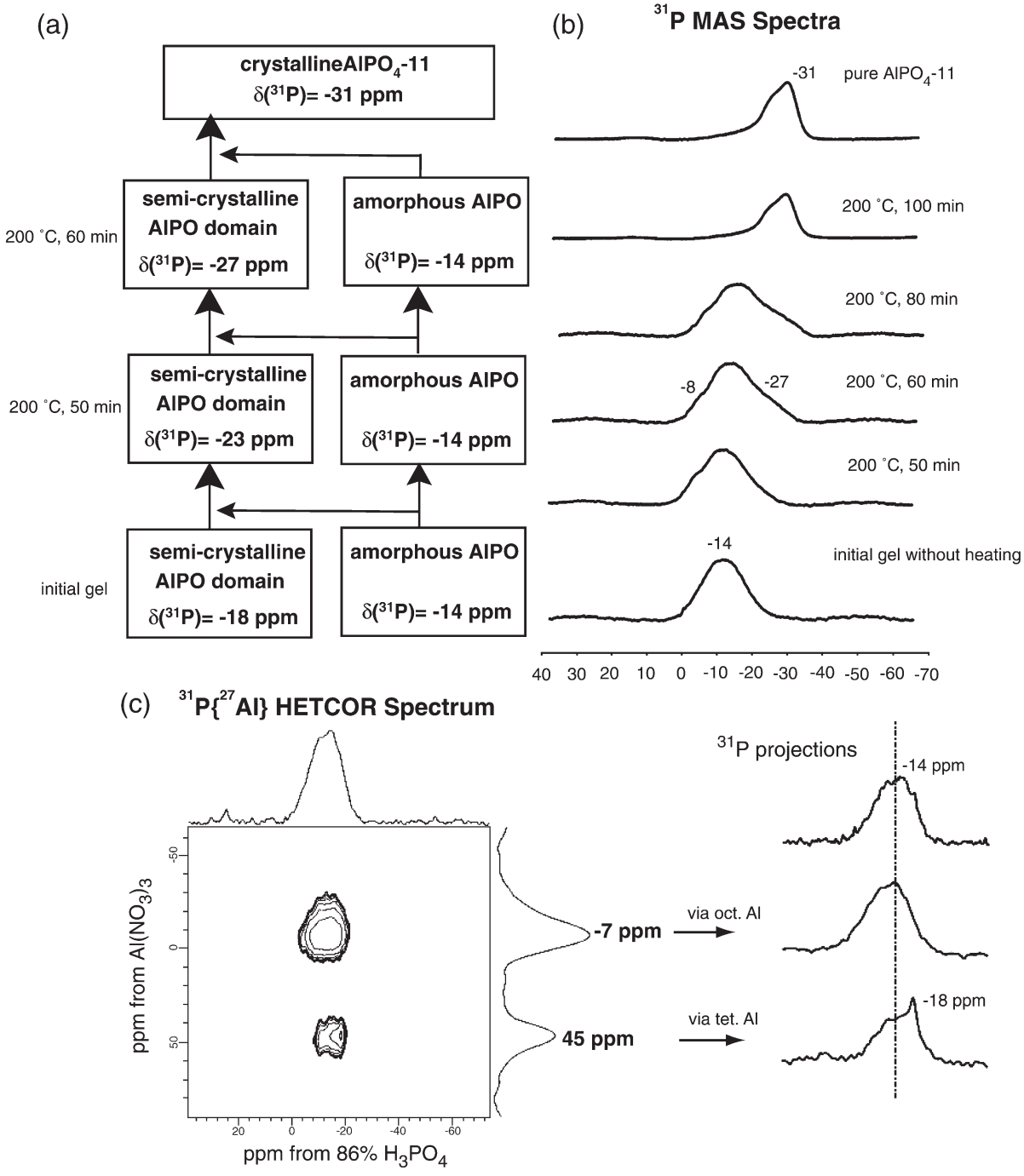

Fig. 10. (a) Evolution of different phases during the formation of $AlPO_4$-11 from an intermediate gel of composition $1Al_2O_3$:$1P_2O_3$:1DPA:$40H_2O$. (b) ^{31}P MAS NMR spectra at various stages of $AlPO_4$-11 formation. (c) 2D $^{31}P\{^{27}Al\}$ HETCOR NMR spectrum of the initial gel sample and projection along the ^{31}P dimension. [Adapted with permission from Ref. [118]. Copyright 2003 American Chemical Society.]

found in solution directly link to form the crystalline $AlPO_4$ or SAPO materials or whether they interact with small seed crystals in the amorphous gel phases.

The changes in intermediate gel phases during the nucleation and growth of $AlPO_4$ molecular sieves have been investigated by ex-situ solid-state NMR [118]. For example, Fig. 10(a) summarizes the evolution of amorphous and semi-crystalline aluminophosphate domains during the formation of $AlPO_4$-11, as indicated by the ^{31}P MAS NMR measurements shown in Fig. 10(b). The initial synthesis gel after aging consists of an amorphous aluminophosphate intermediate phase, represented by a broad peak centered at −14 ppm in the ^{31}P MAS spectrum. Although the nature of the amorphous phase cannot be determined from the single-pulse ^{31}P NMR spectrum unambiguously, $^{31}P\{^{27}Al\}$ CP/MAS NMR measurements established that the aluminum and phosphorus species were in close spatial proximity [119], consistent with the existence of an aluminophosphate network in the amorphous phase. Three aluminum species in the amorphous phase could be clearly identified by ^{27}Al MQ-MAS measurements: one signal could be unambiguously assigned to four-coordinated ^{27}Al sites in aluminophosphate moieties, the other two could either be due to six- or five-coordinated ^{27}Al species in unreacted alumina or aluminophosphate species. The 2D $^{31}P\{^{27}Al\}$ HETeronuclear chemical shift CORrelation (HETCOR) [118] measurements in Fig. 10(c) show a clear correlation of the broad ^{31}P signal to the four-coordinated aluminum site at 45 ppm and the six-coordinated ^{27}Al signal at −7 ppm. However, no correlation was observed to the third signal. Therefore, this uncorrelated ^{27}Al signal likely corresponds to unreacted alumina. This points to a composition of $P(OH)_x[OAl^{tet}]_y[OAl^{oct}]_{4-(x+y)}$, where $x,y=1$ or 2, with the presence of P–OH groups in the material being separately supported by $^{31}P\{^{1}H\}$ CP/MAS results. Projections of the $^{31}P\{^{27}Al\}$ HETCOR spectrum also reveal that the broad ^{31}P peak at 14 ppm contains a shoulder at about −18 ppm in the ^{31}P NMR spectrum, assigned to a phosphorus species linked to four-coordinated aluminum sites via bridging oxygen atoms and also to at least two four-coordinated phosphorus species in a semicrystalline aluminophosphate material. After heating the gel to 200 °C for 60 min, shoulders in the ^{31}P MAS NMR spectrum at −8 ppm and −27 ppm become evident, as shown in Fig. 10(b). Since no HETCOR intensity correlation to ^{27}Al is found for the −8-ppm ^{31}P resonance, it is attributed to a phosphate species in an amorphous material without ^{27}Al species nearby (>1 nm). The shoulder at −27 ppm displays correlated $^{31}P\{^{27}Al\}$ HETCOR intensity and so is assigned to ^{31}P in semicrystalline aluminophosphate environments, similar to the −14 ppm resonance in the initial gel. The reduced ^{31}P chemical shift indicates a greater extent of condensation of this phosphorus species after heating for 60 min, as confirmed by $^{31}P\{^{27}Al\}$ HETCOR and $^{31}P\{^{27}Al\}$ TRAnsfer of Populations in DOuble Resonance (TRAPDOR) [118] measurements. As shown in Fig. 10(b) this signal moves toward lower ^{31}P chemical shift values at longer reaction times, consistent with the increased condensation of the $AlPO_4$ network and supported by separate XRD measurements, which indicate the presence of an intermediate semicrystalline phase. For heating times longer than 100 min, the solid-state ^{31}P MAS spectra exhibit a resonance at −31 ppm corresponding to crystalline $AlPO_4$, in accordance with corroborative ^{27}Al MAS and XRD results.

Thus, combined solution- and solid-state multinuclear NMR results, in conjunction with X-ray scattering, suggest that an amorphous aluminophosphate gel is initially formed, followed by a semicrystalline aluminophosphate intermediate that further condenses upon heating and finally transforms into crystalline $AlPO_4$-11 [118]. In the initial gel and for heating times up to 60 min, small fractions of the semicrystalline intermediate already coexist with the amorphous aluminophosphate and can be monitored in detail by double-resonance NMR methods (e.g., CP/MAS, HETCOR [120], or TRAPDOR [121]) that provide filtering via heteronuclear ^{31}P–^{27}Al dipole–dipole interactions. In a similar study of the formation of $AlPO_4$-18 by the same group [122], no evidence for a semi-crystalline intermediate was found. In that case, the initial gel that was formed by mixing the Al and P sources in the presence of tetraethylammonium hydroxide and HCl consisted of an ordered aluminophosphate material, which contained only four-coordinated aluminum species and a phosphate phase of unknown nature. During hydrothermal treatment at 150 °C for 1 h, however, this ordered phase disappeared entirely in favor of an amorphous aluminophosphate material containing four- and six-coordinated aluminum species. This material subsequently transformed into microporous $AlPO_4$-5 after heating for 2 h, with a pure crystalline $AlPO_4$-5 phase obtained after 24 h. Continued heat treatment up to 72 h promoted further transformation into crystalline molecular sieve $AlPO_4$-18. Similar reaction paths via amorphous gels were evidenced by ex situ ^{27}Al and ^{31}P MAS NMR during the formation of AlPO-HDA [123] and $AlPO_4$-21 [124]. Solid-state ^{27}Al and ^{31}P NMR measurements, thus, appear to support $AlPO_4$ crystallization mechanisms that involve transformations from amorphous aluminophosphate phases.

For silicon-containing $AlPO_4$ molecular sieves, ex situ solid-state NMR, XRD, and Raman measurements allow similar structural changes to be followed, together with the kinetics of heteroatom incorporation. For example, Huang et al. [117] followed the formation of SAPO-44 and showed that the initial gel prior to hydrothermal treatment contains predominantly the unreacted source materials, with only a small amount of amorphous $AlPO_4$ material present. After 2 h of hydrothermal treatment at 190 °C, the solid phase consisted of an amorphous $AlPO_4$ material with two phosphorus sites that were not fully condensed and a crystalline $AlPO_4$ intermediate, which were unambiguously determined from $^{31}P\{^{27}Al\}$ HETCOR measurements. In accordance with Ref. [114], after 3 h of heating, silicon atoms were incorporated into the $AlPO_4$ framework. Such relatively late incorporation was established by solid-state $^{29}Si\{^{27}Al\}$ TEDOR NMR measurements that are sensitive to the ^{29}Si–^{27}Al distances in the products. After heating for 6 h, a crystalline intermediate with a layered structure emerged, which subsequently diminished in favor of the final crystalline SAPO-44 product. These studies show that the complementary use of solution- and solid-state NMR techniques provide detailed

information about different stages of the formation of $AlPO_4$ and SAPO materials.

3. Nucleation of ordered inorganic mesophase materials

Whereas zeolites rely on the use of small-molecules to direct the structures of crystallizing inorganic frameworks, the use of self-assembled aggregates of surfactant molecules allows inorganic–organic composites and porous inorganic solids to be prepared over a wide range of compositions with uniform ordering length scales from 3–50 nm. Typical syntheses of ordered mesoporous materials exploit the properties of amphiphilic surfactant molecules, which are composed of well-demarcated hydrophilic and hydrophobic moieties that self-organize in polar solutions into aggregated molecular assemblies, such as micelles, spheres, cylinders, or lamellae. In concentrated phases, such aggregates often form ordered mesophases, e.g., liquid crystals, whose self-assembly properties can be used to direct the structures of network-forming inorganic species. Conditions are selected that promote preferential interactions between inorganic precursor species, such as those used in zeolite or sol–gel syntheses, and typically (though not necessarily) the hydrophilic surfactant components. This leads to selective incorporation of the inorganic species into the hydrophilic regions, where they condense to form mesoscopically ordered inorganic–organic composite products. Such self-assembled structures form close to, or under certain conditions, at thermodynamic equilibrium, modified by kinetic processes, such as condensation of the inorganic species, solvent evaporation, etc. For a given mixture composition and temperature, various energetic contributions to the Gibbs free energy are balanced [125,126], with the result that a mesophase will self-assemble into a configuration that approaches an energetic minimum. Ordering length scales and periodicities of the mesophase are established by the dimensions and structures of the amphiphilic surfactant species, according to liquid crystal or block-copolymer self-assembly physics, modified by the influences of the inorganic species. Upon removal of the surfactant species, an ordered mesoporous inorganic solid can result, whose typically amorphous framework structure is a replica of the hydrophilic mesophase regions and whose pores and corresponding dimensions are vestiges of the hydrophobic components.

While there are a number of similarities in how zeolites and mesoporous solids are synthesized, there are also significant differences that distinguish how the onset and development of ordered domains occur in the two types of materials. Both involve complex solution chemistries in the presence of organic structure-directing agents, often at similar pHs and even identical inorganic species formulations, leading to ordered composite products. However, as distinguished previously in Fig. 1, formation of nano- and sub-nanoporous zeolites is inherently a crystallization phenomenon, involving the nucleation and growth of co-crystallized inorganic and organic species into solids with high extents of molecular organization, high degrees of long-range crystalline order, and characterized by rich and intricate structural topologies. By comparison, the formation of ordered mesoporous materials is governed by liquid crystal or block copolymer self-assembly processes in the presence of co-assembled inorganic species, which leads typically to materials with amorphous inorganic frameworks and often high extents of long-range mesoscopic ordering that are typical of relatively simple hexagonal, lamellar, cubic, or spherical mesophases. As in the zeolite studies discussed above, detailed insights into the formation mechanisms of mesoporous solids can be obtained by using NMR and EPR spectroscopy to identify key solution, solid, and interfacial species, establish interactions among them, quantify their relative populations, and correlate their roles in the self-assembly/nucleation and growth of long-range mesoscopic order.

3.1. Low-molecular-weight charged surfactants

In a number of aqueous inorganic–organic systems, ionic surfactant species act as structure-directing agents through electrostatic interactions with oppositely charged inorganic species across a hydrophobic–hydrophilic interface. For example, the discovery [1,127] that alkaline anionic silicate–cationic surfactant mixtures could be used to produce mesoporous solids with uniform tunable pore dimensions led to widespread efforts to control and expand such synthesis strategies to a large number of inorganic–surfactant materials. The physicochemical processes underlying these diverse syntheses are often complicated by the multicomponent, non-equilibrium, and heterogeneous nature of the mixtures, together with overlapping hydrolysis, self-assembly, and inorganic polymerization processes, often also under the influence of concentration and thermal gradients and/or applied shear, electromagnetic, or surface fields. Nevertheless, the molecular origins of the self-assembly, organization, and phase behavior of inorganic–surfactant mesophases can be established in detail by using a combination of complementary experimental techniques. Depending upon the composition of the synthesis mixtures and products, multinuclear NMR (including ^{1}H, ^{2}H, ^{13}C, ^{14}N, ^{17}O,^{27}Al, ^{29}Si, ^{31}P, and ^{81}Br) and EPR studies can be correlated with scattering, electron microscopy, adsorption, and/or other macroscopic property measurements to obtain compositional, structural, and dynamical information over molecular, mesoscopic, and macroscopic length scales.

3.1.1. Equilibrium mechanistic studies

The molecular bases by which inorganic–surfactant mesophases self-assemble under highly alkaline conditions is generally well understood, due principally to the molecular insights provided by NMR and EPR spectroscopy. Important to this understanding has been the ability to examine self-assembly and resulting phase behaviors of multicomponent lyotropic silicate–surfactant liquid crystals under conditions where thermodynamic equilibrium prevails. Until now, such conditions have been observed only for silica and only under highly alkaline conditions, where self-assembly can occur in the absence of inorganic cross-linking or gelation. For example, in highly alkaline aqueous solutions (pH ~ 12, 298 K), mixtures of cationic surfactants, such as cetyltrimethylammonium bromide

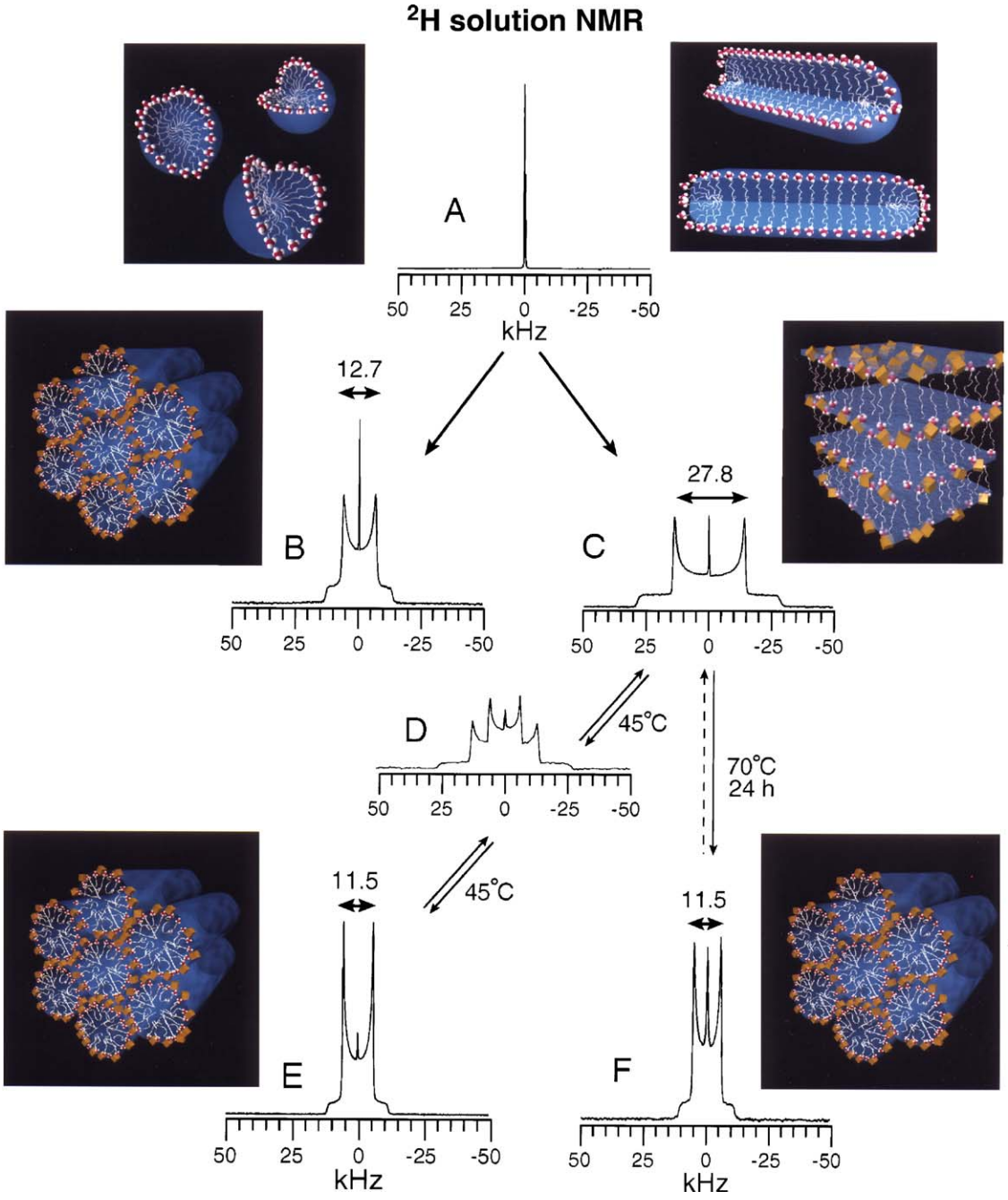

Fig. 11. ^{2}H NMR spectra of (A) a representative isotropic micellar CTAB(aq) solution; (B) a hexagonal silicate–CTA^{+} liquid crystal (C) a lamellar silicate–CTA^{+} liquid crystal (D) a two-phase mixture of hexagonal and lamellar silicate–CTA^{+} liquid crystals formed from (C) after heating for 10 min at 45 °C, which transforms reversibly into (E) a single hexagonal phase after 8h. (F) a hexagonal silicate–CTA^{+} liquid crystal formed irreversibly from the lamellar sample (C) after heating for 24 h at 70 °C. An isotropic micellar phase co-exists with the liquid crystal phases in (B)-(F). [Reprinted with permission from Ref. [128]. Copyright 1995 AAAS.]

(CTAB), and anionic silicate species form self-assembled mesophases that display lyotropic liquid crystalline behavior under conditions of thermodynamic equilibrium. Firouzi et al. [126,128] showed through a combination of correlated solution-state ^{2}H, ^{13}C, and ^{29}Si NMR spectroscopy, small-angle X-ray scattering, and polarized optical microscopy measurements that isotropic micellar solutions of CTAB transformed into hexagonal or lamellar phases when mixed with anionic silicate oligomers in highly alkaline solutions.

Deuterium (^{2}H) NMR measurements of deuterated surfactant species (for example, labeled at the α-carbon position as C–^{2}H bonds) have been widely used to study lyotropic liquid crystal phase behavior, aggregate geometry (e.g., cylinders or sheets), local order parameters, and molecular motions [129]. In alkaline silicate–surfactant liquid crystals specifically, such information has provided insights on the molecular dynamics and organization of the surfactant species, which were correlated with small-angle X-ray scattering (SAXS) results to

elucidate their phase behaviors in detail [126]. A requirement for such studies is that translational molecular mobilities of the surfactant species must be fast on the ^{2}H NMR time scale (10^{-5}–10^{-4} s), although in liquid crystal phases the molecules are generally confined within the anisotropic geometries of the individual aggregates. As a consequence, time-averaged values for the quadrupolar interaction are non-zero, leading to residual quadrupolar splittings in the ^{2}H spectra that yield information on aggregate shapes and phases.

Fig. 11 shows ^{2}H NMR spectra obtained for silicate–surfactant liquid crystal mesophases prepared with CTAB deuterated at the α-carbon position under conditions of thermodynamic equilibrium at different temperatures and mixture compositions [128]. The initially isotropic low-concentration (7 wt.%) micellar CTAB (aq) solution yields a narrow ^{2}H NMR signal Fig. 11,A in the absence of silicate species, consistent with rapid isotropic mobility of the surfactant molecules. Upon the addition of an alkaline solution containing anionic silicate oligomers, hexagonal Fig. 11,B or lamellar Fig. 11,C liquid crystal phases rapidly form, as evidenced by the characteristic splittings of the scaled ^{2}H "Pake-powder patterns," 13 kHz or 28 kHz, respectively, according to the different mixture compositions. The ^{2}H NMR splittings reflect signals from rapidly mobile surfactant molecules that are partially averaged to different extents by motions that are constrained within the cylindrical or sheet-like aggregates of the hexagonal and lamellar phases. Reversible first-order phase transformations can be induced between ordered hexagonal and lamellar liquid crystal phases by changing the temperature, as evidenced by the superposition of the corresponding ^{2}H lineshapes (Fig. 11C,D,E), provided extensive silica cross-linking has not occurred. After reduction of the pH to below ca. 11.5 or prolonged treatment at elevated temperatures (~70 °C) to promote silica condensation, no further phase changes can occur, due to the rigidity of the solidified silica framework. ^{14}N NMR measurements (spin $I=1$, 100% nat. abund.) have also been used to characterize the solution-state environments of the cationic quaternary ammonium head group moieties [130] of the CTAB surfactant species during syntheses of mesoscopically ordered silica. These studies required no isotopic enrichment, although the information obtained is often limited by characteristically large first-order quadrupolar interactions associated with ^{14}N.

The roles of various counter-ions and solvent species in the nucleation and growth of self-assembled inorganic–surfactant mesophase domains can be established by using solution-state NMR. Such investigations allow the molecular identities of intermediates, precursors, exchangeable ions, and/or co-solvent species to be determined, as well as their partitioning between different regions or phases. These studies generally require that components of interest remain isotropically mobile and long-lived, relative to the ca. 10^{-6}-s time scale typical of most 1D NMR measurements. As similarly discussed above for precursor solutions in zeolite syntheses (see Fig. 2) [22,25,35,36], both the identities and relative populations of silicate species in silicate–CTA$^+$ multicomponent mixtures can be quantitatively established by using in situ solution-

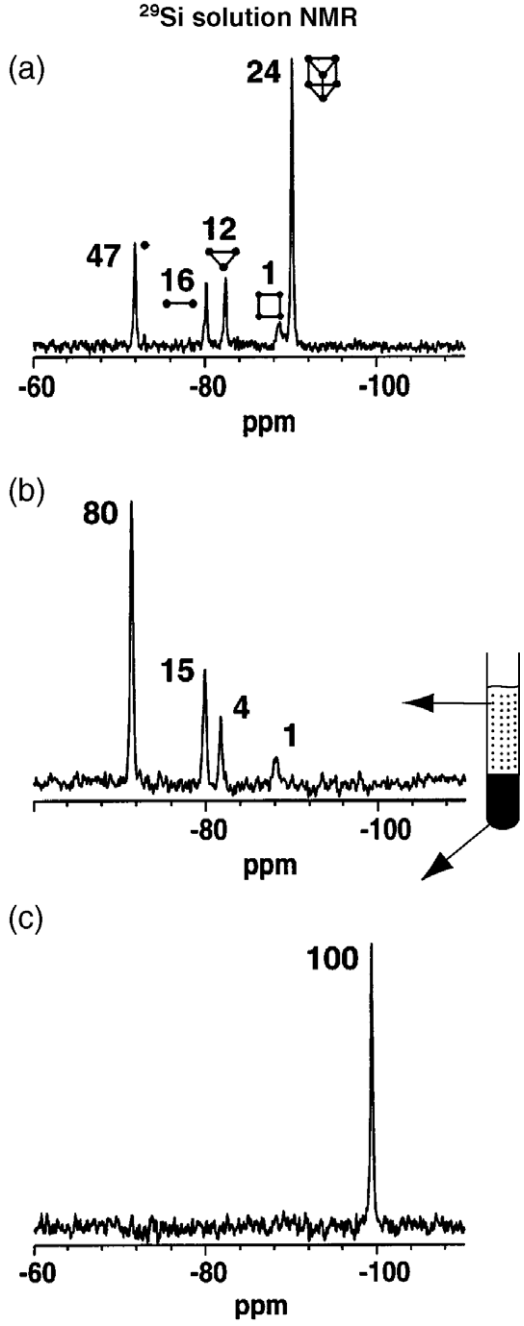

Fig. 12. Room-temperature solution-state ^{29}Si NMR spectra of (a) a tetraethylammonium silicate precursor solution (pH 13.0) containing principally Si atoms in double-three-ring silicate anions, (b) the aqueous-rich phase, and (c) the silicate–surfactant-rich phase that exist in equilibrium in the two-phase mixture formed after mixing the inorganic precursor solution in (a) with a 6.8 wt. % CTAB-(aq) solution. Relative mole percents of the various silicate anion species in each spectrum are shown. [Adapted with permission from Ref. [126]. Copyright 1997 American Chemical Society.]

state ^{29}Si NMR. For example, the solution-state ^{29}Si NMR spectrum in Fig. 12(a) shows peaks corresponding to the different oligomeric silicate anions that exist in (or near) equilibrium in a typical inorganic precursor solution used to prepare silicate–surfactant liquid crystals. From the normalized integrated ^{29}Si peaks, this silicate precursor solution contained an equilibrium mixture of 47% monomers ($SiO_4H_n^{(4-n)-}$ at

−72.4 ppm), 16% dimers ($Si_2O_7H_n^{(6-n)-}$ at −81.0 ppm), 12% cyclic trimers ($Si_3O_9H_n^{(6-n)-}$ at −82.7 ppm), 1% cyclic tetramers ($Si_4O_{12}H_n^{(8-n)-}$ at −88.2 ppm), and 24% double-three-ring (D3R) species ($Si_6O_{15}H_n^{(6-n)-}$ at −90.0 ppm), in molar percentages. The addition of this homogeneous precursor solution to an isotropic 7 wt.% micellar CTAB solution rapidly (ca. seconds) formed a two-phase mixture (pH 12), comprised of an aqueous-rich isotropic phase with a silicate–surfactant-rich hexagonal (H_α) phase. These conditions and the resulting self-assembly process are identical to and consistent with those monitored by ^{2}H NMR spectra [Fig. 11(A) and (B)] of the deuterated surfactant species.

But whereas ^{2}H NMR lineshapes are used to monitor the geometries of surfactant aggregates in different liquid crystal mesophases, solution-state ^{29}Si NMR permits the rich speciation of silicate anion distributions in these mixtures to be analyzed in detail. For example, the ^{29}Si NMR spectra in Fig. 12 (b) and (c) prove that the various silicate oligomeric anions are partitioned differently among the two equilibrium phases present at room temperature: the aqueous-rich phase contains large concentrations of monomers (80%), as well as dimers (15%), cyclic trimers (4%), and cyclic tetramers (1%) [Fig. 12 (b)], while the silicate–surfactant-rich phase possesses exclusively double-four-ring (D4R) anions (100%) [Fig. 12(c)]. The highly charged oligomeric silicate anions in alkaline inorganic precursor solutions interact strongly with the cationic surfactant head groups, thereby effectively shielding electrostatic repulsions between micelles and promoting rapid self-assembly of silicate–surfactant mesophases. The bulky double-ring silicate anions apparently retain negative charges that are not completely neutralized at the surfactant aggregate interfaces, and so remain unpolymerized, allowing under the specific conditions used, formation of thermodynamically stable liquid crystal phases.

Solution-state ^{81}Br NMR measurements confirm essentially complete exchange of Br^-, the initial counter-ions present in the CTAB surfactant species, in favor of the double-ring silicate anions during alkaline syntheses of mesoscopically ordered silica [126]. The ^{81}Br (or ^{79}Br, both spin I=3/2, 50% nat. abund.) NMR studies also require no isotopic enrichment. As discussed above, after initial mixing rapid halide–silicate anion exchange occurs at the micelle interfaces, thereby reducing inter-aggregate repulsions, so that attractive van der Waals forces become dominant, and liquid crystal phases self-assemble. Such observations are analogous to electrolyte "salting out" effects in micellar solutions, in which the addition of dissolved salts diminishes the Debye–Hückel ionic double layer that accounts for repulsions between dilute micelles, with the result that attractive interactions prevail and lyotropic liquid crystal phases spontaneously form [131]. For a given mixture composition and temperature, various contributions to the Gibbs free energy must be balanced, with the result that, under conditions of thermodynamic equilibrium, a mesophase will self-assemble into the configuration with the lowest overall energy.

Perhaps surprisingly, although the precursor silicate solution in Fig. 12(a) contained no double-four-ring (D4R) silicate anions, the equilibrated hexagonal liquid crystal phase [Fig. 12(c)] was comprised exclusively of D4R silicate species. This manifests the strong *molecular* structure-directing function of the cationic surfactant head groups (in addition to the usual mesoscale organization), which stabilize certain oligomeric silicate anions at the hydrophilic–hydrophobic aggregate interfaces. For the case of tri*methyl*ammonium head group moieties (e.g., of CTA^+), double-four-ring anions are preferred, whereas for tri*ethyl*ammonium head groups double-three-ring anions predominate [126]. Such interfacial silicate-ion selections appear to be due to the differing extents to which electrostatic and hydrophobic interactions are balanced between the alkylammonium head group moieties of the surfactant and multi-charged double-ring silicate oligomers. Other strongly interacting (e.g., charged) surfactant head groups may be expected to interact preferentially with these or other oppositely charged inorganic species under favorable solution conditions.

The importance of the equilibrium silicate–surfactant liquid crystal investigations lies in the fact that the inorganic–organic self-assembly process was entirely decoupled from the kinetics

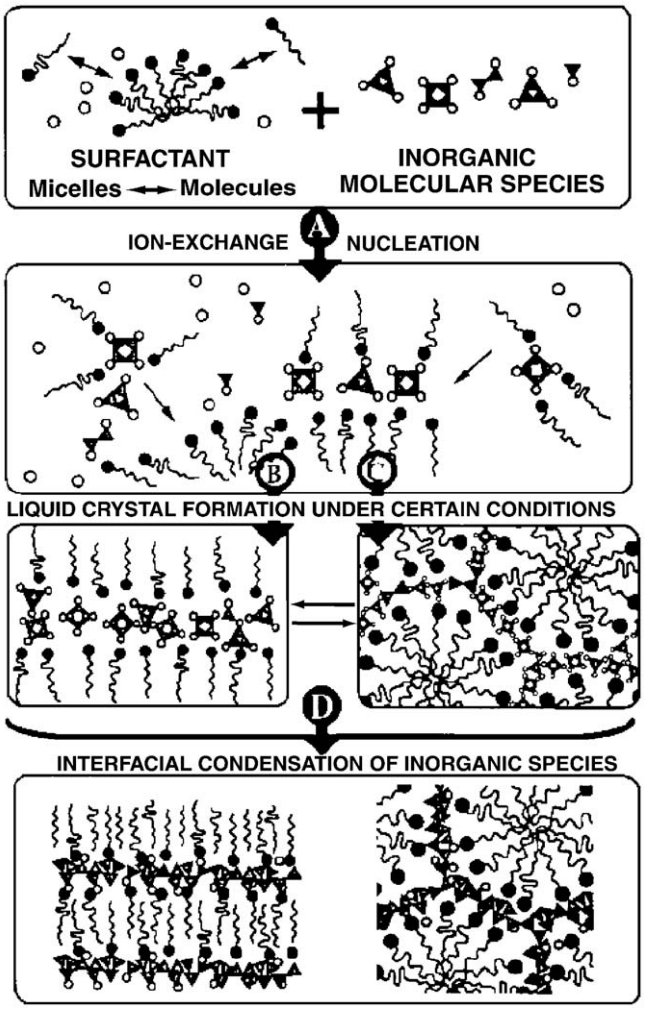

Fig. 13. Schematic overview of the principal physicochemical processes that occur during silicate–surfactant co-self-assembly. [Adapted with permission from Ref. [133]. Copyright 1994 American Chemical Society.]

of precursor hydrolysis, solvent evaporation, or interfacial silicate polymerization. As a consequence, the molecular and mesoscopic mechanistic details associated with inorganic–organic mesophase nucleation and growth, as well as overall phase behavior could be determined and correlated. The presence of polymerizable silicate anions at the interfacial region of a silicate–surfactant mesophase introduces opportunities for further manipulation of the phase structure through condensation of the silicate species, which may be achieved by lowering the pH (<11.8) and/or prolonged thermal treatments [126]. In such cases, as silica polymerization progresses, the charge density of the inorganic framework is reduced, thereby altering the interfacial force balance. As a consequence of these non-equilibrium changes, the system may respond by adopting a new mesophase morphology, providing the flexibility of the cross-linking silicate network allows it [128,132]. Despite the presence of well-defined silicate anions in the liquid crystal phases, all vestiges of local, e.g., double-four-ring, order, however, are lost during the initial cross-linking procedure, reflecting the dynamic lability of Si–O–Si bonds in alkaline solutions. The mesostructured silica frameworks that result are amorphous with characteristics that are identical to those of other M41S-type materials [1]. Fig. 13 summarizes the principal physicochemical processes that occur during silicate–surfactant

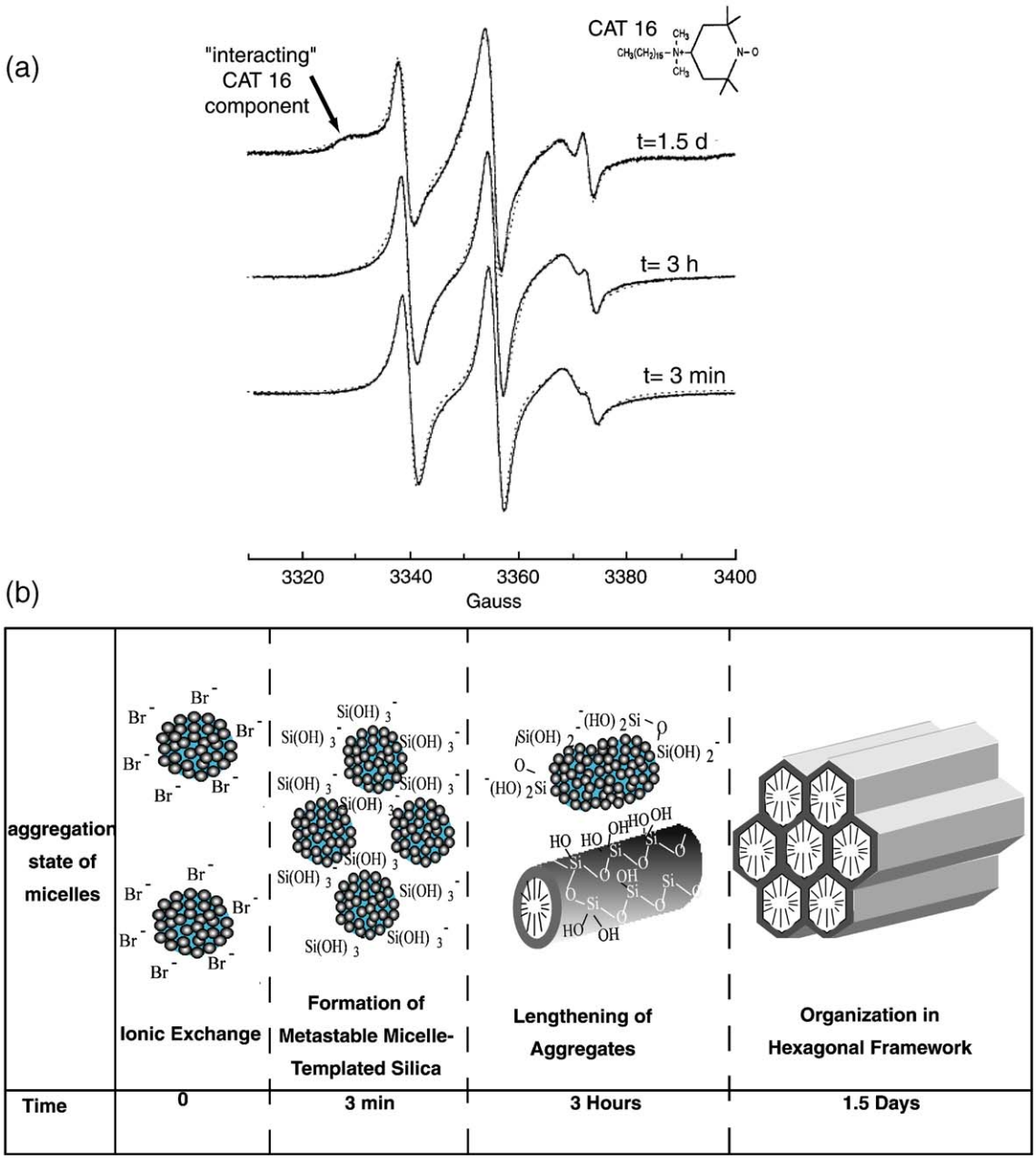

Fig. 14. (a) Experimental (full lines, 323 K) and computed (dotted lines) EPR spectra of 0.05 M CTAB solution containing 2.5×10^{-4} M 4-cetyldimethylammonium-2,2,6,6-tetramethyl-piperidine-1-oxyl (CAT16), 0.5 M silica and 0.14 M NaOH at various times (t = 3 min; 3 h; 1.5 days) after addition of the silica solution to the CTAB solution. (b) Schematic view of the formation of mesostructured silica at 323 K. [Adapted from [134]. Copyright 1998, Reprinted with Permission.]

self-assembly, including convective mixing of the components, silicate–halide ion-exchange, formation of ordered mesophase domains (with liquid crystalline properties under certain conditions), and typically condensation/cross-linking of the surfactant-ordered inorganic species [133].

3.1.2. Non-equilibrium mechanistic studies

For different synthesis compositions (e.g., pH, inorganic oxide precursors, solvents, co-solvents, and surfactants) or processing conditions (e.g., temperature, pressure, or flow), the same underlying physicochemical processes are expected to occur as for the silicate–CTA^+ liquid crystals, although their relative contributions will generally be different and the systems may be far from equilibrium. Taking into account such differences, the general physical insights can nevertheless serve to guide other complex inorganic–organic mesophase syntheses, including those using cationic inorganic precursor species, anionic, non-ionic, or block-copolymer surfactants, hydrogen-bonding components, etc. A main prerequisite is that the inorganic species interact sufficiently strongly with the surfactant species to allow co-assembly of a composite system. As is widely known, however, equilibrium conditions leading to thermodynamically stable liquid crystal systems are neither necessary nor common. In general, synthesis and processing conditions may be used in which surfactant self-assembly and inorganic cross-linking occur simultaneously, as indeed is typically the case. For alkaline silicate solutions with pH values <11.8, and acidic or neutral sol–gel mixtures of silicates, other oxides, non-oxides, and/or mixtures thereof, mesostructured inorganic solids can be prepared, though under conditions where mesophase ordering develops and evolves according to multiple kinetic processes. Such systems self-assemble according to instantaneous thermodynamic criteria that will be similar to those described above for the special case of highly alkaline silicate–CTA^+ liquid crystals in equilibrium.

Concurrent kinetic processes, such as hydrolysis of inorganic precursor species, solvent/co-solvent evaporation, inorganic cross-linking, domain nucleation and growth, etc., however, can introduce multiple time-dependent factors that make the processes difficult to disentangle and control. Galarneau et al. have notably followed the dynamic development and evolution of order in silica–CTA^+ materials by using electron paramagnetic resonance (EPR) spectroscopy [134]. EPR measurements are sensitive to the environments of free-radical probe species added in low concentration to the synthesis mixture, which allow different aggregation states of the self-assembling silica–surfactant components to be identified. For example, as shown in Fig. 14(a), EPR spectra were acquired 3 min, 3 h, and 1.5 days after mixing an alkaline silicate precursor solution with a micellar solution of CTAB, containing 0.005 molar surfactant ratio of nitroxide-containing surfactant species, such as the cationic probe agent depicted in the inset. Compared to EPR spectra of an otherwise identical dilute micellar CTAB solution before the addition of silica, significant differences are observed in EPR spectra acquired at later times. EPR lineshape changes can be attributed to different, predominantly diminishing, probe

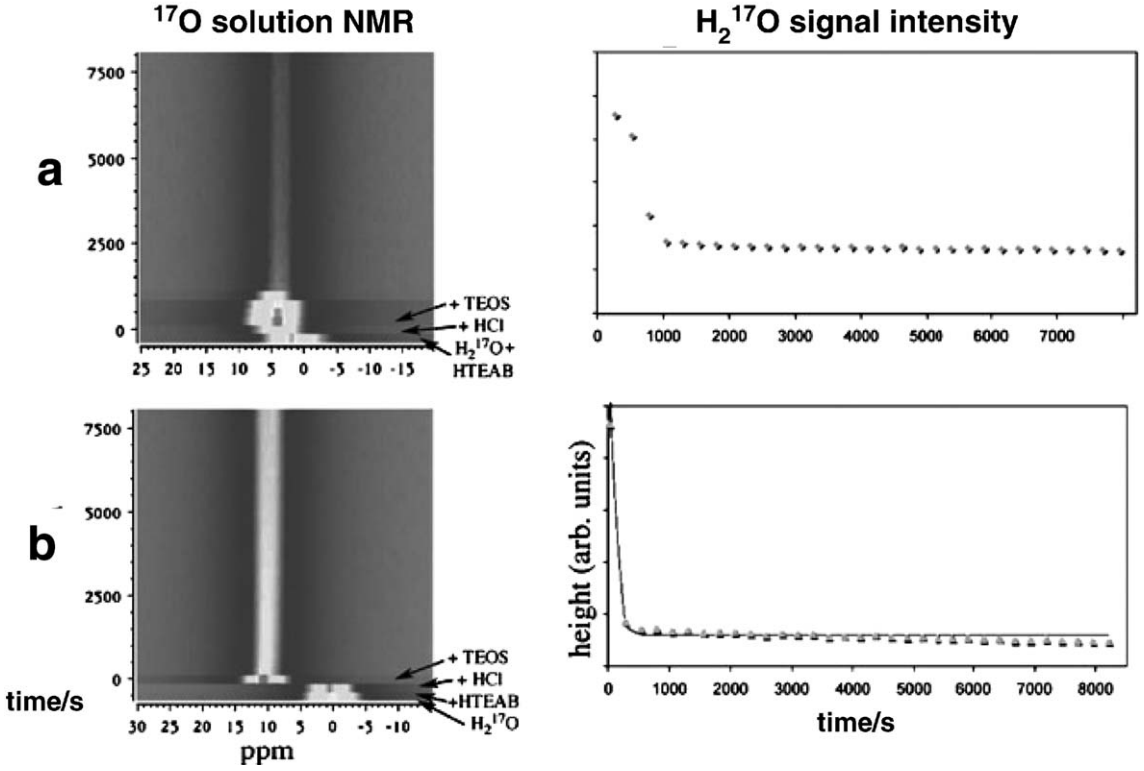

Fig. 15. Time-resolved in situ ^{17}O NMR spectra measured at (a) pH = 0 and (b) pH = −0.7 showing the evolution in time of the water signal. A spectrum of 50 mL of $H_2^{17}O$ is inserted at the beginning of the series of 2D data (line width is typically 170 Hz), as well as the spectra of $H_2^{17}O$ + HCl and $H_2^{17}O$ + HTEAB for comparison after the addition of TEOS. [Adapted from Ref. [135]—reproduced by permission of the PCCP Owner Societies.]

mobilities that reflect changing interactions of the probe species in self-assembled surfactant aggregates and at the interface with the polymerizing silica network. At longer reaction times (1.5 days), a feature is observed at ca. 3330 Gauss that is assigned to an approximately 35% fraction of the probe species that interacts 'strongly' with the condensed silica framework. When correlated with X-ray diffraction results, the EPR analyses permit silica–surfactant aggregation kinetics to be examined as a function of different compositions and process variables. Fig. 14(b) summarizes the time-dependent aggregation behavior of CTA^+-templated silica based on EPR results, showing schematically dilute micelles, liquid-crystal-like aggregates, and the extending silica network.

In contrast to the study of mesophase self-assembly from highly alkaline conditions, there are only few studies of the dynamic processes leading to the formation and growth of mesoporous materials under acidic conditions. Egger et al. [135] used in situ solution-state ^{17}O, ^{14}N and solid-state ^{29}Si MAS NMR along with energy dispersive X-ray diffraction (EDXRD) to follow the formation of mesoporous SBA-1 at low pH. The intensity of the ^{17}O NMR signal corresponding to water can be used as a probe of the hydrolysis and polymerization kinetics of TEOS. Its acid catalyzed hydrolysis leads to the incorporation of ^{17}O nuclei from ^{17}O-enriched water and therefore to a decrease in the intensity of the water ^{17}O NMR signal. Fig. 15(a) shows a series of solution-state ^{17}O NMR spectra for different times after the addition of TEOS to an hexadecyltriethylammonium bromide (HTEAB) surfactant solution at pH = 0 and a corresponding plot of the intensity of the ^{17}O water peak at 2 ppm. Fig. 15(b) shows the identical measurements for a surfactant solution at pH = −0.7, where the water signal is shifted to 10 ppm. The more rapid decrease of the water ^{17}O signal at lower pH supports an acid catalyzed mechanism for the TEOS hydrolysis. In both cases, the decay of the signal does not obey a simple exponential dependence, which points to the involvement of at least two different processes. A comparison of the maximum loss in $H_2^{17}O$ due to hydrolysis with the total loss of ^{17}O water signal suggested that the signal decrease was partially due to strong association of water species to the polymerizing silica species. Additional ^{17}O NMR measurements of hydrolysis in the absence of surfactant molecules furthermore showed that the hydrolysis of TEOS occurred about three times as fast in the presence of HTEAB independent of the solution pH over the range examined.

In solution-state in situ ^{14}N NMR measurements, a decrease in the signal arising from the surfactant head groups occurred significantly after the observed decrease in the $H_2^{17}O$ signal. Nevertheless, on the same timescale, the appearance and growth of an ordered mesophase precipitate is observed by EDXRD [135]. Consequently, the decrease in the intensity of the solution-state ^{14}N NMR signal was attributed to reduced surfactant head group motions in the silica–surfactant aggregates. Low intensity signals arising from Q^4 species in ^{29}Si MAS spectra at room temperature suggests that the cross-linking of silica species at very low pH is poor despite increased hydrolysis. Overall, the extensive study by Egger et al. [135] suggests fast hydrolysis of silica species and binding of water to small oligomers, followed by slower aggregation to a mesophase, similar to what is observed in the formation of liquid crystals under equilibrium conditions. Reorganization of the precipitate subsequently leads to the formation of an ordered SBA-1 structure. Insights gained from in situ NMR and EPR measurements under equilibrium or slowly evolving conditions, allow molecular and mechanistic details to be determined from which more complicated conditions and mixtures may be better understood and optimized.

3.2. Co-condensation of mixed inorganic framework components

As the varieties of compositions and synthesis conditions of mesostructured inorganic solids have expanded, much progress has been achieved in the preparation of inorganic frameworks with mixed compositions. In such cases, the nucleation and growth of surfactant-templated mixed oxide (or other inorganic) solids are still more complicated, as they present greater compositional diversity and the possibility of usually undesirable macrophase separation of the different inorganic components. A key issue in syntheses and characterization of all such mesostructured systems with mixed inorganic framework compositions is the extent to which uniform co-assembly and co-condensation occur. Different precursor solubilities and different hydrolysis and condensation kinetics open questions as to whether ordered domains nucleate and grow with uniform compositions and structures, or whether and to what extent heterogeneities exist.

An important example is the incorporation of aluminum heteroatoms into mesostructured silica frameworks, which as for zeolites, can have beneficial effects on the adsorption and chemical reaction properties of the product materials. To optimize the properties of aluminosilica mesoporous solids, it is necessary to establish the extent to which Al atoms have been incorporated into the inorganic framework and their oxidic coordination. Typically, solid-state 1D ^{27}Al MAS NMR (spin $I = 5/2$, 100% nat. abund.) has been used to quantify the relative amounts of tetrahedrally and octahedrally coordinated aluminum atoms, based on their characteristic ^{27}Al MAS peak positions near 55 ppm and 0 ppm, respectively. Tetrahedral coordination is generally considered to indicate desirable framework Al species, while octahedral coordination may reflect undesirable dense Al_2O_3 species or framework Al moieties coordinated also to strongly adsorbed water. While 1D MAS methods are often ambiguous with respect to such determinations, the powerful correlative capabilities of two-dimensional (2D) NMR methods can yield detailed structural and compositional insights on molecular proximities that resolve these questions definitively.

Fig. 16 shows a pulse sequence and spectra for 2D $^{27}Al\{^1H\}$ HETeronuclear chemical shift CORrelation measurements that allow dipole–dipole-coupled proton and aluminum moieties to be established [137]. In this experiment [136], ^1H spins are excited by a 90° pulse, followed by an incremented evolution period t_1 that encodes the proton frequencies. The inclusion of an optional mixing time, preceded by a second 90° pulse which

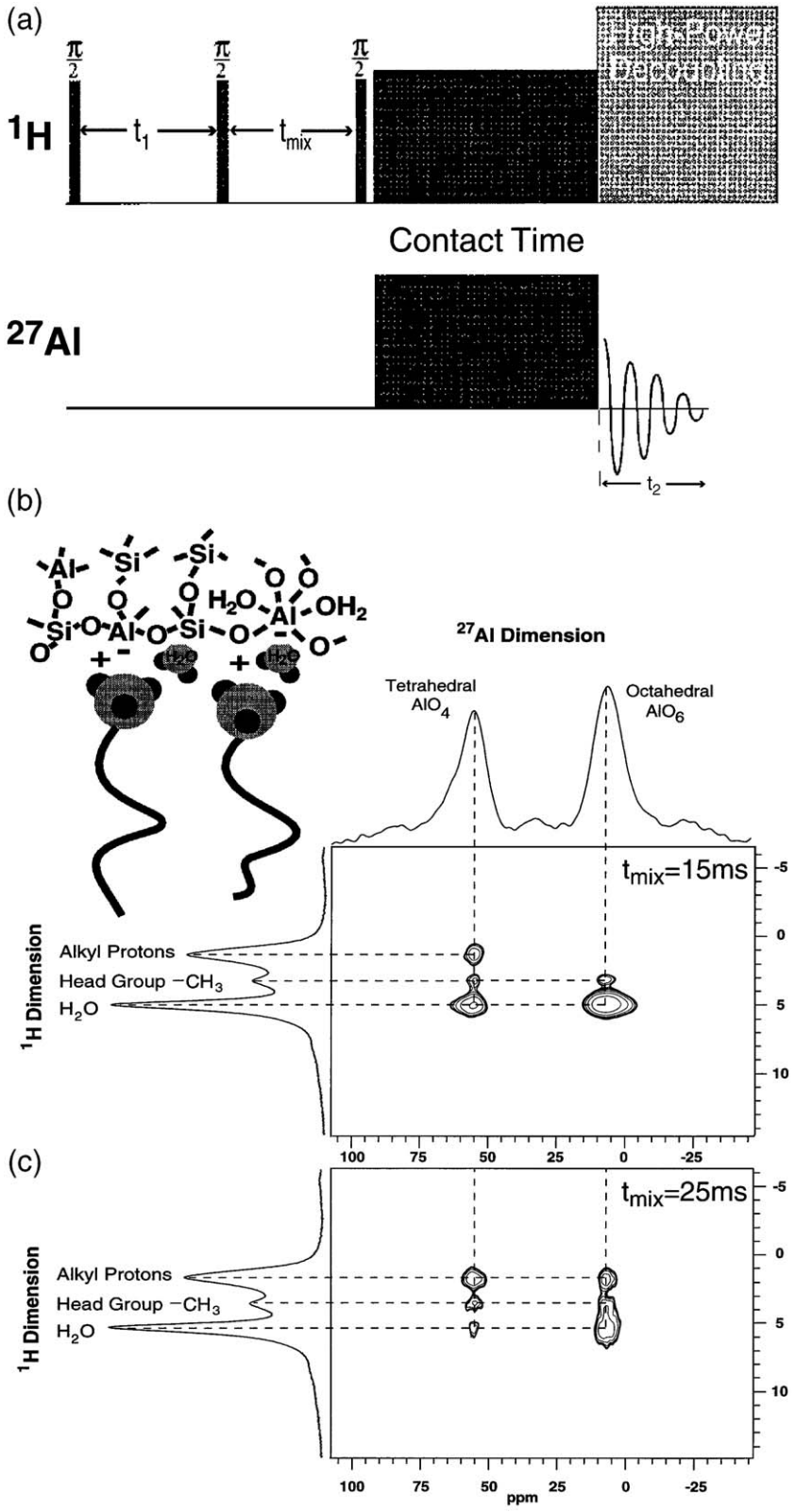

Fig. 16. (a) $^{27}Al\{^{1}H\}$ HETCOR NMR pulse sequence that allows for ^{1}H spin diffusion to occur during the mixing time t_{mix} for measurement of framework interactions with the surfactant species and adsorbed water. (b)–(c) 2D $^{27}Al\{^{1}H\}$ HETCOR spectra for hexagonal aluminosilica MCM-41 acquired using the pulse sequence depicted in (a). The spectra were recorded with a mixing time of (b) 15 ms and (c) 25 ms. [Adapted with permission from Ref. [137]. Copyright 1998 American Chemical Society.]

stores the ^{1}H magnetization along the z-axis, allows proton spin diffusion to transfer magnetization among nearby proton moieties, permitting the measurement of even relatively weakly coupled ^{1}H–^{27}Al spin pairs. A third 90° pulse initiates the contact time, during which ^{1}H magnetization is transferred to nearby ^{27}Al spins for subsequent detection during t_2 under conditions of proton decoupling. Importantly, the ^{27}Al species are never excited directly, but rather receive magnetization only from proton spins to which they are molecularly near and dipole–dipole coupled. By performing a double Fourier transform of the time domain ^{1}H signals in t_1 and ^{27}Al signals in t_2, a two-dimensional frequency map is produced that contains correlated ^{27}Al–^{1}H signal intensities from dipole–dipole-coupled spin pairs that are resolved according to their respective chemical shifts. On the basis of such correlations, the proton species from which the ^{27}Al sites received their magnetization can be unambiguously established.

For example, Fig. 16(b,c) shows 2D $^{27}Al\{^{1}H\}$ HETCOR contour-plot spectra acquired for as-synthesized hexagonal aluminosilica MCM-41 prepared under hydrothermal conditions from a reaction gel containing a Si/Al ratio of six [137]. A separately acquired ^{27}Al CP/MAS spectrum is shown along the horizontal axis, revealing resolved ^{27}Al signals from four- and six-coordinated Al species at 56 and 6 ppm, respectively. A single-pulse ^{1}H MAS spectrum is shown along the vertical axis, yielding resolved ^{1}H signals from adsorbed water (4.7 ppm), the trimethylammonium surfactant head groups (3.2 ppm), and alkyl surfactant chains (1.0 ppm). For a mixing time of 15 ms [Fig. 16(b)], strong intensity correlations are observed between all of the different proton species and the four-coordinated aluminum moieties, consistent with the strong electrostatic interactions expected between the anionic tetrahedral framework Al sites and cationic surfactant head groups. The ionic character of these species furthermore render them hydrophilic and therefore strongly interacting with adsorbed water, as confirmed by the separate strong intensity correlation observed between Al^{IV} and H_2O, as well. Even stronger intensity correlations are observed between the six-coordinated ^{27}Al species and adsorbed water, along with a weaker correlation with the surfactant head group proton moieties. For longer mixing times (e.g., $t_{mix}=25$ ms), relatively weakly coupled ^{1}H–^{27}Al species become more visible, as shown in Fig. 16(c), where correlations also appear with the alkyl surfactant protons. These measurements establish that the six-coordinated Al^{VI} sites in this material are also in the framework and not present as dense macroscopically phase-separated Al_2O_3. Analogous and complementary $^{29}Si\{^{1}H\}$ HETCOR measurements for the same sample show similar strong interactions between framework silica sites and the structure-directing surfactant species [137]. These powerful 2D HETCOR techniques confirm unambiguously that silica and alumina precursor species co-assemble and co-condense during the nucleation and growth of surfactant-templated mesostructured aluminosilica under alkaline conditions. Such detailed NMR characterization insights have been used to optimize synthesis conditions to prepare mesostructured aluminosilica frameworks with near maximum Al contents approaching Lowenstein's limit of Si/Al=1 [138].

3.3. Formation of mesostructured silica using non-ionic block copolymers

In general, a variety of different surfactant, block-copolymer, or colloidal agents may be suitable for directing the formation of condensed inorganic network structures. The principal requirements are that conditions must exist in which the structure-directing agents self-assemble into ordered systems, and under which the inorganic species interact with or otherwise associate selectively with certain of the self-assembling components. One system that has been extensively studied mechanistically has used amphiphilic poly(ethylene oxide)–poly(propylene oxide)–poly(ethylene oxide) (PEO–PPO–PEO) block copolymer species under acidic solution conditions to incorporate and cross-link hydrolyzed silica precursor species selectively in the hydrophilic regions of hexagonal and cubic composite mesophases [139–145], While the underlying physical basis by which self-assembly occurs is similar for non-ionic block-copolymer species and the charged-surfactant structure-directing agents discussed above, several mechanistic differences can be identified. Among them, is that the two systems often occur in different regimes where attractive versus repulsive interactions dominate among the self-assembling agents. For example, syntheses involving relatively low bulk concentrations of low-molecular-weight surfactant species in either alkaline or acidic solutions occur under conditions where attractive van der Waals interactions cause self-assembly. This accounts for the two phases observed in the silicate–surfactant liquid crystal system discussed in Figs. 11 and 12 above. In contrast, syntheses that rely on non-ionic PEO–PPO–PEO block copolymers frequently employ conditions where repulsive interactions dominate due to entropic effects, so that concentrated single-phase composites result.

Mesostructured silica formed using PEO–PPO–PEO block copolymers in highly acidic solutions self-assembles as cationic silica species interact via polar interactions (e.g., hydrogen bonds) with the hydrophilic PEO moieties. Because silica condensation typically occurs simultaneously with self-assembly, such materials form under non-equilibrium conditions that are similar to those discussed above for the CTA^{+}-silica system under moderately alkaline conditions [Fig. 14]. Similar to studies reported by Galarneau et al. [134] for the CTA^{+}-silica system, the evolution of order in the block copolymer-silica system can be followed by EPR measurements. Ruthstein et al. [141,142] have studied the formation of SBA-15 by in situ EPR and electron spin-echo envelope modulation (ESEEM) experiments that are sensitive to changes in polarity near the free-radical probe species. The EPR results suggest that a flexible silica network with high water and PEO contents is formed during the first 2 h of the reaction at 50 °C along with the establishment of hexagonal order [141], in three approximate stages [142]. In the first 5 min after the addition of acid and TetraMethylOrthoSilicate (TMOS) to the polymer solution, hydrophobic TMOS and partly hydrolyzed TMOS penetrate into the PPO core of the block copolymer aggregates. This is accompanied by fast hydrolysis of TMOS, which leads to the diffusion of hydrolyzed TMOS to the aggregate corona. In the

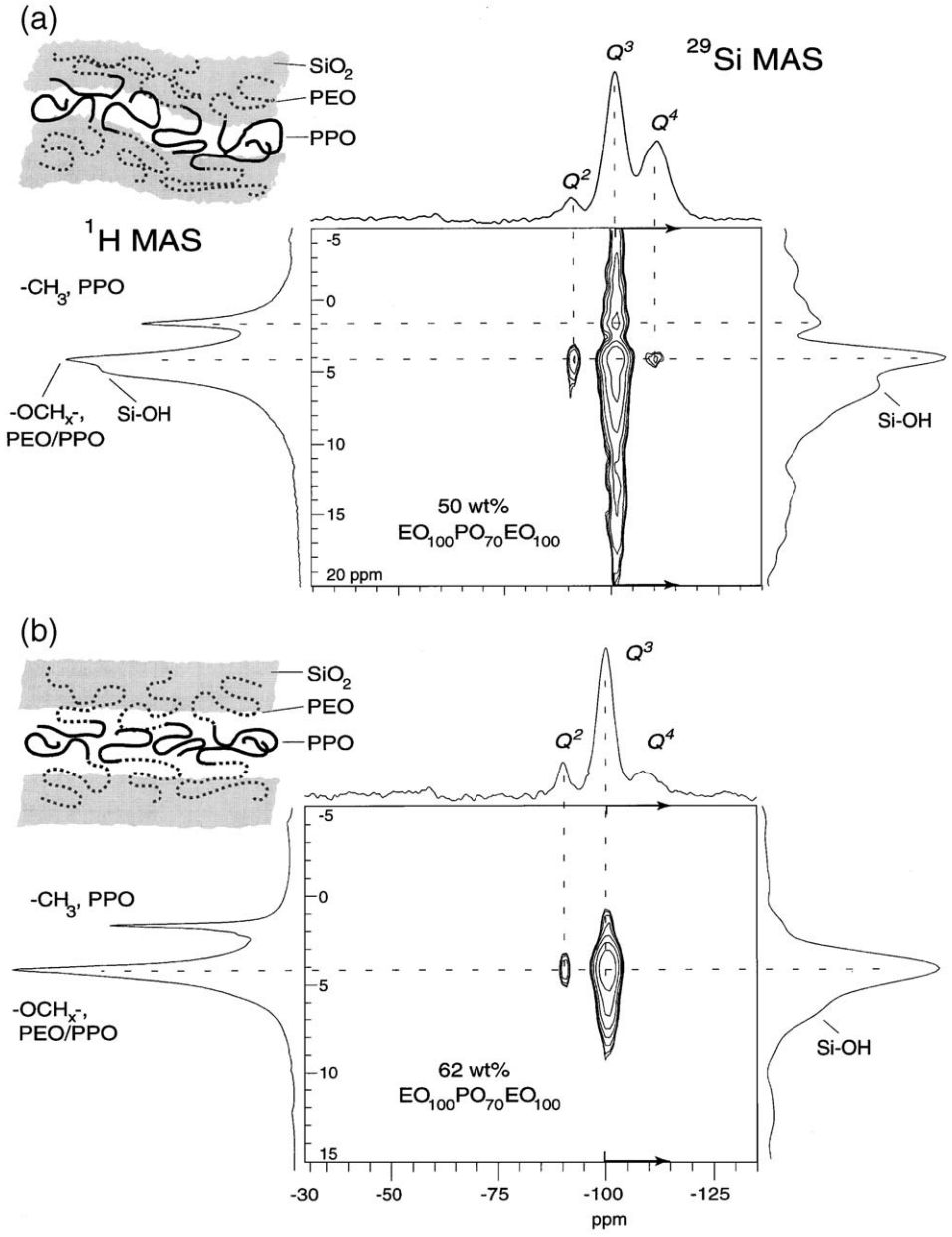

Fig. 17. 2D $^{29}Si\{^{1}H\}$ HETCOR NMR spectra (a) 50 wt.% and (b) 62 wt.% EO_{100}–PO_{70}–EO_{100}/SiO_2 composites. Separate ^{29}Si MAS and ^{1}H MAS spectra are plotted along their respective axes. 1D slices through the Q^3 plane have been plotted on the right side of the spectra to demonstrate correlated intensities more clearly. Schematic diagrams accompanying the spectra depict the local and mesoscopic structures of the composites consistent with the NMR, XRD, and TEM data. [Reprinted with permission from Ref. [139]. Copyright 1999 American Chemical Society.]

second stage, which lasts approximately 1 h, silica polymerization occurs at the core/corona interface of the polymer aggregates and then extends progressively outward to the corona region in the third stage (~1 h). In situ solution-state ^{1}H NMR measurements during the formation of SBA-15 suggest that block copolymer micelles initially increase in size after which they aggregate and subsequently precipitate [143], coalescing into cylinders that adopt, from in situ SAXS measurements, two-dimensional hexagonal order [144]. The stages of silica polymerization at the corona/core interface and in the corona as indicated by EPR appear to play a role in the increased sizes of the polymer aggregates and their aggregation. As the solidification of the silica framework progresses and nears completion, the resolution of features in 1D EPR (and also ^{1}H NMR) spectra tend to diminish, making it more difficult to extract molecular-level information on the resultant mesostructured composites.

Nevertheless, for the resultant silica-block copolymer products, a combination of powerful multidimensional solid-state NMR techniques, in conjunction with SAXS and TEM analyses, allows the structures and dynamics of the different components to be established and, furthermore, correlated across molecular, mesoscopic, and macroscopic length scales. While information on mesoscale material structures are available from SAXS and TEM, 2D solid-state NMR methods and NMR relaxation analyses yield insights on the molecular

interactions that underlie the corresponding self-assembled structures. For example, local separation of the PEO and PPO copolymer blocks and their interfacial proximities relative to the silica matrix can be determined from 2D $^{29}Si\{^{1}H\}$ HETCOR experiments. Correlated peak intensities between ^{1}H and ^{29}Si resonances in a 2D $^{29}Si\{^{1}H\}$ HETCOR spectrum, such as shown in Fig. 17, indicate close spatial proximities of dipole–dipole coupled ^{1}H and ^{29}Si species. The peaks at ca. −90 ppm, −100 ppm, and −110 ppm in the 1D ^{29}Si MAS spectra shown along the horizontal axes of Fig. 17 are assigned to Q^2, Q^3 and Q^4 ^{29}Si species, corresponding to sites with increasing extents of cross-linking. The ^{1}H MAS spectra along the vertical axes in Fig. 17 are associated with proton moieties of the EO_{100}–PO_{70}–EO_{100} block copolymer and silanol groups, as indicated.

$^{29}Si\{^{1}H\}$ HETCOR spectra of different EO_{100}–PO_{70}–EO_{100}/silica composites provide molecular-level evidence for increasing separation of the PEO and PPO segments with increasing block copolymer concentrations [139]. For a 50 wt.% block copolymer/silica composite, the 2D $^{29}Si\{^{1}H\}$ HETCOR spectrum in Fig. 17(a) yields correlated signal intensities between protons associated with both the PEO and PPO moieties and ^{29}Si framework species. Resolved peaks are observed that reflect strong intensity correlations between the Q^3 ^{29}Si species (−102 ppm) and protons associated with both –OCH_2– moieties (4.0 ppm), which are attributed to both PEO and PPO segments, and the PPO methyl groups (1.5 ppm.) A 1D ^{1}H MAS slice through the Q^3 ^{29}Si peak is plotted on the right vertical axis of Fig. 17(a), showing these resolved proton correlations, as indicated by the dotted lines. Weaker correlations are also observed between Q^2 and Q^4 ^{29}Si species and the PEO and PPO moieties. The existence of correlations involving protons from both the PEO and PPO blocks and ^{29}Si species in the silica network demonstrates that both copolymer blocks are in close proximity (within ~1 nm) to the inorganic oxide matrix. These results are corroborated by separate TEM and SAXS measurements, which indicate that local separation of the copolymer blocks is incomplete at concentrations of 50 wt.% EO_{100}–PO_{70}–EO_{100} and below. The $^{29}Si\{^{1}H\}$ HETCOR spectra for the 50 wt.% block copolymer/silica composite establish that the PEO blocks interact with, and perhaps penetrate into, the silica network, consistent with the appearance of microporosity in the frameworks observed under certain conditions [141,146–148].

By comparison, for a EO_{100}–PO_{70}–EO_{100}/silica composite containing 62 wt.% of the triblock copolymer, the $^{29}Si\{^{1}H\}$ HETCOR spectrum in Fig. 17(b) reveals significantly increased separation of the different copolymer moieties and different interfacial proximities to the silica network. Two distinct peaks are observed in the 2D $^{29}Si\{^{1}H\}$ HETCOR contour plot that correlate signal intensity from the –OCH_2CH_2– PEO backbone protons at 4.0 ppm with that from Q^2 and Q^3 ^{29}Si species at −92 and −102 ppm, respectively. This confirms the close proximity of the PEO segments and the silica network. However, no correlated intensity is observed between the ^{29}Si Q^3 species and protons of the PPO –CH_3 group, in contrast to the $^{29}Si\{^{1}H\}$ HETCOR spectrum [Fig. 17(a)] for the 50 wt.% composite. The 1D ^{1}H MAS slice through the Q^3 peak plotted in Fig. 17(b) confirms a single correlation between the PEO protons and the Q^3 ^{29}Si sites. The absence of intensity correlations between the ^{1}H peak associated with the –CH_3 species of the PPO blocks and the ^{29}Si species in the silica framework demonstrates that the majority of PPO species have separated to distances greater than ca. 1 nm from the silica matrix. Such molecular evidence for local separation is in agreement with separate TEM and SAXS results that confirm the 62 wt.% block-copolymer/silica composite to be a highly ordered hexagonal mesophase. These results are consistent with the formation of block copolymer aggregates composed of central PPO cores surrounded by annular shells or layers of PEO ~1 nm thick that interact strongly with the silica network. The schematic diagrams in Fig. 17 depict the relative molecular partitioning and mesostructural ordering of the copolymer blocks and silica that are consistent with the NMR, SAXS, and TEM results. Collectively, they show increased mesoscale ordering for higher concentrations of the structure-directing triblock copolymer species.

For condensed mixed oxide systems, similar physicochemical self-assembly processes and resultant structures are observed. For example, De Paul et al. [149] studied an aluminosilica poly(isopropene-*b*-ethyleneoxide) hybrid material that is a candidate for applications in lithium batteries [150]. Their solid-state ^{27}Al and ^{29}Si MAS NMR measurements indicate that the structure of the aluminosilica framework in the hybrid material is not influenced strongly by the block copolymer, and that framework formation may be initiated before the addition of the block copolymer. Nevertheless, proton spin diffusion NMR experiments show a high degree of intermixing and no evidence for a well demarcated PEO interface between the inorganic aluminosilica and the polyisopropene moieties. These mechanistic and structural insights are expected to be generally applicable to the preparation of inorganic–organic hybrid materials [151–153].

3.4. Formation of molecularly ordered inorganic mesophase frameworks

As clearly shown in Fig. 1, one of the principal differences between zeolites and nearly all mesoporous inorganic materials prepared to date is the greatly different extents of molecular ordering in their frameworks. The high degrees of crystallinity found in zeolites and other molecular sieves are in stark contrast to the amorphous frameworks observed generally for materials prepared using surfactant, block copolymer, or emulsion structure-directing agents. Practically, these differences have enormous effects on the macroscopic properties of the different materials, including their adsorption, reaction, hydrothermal and mechanical stability behaviors. As a consequence, considerable synthetic effort has been devoted to developing mesoporous inorganic solids with crystalline frameworks, based on variations and combinations of the approaches discussed above for zeolites and surfactant-templated solids. Until now, however, local ordering of inorganic oxide-mesophase frameworks has been rare and observed only under certain conditions. This has been due, in part, to the difficulty of using elevated

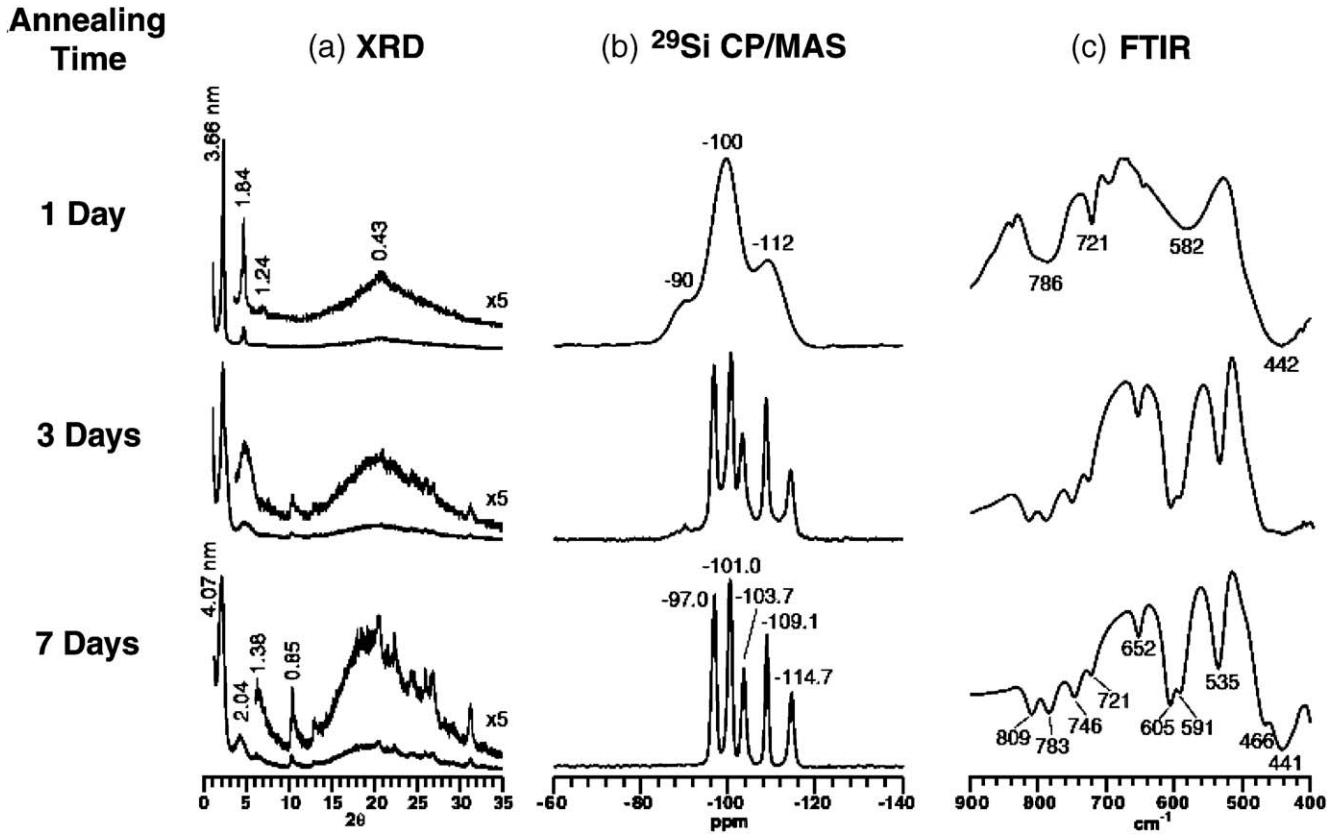

Fig. 18. A series of (a) small-angle X-ray powder diffraction patterns, (b) ^{29}Si CP/MAS NMR spectra, and (c) FTIR spectra for silica–surfactant mesophases synthesized using cetyldimethylethylammonium bromide ($C_{16}NMe_2Et_1Br$) and annealed at 135 °C for different lengths of time. [Reprinted with permission from Ref. [154]. Copyright 2001 American Chemical Society.]

temperatures (>140 °C) in surfactant-based inorganic–organic mesophase syntheses. Such conditions can lead to a degradation of the surfactant species, triggering a collapse of the organized mesostructure and/or the formation of crystalline zeolites. The use of lower temperatures (<100 °C) allows well-ordered mesostructured products to form, but typically with disordered inorganic frameworks.

Nevertheless, under carefully controlled conditions, self-assembled silicate–surfactant mesophase solids can be synthesized with crystal-like molecular ordering in their inorganic frameworks [104,154–156]. Among the important synthesis variables are solution pH, surfactant head group composition, temperature, and crystallization time. The head group moiety of the surfactant is particularly important, because of its position at the hydrophobic–hydrophilic interface, where it interacts directly with the solution environment, inorganic precursor species, and the resultant solid network. In fact, as in zeolites, the use of different cationic alkylammonium head groups under otherwise identical alkaline conditions has been shown to lead to layered silicate–surfactant mesophases with different 2D crystal-like framework structures [154]. A combination of solid-state ^{29}Si CP/MAS NMR, X-ray diffraction (XRD), and Fourier transform infrared (FTIR) spectroscopy measurements show the development and evolution of molecular framework ordering in lamellar silicate–surfactant composites. For example, as shown in Fig. 18, a lamellar silica–$C_{16}N^+Me_2Et_1$ (where Me represents a $-CH_3$ methyl group, Et represents a $-C_2H_5$ ethyl group, and C_{16} represents an alkyl chain with 16 carbon atoms) mesophase with an initially amorphous silica lattice transforms over time (~1 week, pH 11.5, 135 °C) into a similarly layered product, but with crystal-like ordering in its silicate framework. This is evident by inspection of X-ray diffraction patterns [Fig. 18(a)] at selected time intervals, which show the retention of the characteristic (*100*) and (*200*) reflections at small 2θ angles corresponding to a layered mesostructure. More importantly, the ^{29}Si CP/MAS spectra in Fig. 18(b) of the same bulk samples show dramatic reductions in the ^{29}Si linewidths during these same time intervals, corresponding to the transformation of the initially amorphous framework into one with crystal-like molecular order. After 7 days, five well-resolved ^{29}Si peaks are observed indicating the presence of five distinct tetrahedrally coordinated Si sites in the bulk silicate–$C_{16}N^+Me_2Et_1$ product. Such molecular order is evident in poorly resolved XRD reflections at wide-scattering angles ($2\theta > 10°$) [Fig. 18(a), bottom] and also manifested in the appearance of narrow FTIR bands associated with silicate framework vibrations [Fig. 18(c), bottom]. Wang and Exarhos have studied similar silicate–$C_{16}N^+Me_3$ (i.e., CTA^+) materials with ordered frameworks using a combination of ^{29}Si and ^{13}C MAS, $^{13}C\{^1H\}$ CP buildup curves, $^{13}C\{^1H\}$ wideline-separation NMR and X-ray diffraction to analyze the framework structures and surfactant dynamics [155]. Xia et al. interestingly showed that starting with siliceous hexagonal MCM-41 (also using CTA^+), the initially amorphous framework transformed into a molecularly

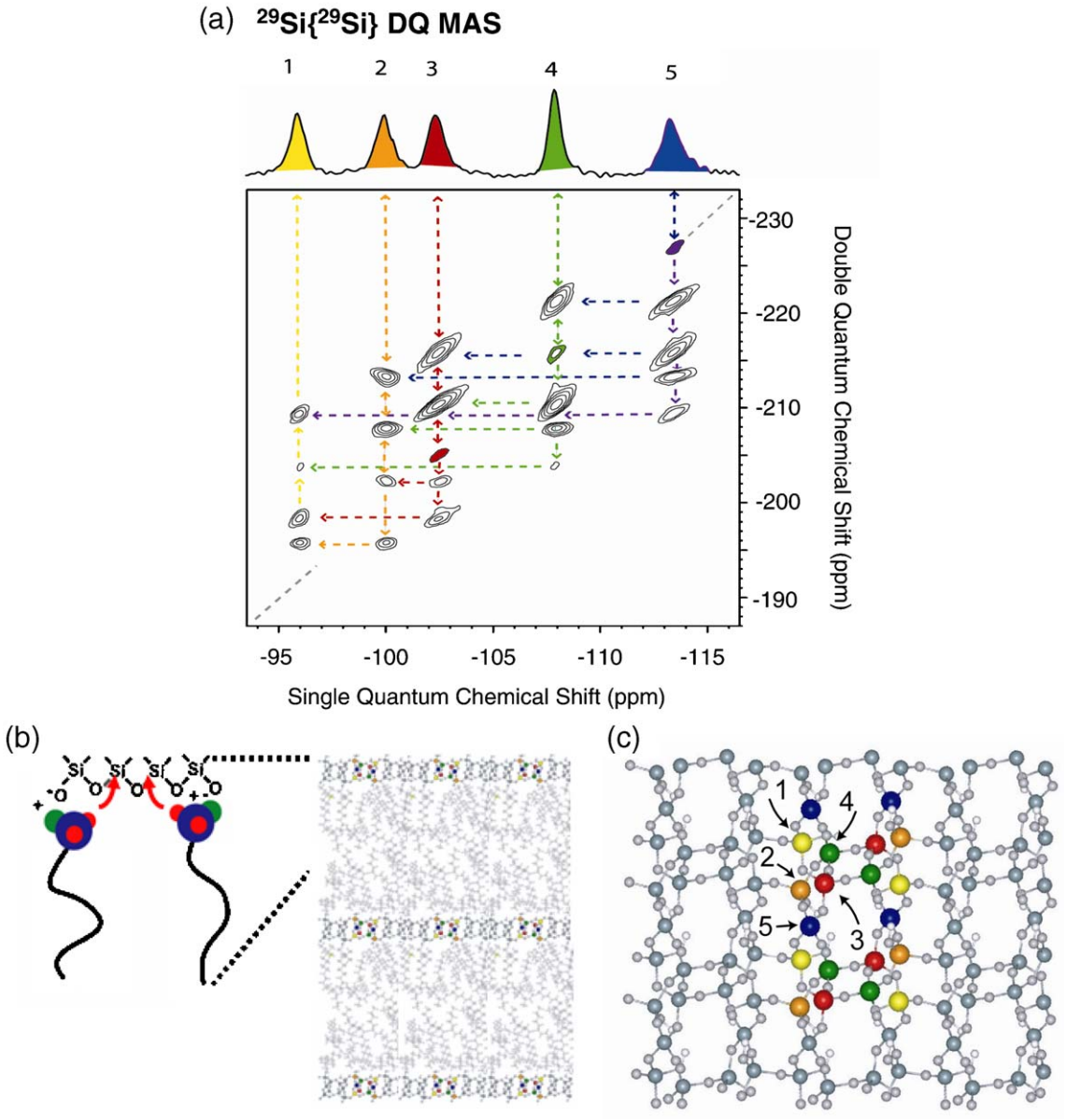

Fig. 19. (a) Dipole–dipole-mediated 2D Double-Quantum $^{29}Si\{^{29}Si\}$ MAS NMR spectrum from a lamellar silicate–$C_{16}N^{+}Me_2Et_1$ mesophase with a molecularly ordered framework. A single-pulse ^{29}Si MAS NMR spectrum accompanies the contour plot along the horizontal single-quantum dimension, while the double-quantum dimension lies along the vertical axis. (b) Schematic of the interaction of the organic surfactant with the inorganic silica framework. (c) Top-view of the 2D silicate framework; the surfactant molecules are excluded for clarity. [Adapted with permission from Ref. [104]. Copyright 2004 American Chemical Society.]

ordered one, although the XRD results showed that this was accompanied by a transformation through a cubic phase finally to a layered material [156]. This indicates that structure-directing functions are provided by different components at different stages of the synthesis, initially by self-assembly of the surfactant species and subsequently by two-dimensional crystallization of the inorganic framework.

More detailed determination of the ordered framework structures, however, has been challenging, due to the absence of 3D crystallinity in the silicate–surfactant solids, which precludes meaningful analysis at molecular length scales by scattering methods. Nevertheless, the combination of powerful new techniques of solid-state NMR, X-ray diffraction, and molecular modeling, permit the structural determination of complex molecularly ordered inorganic frameworks, despite the lack of 3D molecular periodic ordering. Hedin et al., for example, have recently shown that by using 2D double-quantum (DQ) $^{29}Si\{^{29}Si\}$ NMR techniques, the interconnectivity relationships among the five tetrahedrally coordinated framework silicon sites in the ordered silicate–$C_{16}N^{+}Me_2Et_1$ composite of Fig. 18(b),bottom are unambiguously and uniquely established [104]. Fig. 19 shows a $^{29}Si\{^{29}Si\}$ double-quantum spectrum in which intensity correlations are observed among nearest- and next-nearest ^{29}Si sites, which greatly constrain the possible framework configurations. In fact, out of a very large number of possible framework configurations, only one set of tetrahedrally coordinated Si site connectivities is consistent with the NMR measurements. By invoking

additional constraints imposed by small- and wide-angle XRD data [Fig. 18(a), bottom], an energy-minimized structure was calculated using empirical force fields, as well as quantum chemical modeling. The results were subsequently cross-validated and tested for self-consistency by comparison with predicted isotropic ^{29}Si NMR chemical shifts obtained from separate ab initio calculations. Fig. 19(b,c) shows different orientations of the energy minimized structure of the layered silicate framework, which contains four- and six-membered rings that are commonly observed in zeolites. The 2D double-quantum ^{29}Si{^{29}Si} NMR measurements provided the crucial new inputs that allowed the structural analysis to advance, even without 3D crystallinity. It is anticipated that such DQ NMR methods will be generally applicable to structural studies of other complicated siliceous molecular sieves, clays, or phyllosilicates, or to phosphates, phosphides, and other complex solid materials containing ^{31}P or other dipole–dipole-coupled spin $I=1/2$ nuclei in moderate abundances.

3.5. Formation of transition-metal-containing mesoporous materials

While siliceous mesoporous materials are the most extensively studied class of mesoporous solids, other such materials are of significant technological interest as well [157]. The hydrothermal synthesis strategies developed for siliceous mesoporous materials have been extended to the incorporation of other heteroatom transition metal oxides into mesoporous silica frameworks and the preparation of mesoporous transition metal oxide materials. For example, materials incorporating titania into a mesoporous silica framework exhibit low thermal expansion coefficients and promising catalytic, optical, and combined photocatalytic properties [158,159]. Due to the richer and more complex chemistry of transition metals, especially in hydrothermal reaction mixtures, only a few studies have been reported on the mechanisms of nucleation and growth in these materials.

Solution- and solid-state ^{17}O NMR is particularly useful for monitoring local chemical environments of inorganic precursor species or condensed networks containing heteroatoms, such as Ti, that are inconvenient or not amenable to NMR investigations themselves. Gervais et al. [160] studied the evolution of amorphous titania–silica precursor gels by solution- and solid-state ^{17}O NMR. However, a challenging aspect of sol–gel syntheses involving co-condensation of titania and silica is the prevention of phase-separation during hydrolysis and cross-linking of the silicon alkoxides and titanium alkoxides (or other precursors.) In addition, due to the low natural abundance of ^{17}O ($I=5/2$, 0.037% nat. abund.), samples must generally be enriched in ^{17}O. Fig. 20 shows solution-state ^{17}O NMR spectra of a hydrolyzed solution of tetraethoxysilane (TEOS) at pH=2 before and at various times after the addition of Ti butoxide. The ^{17}O NMR spectrum of the TEOS precursor solution in Fig. 20(a) exhibits a resonance at ca. 30 ppm corresponding to

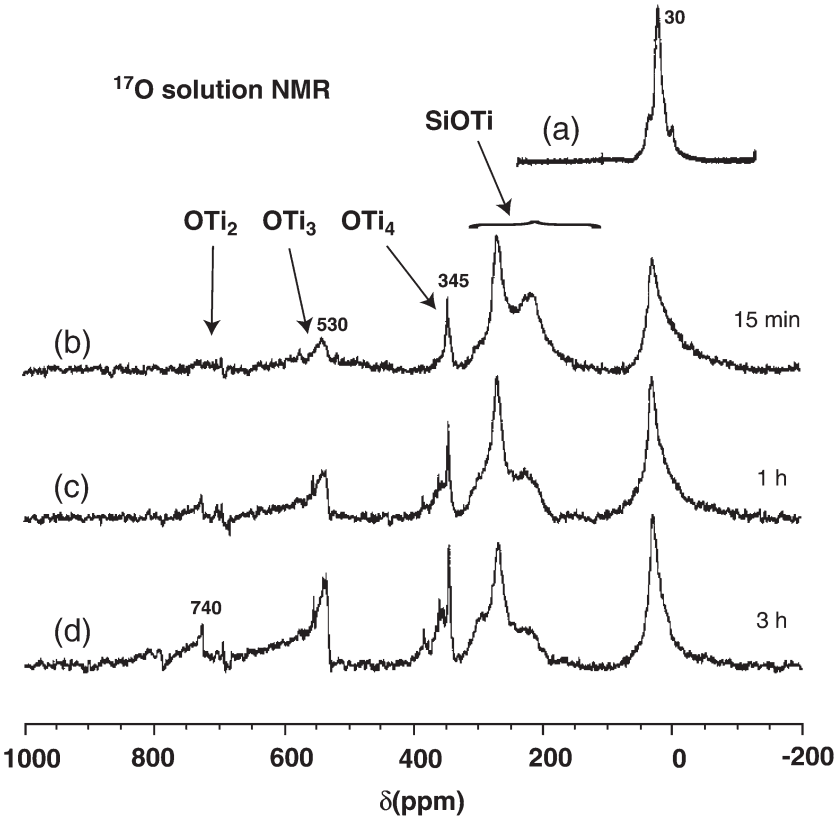

Fig. 20. ^{17}O NMR spectra of a hydrolyzed solution of TEOS (a) before and (b)–(d) after addition of Ti(OBu^n)$_4$ after (b) 15 min, (c) 1 h and (d) 3 h. [Reprinted with permission from Ref. [160]. Copyright 2001 American Chemical Society.]

oxygen atoms associated with Si–^{17}OH and Si–^{17}O–Si species. After the addition of Ti butoxide, the spectrum in Fig. 20(b) shows broad resonances between 200 and 300 ppm assigned to Si–^{17}O–Ti bridges [161] and two weak signals at 345 ppm and 530 ppm, corresponding to oxygen bridges in $^{17}OTi_4$ and $^{17}OTi_3$ environments, respectively [161,162]. This indicates the relatively rapid and preferential formation of Si–O–Ti linkages compared to Ti–O–Ti species. Subsequent aging of the system was followed by solution-state ^{17}O NMR for 17 h, but only during the first 3 h were changes in the spectra observed. During this time, a decrease in the signal intensity assigned to Si–^{17}O–Ti species took place, accompanied by increased signal intensities associated with the $^{17}OTi_4$, $^{17}OTi_3$, and $^{17}OTi_2$ (~740 ppm) moieties; signals corresponding to Si–^{17}O–Si linkages showed little change in relative integrated intensity. The ^{17}O NMR results thus suggest that the formation of Si–O–Ti linkages is favored kinetically during the reaction of hydrolyzed titanium alkoxides with dissolved silica species. Such mixtures, nevertheless, continue to evolve slowly, with the appearance of more Ti–O–Ti species, until this redistribution is apparently halted by gelation. ^{17}O MAS NMR spectra (not shown here) of the samples separately suggest that at least two types of Si–^{17}O–Ti linkages are present in the gels, one being Si–O–TiO_3 species that contribute to ^{17}O MAS signals at 290–315 ppm and are stable to 750 °C, while the other contains three-coordinated oxygen atoms linked to one silicon and two titanium atoms Si–O–$(TiO_3)_2$ that accounts for an ^{17}O MAS signal at 174 ppm and is less stable to heat treatment. Further information could be gained by solution- and solid-state ^{29}Si NMR measurements which would provide separate complementary information on the evolution of the inorganic network.

Few NMR studies have been conducted to investigate the mechanisms by which ordered non-siliceous mesostructured transition-metal oxides, such as titania or vanadia, self-assemble and grow. Due to the complex reactions that transition-metal oxide species undergo during hydrolysis, condensation, and their interactions with structure-directing species, the processes by which they form mesostructured materials are less well understood, compared to mesostructured silicas. The syntheses of mesostructured transition-metal oxides can be studied at a molecular-level by NMR, as above, provided they have convenient NMR-active isotopes. One suitable example is vanadia, for which ^{51}V (I=7/2, 100% nat. abund.) NMR can be used as a probe of solution- and solid-state physicochemical structures and processes associated with the vanadia–surfactant co-assembly. Soler-Illia and Sanchez have studied chelation and complexation of vanadium in different VO(O-*tert*-Am)$_3$–surfactant solutions by ^{51}V NMR [163]. Vanadium was chosen because its interactions with different self-assembling surfactant species were hypothesized to be similar to technologically important titanium, though with an isotope more suitable for direct study. Fig. 21 shows solution-state ^{51}V NMR spectra acquired for non-aqueous mixtures of VO(O-*tert*-Am)$_3$ (VOTAM) and different surfactants in the organic solvent tetrahydrofuran (THF). The assignments of the ^{51}V resonances were made by comparisons with ^{51}V NMR signals for VOTAM in THF and for similar solutions containing VOTAM and

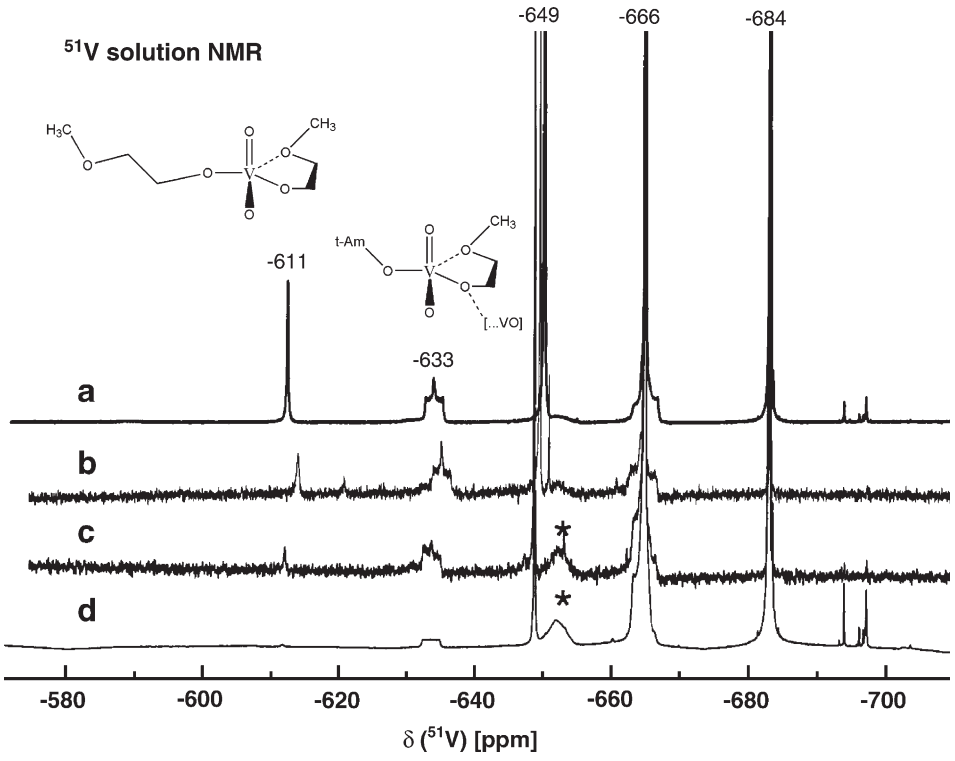

Fig. 21. Solution-state ^{51}V NMR spectra of VO(O-*tert*-Am)$_3$–surfactant systems in THF with (a) methoxyethanol or surfactants (b) P123, (c) F127 or (d) Brij 56. The asterisks denote peaks attributed to double hydrolysis of VO(O-*tert*-Am)$_3$. [Adapted from Ref. [163]—reproduced by permission of The Royal Society of Chemistry (RSC) on behalf of the Centre National de la Recherche Scientifique (CNRS).]

increasing amounts of methoxyethanol $MeOCH_2CH_2OH$. The ^{51}V NMR spectrum of a solution of VOTAM and methoxyethanol in a ratio of 1:2 is shown in Fig. 21(a). The resonances at −684 ppm and −666 ppm can be attributed to VO(O-*tert*-Am)$_3$ and the hydrolysis product VOOH(O-*tert*-Am)$_2$, which are also found in the pure VOTAM solution. The peak at −649 ppm represents a species, in which one *tert*-amyloxy group has been replaced by a methoxyethanol group that is coordinated as a monodentate ligand to the central vanadium atom. The resonances at −633 and −611 ppm correspond to five-coordinated vanadium species, in which vanadium is chelated by methoxyethanol as a bidentate ligand. Variations of the templating agent or the surfactant/VOTAM ratio show little influence on the ^{51}V NMR spectra. Fig. 21(b)–(d) show the ^{51}V spectra of a non-aqueous VOTAM solution (THF) containing the surfactants P123 [$(EO)_{20}(PO)_{70}(EO)_{20}$], F127 [$(EO)_{100}(PO)_{70}(EO)_{100}$] and Brij 56 [$C_{16}H_{33}(EO)_{10}OH$], respectively. The spectra contain the same resonances as observed in Fig. 21(a), but exhibit different structures in the peaks centered at −633 ppm, which is ascribed to the presence of V–O–V linkages formed by the oligomerization of vanadium species complexed by the block copolymer. ^{51}V signals attributed to V–O–V linkages indicate slow condensation to transition-metal-oxide oligomers and small clusters, once the metal species are complexed by the hydrophilic PEO moieties. In the presence of small amounts of water, such as may be provided by moisture in the air or trace water, these vanadia oligomers can further condense to form 'worm-like' vermicular mesophases, whose solution-state ^{51}V NMR signals ultimately vanish, as solid mesostructured products are formed. This chelation-like behavior of vanadium in aprotic solvents is hypothesized to be similar to that of titanium and points to interesting implications for the large influence of water on the structures present during the formation of mesoporous titania thin films.

Since mesoporous titania is of high technological as well as fundamental interest, its preparation has been extensively studied in the forms of powders and thin films [164]. Molecular mechanistic investigations by ^{47}Ti (I=5/2, 7.3% nat. abund.) or ^{49}Ti (I=7/2, 5.5% nat. abund.) NMR are generally not feasible, however, due to the very low signal sensitivities (small gyromagnetic ratios) and quadrupolar characters of both isotopes. Initially the formation of titania was proposed to occur via a non-hydrolytic condensation mechanism [165]. More recently, evaporation-induced self-assembly [166] (EISA)-derived approaches using controlled amounts of water for the synthesis of mesoporous titania thin films from alkoxide–alcohol–water–hydrochloric acid mixtures have been shown to yield higher control over the structures of titania–surfactant mesophases [163,166–169]. Sanchez and coworkers conducted studies applying a variety of spectroscopic methods, including EXAFS, time-resolved synchrotron-SAXS, interferometry, FTIR, and solution-state ^{13}C and ^{17}O NMR to examine the formation mechanisms of mesostructured titania and especially the influence of water on the syntheses [167,170]. The importance of water was demonstrated by solution-state ^{17}O NMR of the complexation behaviors of transition metal oxides with block copolymers in THF solutions with low water contents.

In accordance with the ^{51}V NMR findings above, in ethanol-rich Ti–surfactant–ethanol solutions typically used in mesoporous titania syntheses, interactions between the hydrophilic PEO moieties and hydrolyzed Ti should be suppressed [167]. The reaction of $TiCl_4$ precursor species with ethanol yields titanium chloroethoxide [$TiCl_{4-x}(OEt)_x$], where x is approximately 2. Upon the evaporation of ethanol during dip-coating or otherwise and after aging at temperatures of 40–70 °C, chelation-like interactions of soluble titania species with the hydrophilic PEO blocks increase and become increasingly predominant. In ethanolic solutions containing very small amounts of water, strong interactions with soluble metal oxide species can diminish the solubility difference between the PEO and PPO moieties, thereby reducing the tendency of the block copolymer species to self-assemble into micelles or mesophases. As for vanadia, the presence of water induces rapid condensation of the metal alkoxides to hydrophilic titanium-oxo oligomers and clusters that interact with the PEO copolymer blocks via hydrogen bonds. For water/TiO_2 ratios greater than four, the reaction solution contains hydrolyzed hydrophilic moieties that are predominantly dimers bridged by μ_2-oxygen species, as evidenced by ^{17}O NMR [160,167]. These oligomeric species are anticipated to perturb less (and may even enhance) the solubility difference of the PPO and PEO moieties of the block copolymer, and thereby promote the formation of micelles. As the extent of condensation of such species increases under acidic conditions, mesostructured titania gels or precipitates of cubic, hexagonal, or lamellar structures can form, as directed by the block copolymer structure-directing agents.

In general, the physicochemical processes of self-assembly, complexation, and condensation of transition-metal-oxide (and other inorganic) networks in the presence of block copolymer or surfactant species are expected to be dependent on numerous variables, especially solution composition and processing conditions. For example, during dip-coating operations to prepare mesostructured thin films, water and HCl can concentrate in the film, due to a fast evaporation of more volatile ethanol or THF solvent species. As a result, time-dependent compositions and gradients may exert large influences on the structure(s) of the evolving mesophase(s), the aggregation behavior(s) of condensing titania species, and their interactions with the self-assembling block copolymer agents. Elevated temperatures between 60 and 160 °C often lead to increased condensation of the metal oxide framework associated with the self-assembled mesophase and to stable mesostructured hybrid films. The template molecules can be removed by heat treatment of 300–400 °C, yielding lamellar, cubic, or hexagonal titania mesostructured thin films.

4. Outlook and conclusions

New developments in magnetic resonance spectroscopy are advancing significantly our understanding of the mechanisms by which ordered domains of nano- and mesostructured inorganic solids develop and grow. In situ NMR and EPR

methods introduced in recent years promise to yield more detailed insights into the solution- and solid-state species involved in the nucleation and evolution of ordered aggregates in complicated zeolite and mesoporous materials systems. These methods are especially vital for the study of dynamic processes in the syntheses that cannot be carried out under equilibrium conditions. Complementary in situ and ex situ solution- and solid-state NMR and EPR studies of hydrothermal reaction mixtures may clarify the role of solution-state precursor species and their interactions with intermediate amorphous phases prior to the onset of crystallization. Much of our understanding of the processes that govern nucleation and growth of ordered domains in these systems has come from a combination of the molecular-level insights provided by NMR and EPR with longer-range structural and morphological information obtained from diffraction and electron microscopy experiments, respectively. NMR methods that exploit heteronuclear dipolar couplings like CP/MAS or HETCOR are powerful tools for gaining information about interactions between organic structure-directing molecules and inorganic frameworks. Such information is needed to extend our knowledge of the key mechanistic role(s) that organic molecules play in the onset, development, and evolution of order during the formation of crystalline or mesostructured inorganic solids. Other recently introduced methods that exploit homonuclear $^{29}Si–^{29}Si$ dipole–dipole or *J*-coupling interactions to establish framework site-connectivities open new opportunities for refining the structures of known materials, as well as determining the structures of new materials or intermediates that lack long range order. Recent advances in NMR techniques, such as MQ-MAS, that allow high-resolution solid-state NMR spectra of quadrupolar nuclei to be measured promise to contribute new insights into the nature of aluminum and other quadrupolar species in heterogeneous framework environments.

NMR and EPR spectroscopy allow organization and reorganization processes occurring during the development and evolution of order in porous materials to be followed at a molecular level. Such information can provide detailed insights into the processes that are responsible for the nucleation and growth of nanoporous and mesoporous inorganic materials. Although both nanoporous molecular sieves and mesoporous inorganic solids are synthesized from a wide variety of compositions under different conditions, some common themes emerge from the mechanistic studies of their formation. Both are synthesized from solutions governed by complex solution-state chemistries, often in the presence of structure-directing organic molecules. The nature of the solution-state species and their equilibria and kinetics can be monitored by solution-state NMR. From solution, precursor species assemble to form gel-like intermediates without long-range atomic order of the condensing inorganic framework, although surfactant or block copolymer species can impart mesoscopic framework organization over longer length scales. Condensation proceeds and order develops under the influence of the structure-directing agents, which promote solidification of the framework and lead to nanoporous crystalline zeolite molecular sieves or mesostructured amorphous (or under certain conditions, 2D crystalline) frameworks. As shown by the different studies examined here, significant physicochemical differences often exist at various stages of the formation processes, which depend greatly on the compositions and conditions of the respective reaction mixtures. Nevertheless, common underlying thermodynamic and kinetic phenomena closely link the various materials and the mechanisms by which they form. These common characteristics become clearer at a molecular level, underscoring the utility and importance of the detailed molecular insights provided by NMR and EPR spectroscopy.

Acknowledgments

The authors gratefully acknowledge the contributions from their coworkers, collaborating groups and colleagues to the body of work presented here, both within and outside the scope of the review topics discussed. Current and past funding support for research in these areas is acknowledged by B.F.C. from the U.S. National Science Foundation, the U.S. Department of Energy, and the USARO.

References

[1] Beck JS, Vartuli JC, Roth WJ, Leonowicz ME, Kresge CT, Schmitt KD, et al. A new family of mesoporous molecular sieves prepared with liquid crystal templates. J Am Chem Soc 1992;114:10834–43.
[2] Camblor MA, Corma A, Lightfoot P, Villaescusa LA, Wright PA. Synthesis and structure of ITQ-3, the first pure silica polymorph with a two-dimensional system of straight eight-ring channels. Angew Chem, Int Ed Engl 1997;36:2659–61.
[3] Olson DH, Camblor MA, Villaescusa LA, Kuehl GH. Light hydrocarbon sorption properties of pure silica Si–CHA and ITQ-3 and high silica ZSM-58. Microporous Mesoporous Mater 2004;67:27–33.
[4] Cundy CS, Cox PA. The hydrothermal synthesis of zeolites: history and development from the earliest days to the present time. Chem Rev 2003;103:663–701.
[5] Davis ME, Lobo RF. Zeolite and molecular-sieve synthesis. Chem Mater 1992;4:756–68.
[6] Breck DW. Zeolite molecular sieves. New York: John Wiley & Sons; 1974.
[7] Szostak R. Molecular sieves—principles of synthesis and identification. 2nd ed. London: Blackie; 1989.
[8] Francis RJ, O'Hare D. The kinetics and mechanisms of the crystallisation of microporous materials. J Chem Soc Dalton Trans 1998:3133–48.
[9] Cundy CS, Cox PA. The hydrothermal synthesis of zeolites: precursors, intermediates and reaction mechanisms. Microporous Mesoporous Mater 2005;82:1–78.
[10] Cheetham AK, Mellot CF. In situ studies of the sol–gel synthesis of materials. Chem Mater 1997;9:2269–79.
[11] Klinowski J. Applications of solid-state NMR for the study of molecular sieves. Anal Chim Acta 1993;283:929–65.
[12] Haw JF, Nicholas JB, Xu T, Beck LW, Ferguson DB. Physical organic chemistry of solid acids: lessons from in situ NMR and theoretical chemistry. Acc Chem Res 1996;29:259–67.
[13] Ivanova II. Application of in situ MAS NMR for elucidation of reaction mechanisms in heterogeneous catalysis. Colloids Surf A 1999; 158:189–200.
[14] Han XW, Yan ZM, Zhang WP, Bao XH. Application of in situ NMR in catalytic processes of organic reactions. Curr Org Chem 2001; 5:1017–37.
[15] Hunger M. Applications of in situ spectroscopy in zeolite catalysis. Microporous Mesoporous Mater 2005;82:241–55.

[16] Hunger M. Brønsted acid sites in zeolites characterized by multinuclear solid-state NMR spectroscopy. Catal Rev Sci Eng 1997;39:345–93.
[17] Blumenfeld AL, Fripiat JJ. Acid sites topology in aluminas and zeolites from high-resolution solid-state NMR. Top Catal 1997;4:119–29.
[18] Springuel-Huet MA, Bonardet JL, Fraissard J. Xe-129-NMR of physisorbed xenon used as a probe for the study of microporous solids. Appl Magn Reson 1995;8:427–56.
[19] Shantz DF, Lobo RF. Guest–host interactions in zeolites as studied by NMR spectroscopy: Implications in synthesis, catalysis and separations. Top Catal 1999;9:1–11.
[20] Bell AT. NMR applied to zeolite synthesis. Colloids Surf A 1999;158:221–34.
[21] Barrer RM, Baynham JW, Bultitude FW, Meier WM. Hydrothermal chemistry of silicates: 8. Low-temperature crystal growth of aluminosilicates, and of some gallium and germanium analogues. J Chem Soc 1959:195.
[22] Harris RK, Knight CTG. Silicon-29 NMR studies of aqueous silicate solutions. J Mol Struct 1982;78:273–8.
[23] Engelhardt G, Michel D. High resolution solid state NMR of silicates and zeolites. New York: John Wiley and Sons; 1987.
[24] McCormick AV, Bell AT. The solution chemistry of zeolite precursors. Catal Rev Sci Eng 1989;31:97–127.
[25] Knight CTG, Syvitski RT, Kinrade SD. Aqueous silicate chemistry in zeolite synthesis. Stud Surf Sci Catal 1995;97:483–8.
[26] Knight CTG. Are zeolite secondary building units really red herrings? Zeolites 1990;10:140–4.
[27] Harris RK, Parkinson J, Samadi-Maybodi A. A novel symmetric silicate anion. J Chem Soc Dalton Trans 1997:2533–4.
[28] Kinrade SD, Donovan JCH, Schach AS, Knight CTG. Two substituted cubic octameric silicate cages in aqueous solution. J Chem Soc Dalton Trans 2002:1250–2.
[29] Kirschhock CEA, Ravishankar R, Verspeurt F, Grobet PJ, Jacobs PA, Martens JA. Identification of precursor species in the formation of MFI zeolite in the TPAOH–TEOS–H_2O system. J Phys Chem B 1999;103:4965–71.
[30] Kirschhock CEA, Kremer SPB, Grobet PJ, Jacobs PA, Martens JA. New evidence for precursor species in the formation of MFI zeolite in the tetrapropylammonium hydroxide–tetraethyl orthosilicate–water system. J Phys Chem B 2002;106:4897–900.
[31] Houssin CJY, Kirschhock CEA, Magusin PCMM, Mojet BL, Grobet PJ, Jacobs PA, et al. Combined in situ ^{29}Si NMR and small-angle X-ray scattering study of precursors in MFI zeolite formation from silicic acid in TPAOH solutions. Phys Chem Chem Phys 2003;5:3518–24.
[32] Knight CTG, Kinrade SD. Comment on "Identification of precursor species in the formation of MFI zeolite in the TPAOH–TEOS–H_2O system". J Phys Chem B 2002;106:3329–32.
[33] Kinrade SD, Knight CTG, Pole DL, Syvitski RT. Silicon-29 NMR studies of tetraalkylammonium silicate solutions: 1. Equilibria, ^{29}Si chemical shifts, ^{29}Si relaxation. Inorg Chem 1998;37:4272–7.
[34] Kinrade SD, Knight CTG, Pole DL, Syvitski RT. Silicon-29 NMR studies of tetraalkylammonium silicate solutions: 2. Polymerization kinetics. Inorg Chem 1998;37:4278–83.
[35] Hendricks WM, Bell AT, Radke CJ. Effects of organic and metal cations on the distribution of silicate anions in aqueous solutions. J Phys Chem 1991;95:9513–8.
[36] Hendricks WM, Bell AT, Radke CJ. Effects of solvent structure on the distribution of silicate anions in mixed aqueous/organic solutions of alkaline tetramethylammonium silicate. J Phys Chem 1991;95:9519–24.
[37] Hasegawa I, Sakka S, Sugahara Y, Kuroda K, Kato C. Silicate anions formed in tetramethylammonium silicate methanolic solutions as studied by ^{29}Si nuclear magnetic resonance. J Chem Soc Chem Commun 1989:208–10.
[38] Barrer RM. Hydrothermal chemistry of zeolites. New York: Academic Press; 1982.
[39] Ginter DM, Went GT, Bell AT, Radke CJ. A physicochemical study of the aging of colloidal silica gels used in zeolite Y synthesis. Zeolites 1992;12:733–41.
[40] Ginter DM, Bell AT, Radke CJ. The effects of gel aging on the synthesis of NaY zeolite from colloidal silica. Zeolites 1992;12:742–9.
[41] Ogura M, Kawazu Y, Takahashi H, Okubo T. Aluminosilicate species in the hydrogel phase formed during the aging process for the crystallization of FAU zeolite. Chem Mater 2003;15:2661–7.
[42] Shi J, Anderson MW, Carr SW. Direct observation of zeolite A synthesis by in situ solid-state NMR. Chem Mater 1996;8:369–75.
[43] Engelhardt G, Fahlke B, Mägi M, Lippmaa E. High-resolution solid-state ^{29}Si and ^{27}Al n.m.r. of aluminosilicate intermediates in zeolite A synthesis. Zeolites 1983;3:292–4.
[44] Engelhardt G, Fahlke B, Mägi M, Lippmaa E. High-resolution solid-state ^{29}Si and ^{27}Al n.m.r. of aluminosilicate intermediates in the synthesis of zeolite A: Part II. Zeolites 1985;5:49–52.
[45] Mintova S, Valtchev V. Effect of the silica source on the formation of nanosized silicalite-1: an in situ dynamic light scattering study. Microporous Mesoporous Mater 2002;55:171–9.
[46] Lippmaa E, Mägi M, Samoson A, Tarmak M, Engelhardt G. Investigation of the structure of zeolites by solid-state high-resolution ^{29}Si NMR spectroscopy. J Am Chem Soc 1981;103:4992–6.
[47] Smaihi M, Barida O, Valtchev V. Investigation of the crystallization stages of LTA-type zeolite by complementary characterization techniques. Eur J Inorg Chem 2003:4370–7.
[48] Freude D, Haase J. Quadrupole effects in solid-state nuclear magnetic resonance. In: Diehl P, Fluck E, Günther H, Kasfeld R, Seelig J, editors. NMR Basic Principles and Progress, vol. 29. Berlin: Springer-Verlag; 1993. p. 3–90.
[49] Smith ME, van Eck ERH. Recent advances in experimental solid state NMR methodology for half-integer spin quadrupolar nuclei. Prog Nucl Magn Res Spectrosc 1999;34:159–201.
[50] Klinowski J, Thomas JM, Fyfe CA, Gobbi GC. Monitoring of structural changes accompanying ultrastabilization of faujasitic zeolite catalysts. Nature 1982;296:533–6.
[51] Freude D, Brunner E, Pfeifer H, Prager D, Jerschkewitz H-G, Lohse U, et al. Magic-angle-spinning NMR studies of dealuminated zeolites. Chem Phys Lett 1987;139:325–30.
[52] Coster D, Blumenfeld AL, Fripiat JJ. Lewis acid sites and surface aluminum in aluminas and zeolites: a high-resolution NMR study. J Phys Chem 1994;98:6201–11.
[53] Remy MJ, Stanica D, Poncelet G, Feijen EJP, Grobet PJ, Martens JA, et al. Dealuminated H–Y zeolites: relation between physicochemical properties and catalytic activity in heptane and decane isomerization. J Phys Chem 1996;100:12440–7.
[54] Medek A, Harwood JS, Frydman L. Multiple-quantum magic-angle spinning NMR: a new method for the study of quadrupolar nuclei in solids. J Am Chem Soc 1995;117:12779–87.
[55] Amoureux J-P, Fernandez C, Steuernagel S. Z filtering in MQMAS NMR. J Magn Reson Ser A 1996;123:116–8.
[56] Medek A, Frydman L. Multiple-quantum magic-angle spinning NMR: a new technique for probing quadrupolar nuclei in solids. J Braz Chem Soc 1999;10:263–77.
[57] Rocha J, Morais CM, Fernandez C. Progress in multiple-quantum magic-angle spinning NMR spectroscopy. Top Curr Chem 2004;246:141–94.
[58] Brown SP, Wimperis S. Two-dimensional multiple-quantum MAS NMR of quadrupolar nuclei: a comparison of methods. J Magn Reson 1997;128:, 42–61.
[59] Chmelka BF, Zwanziger JW. Solid-state NMR line narrowing methods for quadrupolar nuclei: double rotation and dynamic-angle spinning. In: Kosfeld P, Blümich B, editors. NMR Basic Principles and Progress, vol. 33. Berlin: Springer-Verlag; 1994. p. 79–124.
[60] Alemany LB, Callender RL, Barron AR, Steuernagel S, Iuga D, Kentgens APM. Single-pulse MAS, selective Hahn echo MAS, and 3QMAS NMR studies of the mineral zoisite at 400, 500, 600, and 800 MHz. Exploring the limits of Al NMR detectability. J Phys Chem B 2000;104:11612–6.
[61] Fyfe CA, Bretherton JL, Lam LY. Detection of the 'invisible aluminium' and characterisation of the multiple aluminium environments in zeolite USY by high-field solid-state NMR. Chem Commun 2000;17:1575–6.

[62] Fyfe CA, Bretherton JL, Lam LY. Solid-state NMR detection, characterization, and quantification of the multiple aluminum environments in US-Y catalysts by ^{27}Al MAS and MQMAS experiments at very high field. J Am Chem Soc 2001;123:5285–91.
[63] Yang H, Walton RI, Antonijevic S, Wimperis S, Hannon AC. Local order of amorphous zeolite precursors from ^{29}Si{^{1}H} CPMAS and ^{27}Al and ^{23}Na MQMAS NMR and evidence for the nature of medium-range order from neutron diffraction. J Phys Chem B 2004;108:8208–17.
[64] Kunath-Fandrei G, Bastow TJ, Hall JS, Jäger C, Smith ME. Quantification of aluminum coordinations in amorphous aluminas by combined central and satellite transition magic angle spinning NMR spectroscopy. J Phys Chem 1995;99:15138–41.
[65] Antonijevic S, Ashbrook SE, Walton RI, Wimperis S. A multiple-quantum ^{23}Na MAS NMR study of amorphous sodium gallium silicate zeolite precursors. J Mater Chem 2002;12:1469–74.
[66] Fricke R, Kosslick H, Lischke G, Richter M. Incorporation of gallium into zeolites: syntheses, properties and catalytic application. Chem Rev 2000;100:2303–405.
[67] Xu W, Dong J, Li J, Li J, Wu F. A novel method for the preparation of zeolite ZSM-5. J Chem Soc Chem Commun 1990:755–6.
[68] Arnold A, Hunger M, Weitkamp J. Dry-gel-Synthese von Zeolithen des Typs [Ga]Beta und deren quantitative Charakterisierung mittels NMR-Spektroskopie. Chem Eng Technol 2001;73:1588–92.
[69] Arnold A, Steuernagel S, Hunger M, Weitkamp J. Insight into the dry-gel synthesis of gallium-rich zeolite [Ga]Beta. Microporous Mesoporous Mater 2003;62:97–106.
[70] Pines A, Gibby MG, Waugh JS. Proton-enhanced NMR of dilute spins in solids. J Chem Phys 1973;59:569–90.
[71] Burkett SL, Davis ME. Mechanism of structure direction in the synthesis of Si-ZSM-5: an investigation by intermolecular ^{1}H–^{29}Si CP MAS NMR. J Phys Chem B 1994;98:4647–53.
[72] Burkett SL, Davis ME. Mechanisms of structure direction in the synthesis of pure-silica zeolites. 1. Synthesis of TPNSJ-ZSM-5. Chem Mater 1995;7:920–8.
[73] Gougeon R, Delmotte L, Le Nouen D, Gabelica Z. The early stages in the behaviour of tetrapropylammonium cations in the synthesis of gel precursor to pure siliceous MFI zeolite: an in situ multinuclear NMR study. Microporous Mesoporous Mater 1998;26:143–51.
[74] Koller H. New developments of NMR spectroscopy applied to zeolite catalysts. Stud Surf Sci Catal 2004;149:105–22.
[75] Gullion T, Schaefer J. Rotational-echo double-resonance NMR. J Magn Reson 1989;81:196–200.
[76] Eckert H, Elbers S, Epping JD, Jansen M, Kalwei M, Strojek W, et al. Dipolar solid state NMR approaches towards medium-range structure in oxide glasses. Top Curr Chem 2004;246:195–233.
[77] Shantz DF, Fild C, Koller H, Lobo RF. Guest–host interactions in As-made Al-ZMS-12: implications for the synthesis of zeolite catalysts. J Phys Chem B 1999;103:10858–65.
[78] Lee GS, Nakagawa Y, Hwang S-J, Davis ME, Wagner P, Beck L, Zones SI. Organocations in zeolite synthesis: fused bicyclo [l.m.0] cations and the discovery of SSZ-48. J Am Chem Soc 2002;124:7024–34.
[79] Zones SI, Hwang S-J, Elomari S, Ogino I, Davis ME, Burton AW. The fluoride-based route to all-silica molecular sieves: a strategy for synthesis of new materials based upon close-packing guest–host products. CR Chim 2005;8:267–82.
[80] Han B, Lee S-H, Shin C-H, Cox PA, Hong SB. Zeolite synthesis using flexible diquaternary alkylammonium ions $(C_nH_{2n+1})_2HN^+(CH_2)_5N^+H(C_nH2_{n+1})_2$ with $n=1$–5 as structure-directing agents. Chem Mater 2005;17:477–86.
[81] Lee H, Zones SI, Davis ME. Zeolite synthesis using degradable structure-directing agents and pore-filling agents. J Phys Chem B 2005;109:2187–91.
[82] Millini R, Perego G, Bellussi G. Synthesis and characterization of boron-containing molecular sieves. Top Catal 1999;9:13–34.
[83] Zones SI, Hwang S-J. The inorganic chemistry of guest-mediated zeolite crystallization: a comparison of the use of boron and aluminum as lattice-substituting components in the presence of a single guest molecule during zeolite synthesis. Microporous Mesoporous Mater 2003;58:263–77.
[84] Valyocsik EW. Synthesis of porous crystalline MCM-58, US Patent 5,441,721;1995.
[85] Dong W-Y, Sun Y-J, He H-Y, Long Y-C. Synthesis and structural characterization of B-Al-ZSM-5 zeolite from boron–silicon porous glass in the vapor phase. Microporous Mesoporous Mater 1999;32:93–100.
[86] Liu H, Ernst H, Freude D, Scheffler F, Schwieger W. In situ ^{11}B MAS NMR study of the synthesis of a boron-containing MFI type zeolite. Microporous Mesoporous Mater 2002;54:319–30.
[87] Rauscher M, Selvam T, Schwieger W, Freude D. Hydrothermal transformation of porous glass granules into ZSM-5 granules. Microporous Mesoporous Mater 2004;75:195–202.
[88] Schoeman BJ, Regev O. A study of the initial stage in the crystallization of TPA-silicalite-1. Zeolites 1996;17:447–56.
[89] Persson AE, Schoeman BJ, Sterte J, Otterstedt J-E. The synthesis of discrete colloidal particles of TPA-silicalite-1. Zeolites 1994;14:557–67.
[90] Kirschhock CEA, Buschmann V, Kremer S, Ravishankar R, Houssin CJY, Mojet BL, et al. Zeosil Nanoslabs: building blocks in nPr_4N^+-mediated synthesis of MFI zeolite. Angew Chem Int Ed 2001;40:2637–40.
[91] Kirschhock CEA, Liang D, Aerts A, Aerts CA, Kremer SPB, et al. On the TEM and AFM evidence of zeosil nanoslabs present during the synthesis of silicalite-1—reply. Angew Chem Int Ed 2004;43:4562–4.
[92] Ravishankar R, Kirschhock CEA, Knops-Gerrits P-P, Feijen EJP, Grobet PJ, Vanoppen P, et al. Characterization of nanosized material extracted from clear suspensions for MFI zeolite synthesis. J Phys Chem B 1999;103:4960–4.
[93] Kirschhock CEA, Ravishankar R, Van Looveren L, Jacobs PA, Martens JA. Mechanism of transformation of precursors into nanoslabs in the early stages of MFI and MEL zeolite formation from TPAOH–TEOS–H_2O and TBAOH–TEOS–H_2O mixtures. J Phys Chem B 1999;103:4972–8.
[94] Kirschhock CEA, Kremer SPB, Vermant J, Van Tendeloo G, Jacobs PA, Martens JA. Design and synthesis of hierarchical materials from ordered zeolitic building units. Chem Eur J 2005;11:4306–13.
[95] Ramanan H, Kokkoli E, Tsapatsis M. On the TEM and AFM evidence of zeosil nanoslabs present during the synthesis of silicalite-1. Angew Chem Int Ed 2004;43:4558–61.
[96] Kragten D, Fedeyko JM, Sawant KR, Rimer JD, Vlachos DG, Lobo RF, et al. Structure of the silica phase extracted from silica/(TPA)OH solutions containing nanoparticles. J Phys Chem B 2003;107: 10006–16.
[97] Koller H, Lobo RF, Burkett SL, Davis ME. $SiO^{-}\cdots HOSi$ hydrogen bonds in as-synthesized high-silica zeolites. J Phys Chem 1995;99:12588–96.
[98] Fedeyko JM, Sawant KR, Kragten D, Vlachos DG, Lobo RF. The structure of subcolloidal zeolite precursor nanoparticles. Stud Surf Sci Catal 2004;154:1267–73.
[99] Fedeyko JM, Vlachos DG, Lobo RF. Formation and structure of self-assembled silica nanoparticles in basic solutions of organic and inorganic cations. Langmuir 2005;21:5197–206.
[100] Fedeyko JM, Rimer JD, Lobo RF, Vlachos DG. Spontaneous formation of silica nanoparticles in basic solutions of small tetraalkylammonium cations. J Phys Chem B 2004;108:12271–5.
[101] Rimer JD, Vlachos DG, Lobo RF. Evolution of self-assembled silica-tetrapropylammonium nanoparticles at elevated temperatures. J Phys Chem B 2005;109:12762–71.
[102] Nikolakis V, Kokkoli E, Tirrell M, Tsapatsis M, Vlachos DG. Zeolite growth by addition of subcolloidal particles: modeling and experimental validation. Chem Mater 2000;12:845–53.
[103] Brouwer DH, Darton RJ, Morris RE, Levitt MH. A solid-state NMR method for solution of zeolite crystal structures. J Am Chem Soc 2005;127:10365–70.
[104] Hedin N, Graf R, Christiansen SC, Gervais C, Hayward RC, Eckert J, et al. Structure of a surfactant-templated silicate framework in the absence of 3D crystallinity. J Am Chem Soc 2004;126:9425–32.

[105] Kristiansen PE, Carravetta M, Lai WC, Levitt MH. A robust pulse sequence for the determination of small homonuclear dipolar couplings in magic-angle spinning NMR. Chem Phys Lett 2004;390:1–7.
[106] Brouwer DH, Kristiansen PE, Fyfe CA, Levitt MH. Symmetry-based ^{29}Si dipolar recoupling magic angle spinning NMR spectroscopy: a new method for investigating three-dimensional structures of zeolite frameworks. J Am Chem Soc 2005;127:542–3.
[107] Wilson ST, Lok BM, Messina CA, Cannan TR, Flanigen EM. Aluminophosphate molecular sieves: a new class of microporous crystalline inorganic solids. J Am Chem Soc 1982;104:1146–7.
[108] Pastore HO, Coluccia S, Marchese L. Porous aluminophosphates: from molecular sieves to designed acid catalysts. Annu Rev Mater Res 2005; 35:351–95.
[109] Barrie PJ. In: Clark RJH, Hester RE, editors. Spectroscopy of new materials. Chichester: John Wiley and Sons; 1993. p. 151.
[110] Taulelle F. Crystallogenesis of microporous metallophosphates. Curr Opin Solid State Mater Sci 2001;5:397–405.
[111] Taulelle F, Haouas M, Gerardin C, Estournes C, Loiseau T, Ferey G. NMR of microporous compounds. From in situ reactions to solid paving. Colloids Surf A 1999;158:299–311.
[112] Gerardin C, Haouas M, Lorentz C, Taulelle F. NMR quantification in hydrothermal in situ syntheses. Magn Reson Chem 2000;38:429–35.
[113] Gerardin C, In M, Allouche L, Haouas M, Taulelle F. In situ pH probing of hydrothermal solutions by NMR. Chem Mater 1999;11:1285–92.
[114] Vistad ØB, Akporiaye DE, Taulelle F, Lillerud KP. In situ NMR of SAPO-34 crystallization. Chem Mater 2003;15:1639–49.
[115] Vistad ØB, Akporiaye DE, Taulelle F, Lillerud KP. Morpholine, an in situ ^{13}C NMR pH meter for hydrothermal crystallogenesis of SAPO-34. Chem Mater 2003;15:1650–4.
[116] Vistad ØB, Akporiaye DE, Lillerud KP. Identification of a key precursor phase for synthesis of SAPO-34 and kinetics of formation investigated by in situ X-ray diffraction. J Phys Chem B 2001; 105:12437–47.
[117] Huang Y, Machado D, Kirby CW. A Study of the Formation of Molecular Sieve SAPO-44. J Phys Chem B 2004;108:1855–65.
[118] Huang Y, Richer R, Kirby CW. Characterization of the Gel Phases of $AlPO_4$-11 Molecular Sieve Synthesis by Solid-state NMR. J Phys Chem B 2003;107:1326–37.
[119] Huang Y, Machado D. Mapping out the connectivities in intermediate gel phases of molecular sieve synthesis by solid-state NMR. Microporous Mesoporous Mater 2001;47:195–202.
[120] Vega AJ. Heteronuclear chemical-shift correlations of silanol groups studied by two-dimensional cross-polarization/ magic angle spinning NMR. J Am Chem Soc 1988;110:1049–54.
[121] Grey CP, Veeman WS, Vega AJ. Rotational echo ^{14}N/^{13}C/^{1}H triple resonance solid-state nuclear magnetic resonance: A probe of ^{13}C–^{14}N internuclear distances. J Chem Phys 1993;98:7711–24.
[122] Huang Y, Demko BA, Kirby CW. Investigation of the evolution of intermediate phases of $AlPO_4$-18 molecular sieve synthesis. Chem Mater 2003;15:2437–44.
[123] Wang K, Yu J, Li C, Xu R. Studies on an intermediate phase $Al_5P_5O_{20}(OH)^*_2C_6H_{18}N^*_2 3H_2O$ and its transformation to AlPO-HDA. Stud Surf Sci Catal 2004;154:1007–13.
[124] Liu Z, Xu W, Yang G, Xu R. New insights into the crystallization mechanism of mesoporous $AlPO_4$-21. Microporous Mesoporous Mater 1998;22:33–41.
[125] Firouzi A, Stucky GD, Chmelka BF. Self-assembly of silicate–surfactant liquid crystals during mesophase materials syntheses. In: Ocelli ML, Kessler H, editors. Synthesis of porous materials. New York: Marcel Dekker; 1996. p. 379–89.
[126] Firouzi A, Atef F, Oertli AG, Stucky GD, Chmelka BF. Alkaline lyotropic silicate–surfactant liquid crystals. J Am Chem Soc 1997;119: 3596–610.
[127] Kresge CT, Leonowicz ME, Roth WJ, Vartuli JC, Beck JS. Ordered mesoporous molecular sieves synthesized by a liquid-crystal template mechanism. Nature 1992;359:710–2.
[128] Firouzi A, Kumar D, Bull LM, Besier T, Sieger P, Huo Q, et al. Cooperative organization of inorganic–surfactant and biomimetic assemblies. Science 1995;267:1138–43.
[129] Seelig J. Deuterium magnetic–resonance—theory and application to lipid-membranes. Q Rev Biophys 1977;10:353–418.
[130] Steel A, Carr SW, Anderson MW. ^{14}N NMR study of surfactant mesophases in the synthesis of mesoporous silicates. J Chem Soc Chem Commun 1994;13:1571–2.
[131] Israelachvili JN. Intermolecular and surface forces. London: Academic Press; 1991.
[132] Tolbert SH, Landry CC, Stucky GD, Chmelka BF, Norby P, Hanson JC, et al. Phase transitions in mesostructured silica/surfactant composites: surfactant packing and the role of charge density matching. Chem Mater 2001;13:2247–56.
[133] Huo Q, Margolese DI, Ciesla U, Demuth DG, Feng P, Gier TE, et al. Organization of organic molecules with inorganic molecular species into nanocomposite biphase arrays. Chem Mater 1994;6:1176–91.
[134] Galarneau A, Di Renzo F, Fajula F, Mollo L, Fubini B, Ottaviani MF. Kinetics of formation of micelle-templated silica mesophases monitored by electron paramagnetic resonance. J Colloid Interface Sci 1998; 201:105–17.
[135] Egger CC, Anderson MW, Tiddy GJT, Cascic JL. In situ NMR and XRD studies of the growth mechanism of SBA-1. Phys Chem Chem Phys 2005;7:1845–55.
[136] Schmidt-Rohr K, Clauss J, Spiess HW. Correlation of structure, mobility, and morphological information in heterogeneous polymer materials by two-dimensional wideline-separation NMR spectroscopy. Macromolecules 1992;25:3273–7.
[137] Janicke MT, Landry CC, Christiansen SC, Kumar D, Stucky GD, Chmelka BF. Aluminum incorporation and interfacial structures in MCM-41 mesoporous molecular sieves. J Am Chem Soc 1998;120:6940–51.
[138] Janicke MT, Landry CC, Christiansen SC, Birtalan S, Stucky GD, Chmelka BF. Low silica MCM-41 composites and mesoporous solids. Chem Mater 1999;11:1342–51.
[139] Melosh NA, Lipic P, Bates FS, Wudl F, Stucky GD, Fredrickson GH, et al. Molecular and mesoscopic structures of transparent block copolymer-silica monoliths. Macromolecules 1999;32:4332–42.
[140] Melosh NA, Davidson P, Chmelka BF. Monolithic mesophase silica with large ordering domains. J Am Chem Soc 2000;123:823–9.
[141] Ruthstein S, Frydman V, Kababya S, Landau M, Goldfarb D. Study of the formation of the mesoporous material SBA-15 by EPR spectroscopy. J Phys Chem B 2003;107:1739–48.
[142] Ruthstein S, Frydman V, Goldfarb D. Study of the initial formation stages of the mesoporous material SBA-15 using spin-labeled block co-polymer templates. J Phys Chem B 2004;108:9016–22.
[143] Flodström K, Wennerström H, Alfredsson V. Mechanism of mesoporous silica formation. A time-resolved NMR and TEM study of silica-block copolymer aggregation. Langmuir 2004;20:680–8.
[144] Flodström K, Teixeira CV, Amenitsch H, Alfredsson V, Lindén M. In situ synchrotron small-angle X-ray scattering/X-ray diffraction study of the formation of SBA-15 mesoporous silica. Langmuir 2004;20:4885–91.
[145] Flodström K, Wennerström H, Teixeira CV, Amenitsch H, Lindén M, Alfredsson V. Time-resolved in situ studies of the formation of cubic mesoporous silica formed with triblock copolymers. Langmuir 2004;20:10311–6.
[146] Ryoo R, Ko CH, Kruk M, Antochshuk V, Jaroniec M. Block-copolymer-templated ordered mesoporous silica: array of uniform mesopores or mesopore-micropore network? J Phys Chem B 2000; 104:11465–71.
[147] Kruk M, Jaroniec M, Ko CH, Ryoo R. Characterization of the porous structure of SBA-15. Chem Mater 2000;12:1961–8.
[148] Galarneau A, Cambon H, Di Renzo F, Fajula F. True microporosity and surface area of mesoporous SBA-15 silicas as a function of synthesis temperature. Langmuir 2001;17:8328–35.
[149] De Paul SM, Zwanziger JW, Ulrich R, Wiesner U, Spiess HW. Structure, mobility, and interface characterization of self-organized organic–inorganic hybrid materials by solid–state NMR. J Am Chem Soc 1999; 121:5727–36.

[150] Ulrich R, Zwanziger JW, De Paul SM, Reiche A, Leuninger H, Spiess HW, et al. Solid hybrid polymer electrolyte networks: nano-structurable materials for lithium batteries. Adv Mater 2002;14:1134–7.
[151] Schubert U, Hüsing N, Lorenz A. Hybrid inorganic–organic materials by sol–gel processing of organofunctional metal alkoxides. Chem Mater 1995;7:2010–27.
[152] Antonietti M, Göltner C. Superstructures of functional colloids: chemistry on the nanometer scale. Angew Chem Int Ed 1997; 36:910–28.
[153] Templin M, Franck A, Du Chesne A, Leist H, Zhang Y, Ulrich R, et al. Organically modified aluminosilicate mesostructures from block copolymer phases. Science 1997;278:1795–8.
[154] Christiansen SC, Zhao D, Janicke MT, Landry CC, Stucky GD, Chmelka BF. Molecularly ordered inorganic frameworks in layered silicate surfactant mesophases. J Am Chem Soc 2001;123:4519–29.
[155] Wang L-Q, Exarhos GJ. Study of local molecular ordering in layered surfactant–silicate mesophase composites. J Phys Chem B 2003;107: 443–50.
[156] Xia Y, Mokaya R, Titman JJ. Formation of molecularly ordered layered mesoporous silica via phase transformation of silicate–surfactant composites. J Phys Chem B 2004;108:11361–7.
[157] Schüth F. Non-siliceous mesostructured and mesoporous materials. Chem Mater 2001;13:3184–95.
[158] Davis RJ, Liu Z. Titania–silica: a model binary oxide catalyst system. Chem Mater 1997;9:2311–24.
[159] Zhang X, Zhang F, Chan K-Y. Synthesis of titania–silica mixed oxide mesoporous materials, characterization and photocatalytic properties. Appl Catal A 2005;284:193–8.
[160] Gervais C, Babonneau F, Smith ME. Detection, quantification, and magnetic field dependence of solid-state ^{17}O NMR of X–O–Y (X,Y = Si, Ti) linkages: implications for characterizing amorphous titania–silica-based materials. J Phys Chem B 2001;105:1971–7.
[161] Delattre L, Babonneau F. ^{17}O solution NMR characterization of the preparation of sol–gel derived SiO_2/TiO_2 and SiO_2/ZrO_2 glasses. Chem Mater 1997;9:2385–94.
[162] Day VW, Eberspacher TA, Klemperer WG, Park CW, Rosenberg FS. Solution structure elucidation of early-transition-metal polyoxoalkoxides using ^{17}O nuclear magnetic resonance spectroscopy. J Am Chem Soc 1991;113:8190–2.
[163] Soler-Illia GJ de AA, Sanchez C. Interactions between poly(ethylene oxide)-based surfactants and transition metal alkoxides: their role in the templated construction of mesostructured hybrid organic–inorganic composites. New J Chem 2000;24:493–9.
[164] Gerfin T, Grätzel M, Walder L. Molecular and supramolecular surface modification of nanocrystalline TiO_2 films: charge-separating and charge-injecting devices. Prog Inorg Chem 1997;44:345–93.
[165] Yang P, Zhao D, Margolese DI, Chmelka BF, Stucky GD. Generalized syntheses of large-pore mesoporous metal oxides with semicrystalline frameworks. Nature 1998;396:152–5.
[166] Brinker CJ, Lu Y, Sellinger A, Fan H. Evaporation-induced self-assembly: nanostructures made easy. Adv Mater 1999;11:579–85.
[167] Soler-Illia GJ de AA, Scolan E, Louis A, Albouy P-A, Sanchez C. Design of meso-structured titanium oxo based hybrid organic–inorganic networks. New J Chem 2001;25:156–65.
[168] Grosso D, Soler-Illia GJ de AA, Babonneau F, Sanchez C, Albouy P-A, Brunet-Bruneau A, et al. Highly organized mesoporous titania thin films showing mono-oriented 2D hexagonal channels. Adv Mater 2001; 13:1085–90.
[169] Alberius PCA, Frindell KL, Hayward RC, Kramer EJ, Stucky GD, Chmelka BF. General predictive syntheses of cubic, hexagonal, and lamellar silica and titania mesostructured thin films. Chem Mater 2002;14:3284–94.
[170] Crepaldi EL, Soler-Illia GJ de AA, Grosso D, Cagnol F, Ribot F, Sanchez C. Controlled formation of highly organized mesoporous titania thin films: from mesostructured hybrids to mesoporous nanoanatase TiO_2. J Am Chem Soc 2003;125:9770–86.